Analysis of Fluid and Particle Dynamics in a Spiral Jet Mill by Coupled CFD-DEM

by

Lewis Michael Scott

Submitted in accordance with the requirements for the degree of
Doctor of Philosophy

The University of Leeds
School of Chemical and Process Engineering

March, 2022

The candidate confirms that the work submitted is his/her own, except where work which has formed part of jointly-authored publications has been included. The contribution of the candidate and the other authors to this work has been explicitly indicated below. The candidate confirms that appropriate credit has been given within the thesis where reference has been made to the work of others.

Chapter 5 of the thesis has been prepared as a paper and accepted into the journal of Powder Technology. The other authors are part of the supervisory team.

Chapter 6 of the thesis has been prepared as a paper and accepted into the journal of Powder Technology. The other authors are part of the supervisory team.

Chapter 7 of the thesis has been prepared as a paper and accepted into the journal of Powder Technology. Dr. Alberto Di Renzo was initially consulted on this section of the thesis. The other authors are part of the supervisory team.

Acknowledgements

Firstly, I would like to express my sincerest gratitude to my supervisor, Professor Mojtaba Ghadiri, for giving the opportunity to become a member of group as a PhD student. Your dedication to project, honesty and support has been unwavering from beginning to end. My deepest thanks to my co-supervisor, Dr. Antonia Borissova for always making time to discuss the project and the hours spent picking through my work.

I am grateful to Astra Zeneca for sponsoring the project and support provided by the Ian Gabbott and Catherine Hallam, as well as the guidance offered by Hosokawa Micron.

To Dr David Austin, Dr Dewi Ballard, Dr Peter Kaskiewicz and Dr Jonathan White, I would like to congratulate you all! You're friendship throughout the PhD meant everything and I couldn't of met a better group of guys.

Dr Wei Pin Goh!! Thank you for all your help, allowing me to vent and keeping me focused! You are an amazing person and I wish you very best for the future. Dr. Selasi Dogbe, thank you for all your help getting the project off the ground and, Dr. Mehrdad Pasha, for all the training provided.

I will always be grateful to my parents, Mr. Norman Scott and Mrs. Alison Ward for your constant support throughout this journey. After starting university all those years ago, and never being more than a phone call away.

Abstract

The spiral jet mill is fundamentally very simple in its design and operation. However, it is difficult to predict the particle product size without empirical knowledge of the system being used. There is a dynamic relationship between solid material and gas inputs, as well as an interdependence between breakage and classification all occurring in the same chamber. The role of particle hold-up and how it affects both particle dynamics and fluid behaviour has been investigated. By changing the mass loading and keeping the grinding gas pressure constant it is shown that the particle bed indirectly decreases the fluid gas velocity surrounding the classifier, as the particles in the bed dampen the fluid field and lower its kinetic energy. It is also shown that the kinetic energy of the particle system remains largely unaffected by mass loading, whilst the vortex is stable. This is because the energy provided to the bed by the gas jets remains unchanged.

The grinding gas pressure is varied at different mass loading to investigate the jet behaviour. The results show that particle behaviour changes as the number of particles increases, or pressure decreases, as the grinding gas jets can no longer penetrate through the densely packed bed. This inhibits particles from reaching the highest velocities needed to cause fragmentation and chipping.

To approach scaling, the coarse grain method is applied. This method replaces groups of smaller particles, with a single larger one. Both the kinetic energy and dissipated energy are modelled successfully for the lowest scaling values of 4 or fewer particles per group. The predicted behaviour of the particles in the bed agrees with the base case. However, particle velocity in the lean region disagrees with the original simulation due to the reduced number of particles present. Finally, the Ghadiri & Zhang breakage model has been implemented to allow for size reduction by chipping. By recording the mass loss with respect to time at various gas pressures, the total work leading to breakage can be calculated and optimised. The work developed here provides a capability of predictive milling for various applications based on the mechanical and physical properties of single particles.

Table of Contents

List of Tables

List of Figures

Chapter 1 Thesis outline and structure

This chapter of the thesis will outline each chapter in brief, providing a short overview on what is included in each chapter.

Chapter 2 provides the necessary background to the major components of the thesis. An introduction to the use and operation of a spiral jet mill is first discussed, before introducing the simulation techniques that heavily feature in the work; computational fluid dynamics (CFD) and discrete element method (DEM) modelling.

Chapter 3 discusses the literature detailing the spiral jet mill. First considering its operation and which parameters have the largest effect on controlling product size. Second, the design features of the mill, and finally, other works which consider the cut size in more detail.

Preliminary work that was necessary to the complete before any simulations to obtain data is discussed in Chapter 4. The in-house 3-D model used in this body of work is based on the AS-50 spiral jet mill manufactured by Hosokawa Micron (Runcorn, UK). It took several iterations to accurately model the mill, as no drawing was available. Included in this chapter is the mesh independence study to predict the gas field, as well as the final drawing of the mill with dimensions

The role of hold-up in the mill by analysing the effect of different mass loading on the fluid field and particle dynamics is discussed in Chapter 5.

The role of the grinding pressure on the particle bed and fluid field is discussed in Chapter 6. A range of pressures are analysed at different mass loadings.

Chapter 7 focuses on scaling the particles whilst maintaining the bulk behaviour of the solid material and without changing the fluid flow field. The technique investigated is coarse graining, as it allows for larger simulations by replacing groups of small particles with a single larger one.

Chapter 8 of work investigates particle breakage in the mill. The Ghadiri and Zhang chipping model was selected as the breakage model and the grinding gas pressure and mass loading are varied in the study. The mass loss, change in particle radius, work efficiency and position of breakage are all analysed.

Chapter 2 Background

This section will introduce the reader to the background concepts of the thesis; i.e. the spiral jet mill, CFD, DEM and coupling.

2.1. Particle Size Reduction

Particle size reduction (PSR) is the act of reducing a medium down to a useful size; this could be for either end-use, or for further processing. The process of PSR is known as comminution and it is required across many sectors and industries; including construction, mining, power generation, pharmaceuticals and paints [1].

There are many types of PSR equipment that exist. They vary by PSR method, feed rate, feed size and desired product size. Table 2-1 provides some examples of different PSR equipment that are used. Compression is used at larger feed sizes as the material breaks more easily in general. However, as the medium becomes smaller and particle size decreases, impaction and attrition are required to achieve the smallest product sizes.

Table 2-1: Examples of PSR equipment and product size [1–3]

Method	**Example equipment**	**Approx. diameter of the product (*μm*)**
Coarse crushing	Jaw crusher Gyratory crusher	5000-50,000
Cutting	Cutter mill Shears	100-80,000
Compression	Rod mill Pestle and mortar	50-10,000
Impaction	Hammer mill Disintegrator	50-8000
Attrition	Cordial mill Roller mill	0.01-50
Combined Attrition and Impact	Fluid Energy mill Ball mill	1-2000

2.2. Spiral Jet Mill

The spiral jet mill is a type of fluid energy mill, which employs a combination of particle impaction and abrasion to reduce the feed material to the desired size. The mill is simple in its design and in operation. A series of high-pressure gas nozzles are set at angles inside a circular chamber and form an internal vortex of gas. Air is typically used as the gas of choice during operation;

however, there are instances where an inert gas may be chosen to safeguard against material degradation, such as nitrogen. Typically, the spiral jet mill is capable of producing a product size below 10 μm. Yet, the mill is typically chosen due to the narrow size distribution of the product.

By only using gas to accelerate the particles in the mill, size-reduction is autogenic; the particles reduce in size due to inter-particle collisions and collisions with the chamber wall. This method of breakage is advantageous as it does not rely on an additional solid medium, or mechanical action to aid size reduction. Furthermore, the lack of moving parts reduces the cost of maintaining the mill and minimises possible causes of product contamination. It is also possible to accurately regulate the temperature in the mill, given the large throughput of gas [4]. However, particle size reduction comes at a high cost when using a spiral jet mill, as only 2% of the energy supplied to mill is used in breakage [5]. This low energy ultilisation found in the spiral jet mill is due to creation and stabilisation of the vortex, as well as the suspension of particles.

2.3. Spiral Jet Mill Operation

Figure 2-1 depicts the mill used throughout this work, which is based on the Hosokawa AS-50 spiral jet mill (Runcorn, UK). Its operation and design shares many commonalties with other spiral jet mills. The feed material is introduced into the mill using a hopper (A) and accelerated into the main chamber by a high-pressure jet of gas delivered through the feed nozzle (B). In the AS-50 spiral jet mill, the feed enters the mill through a port (C) in the ceiling at around 12 mm from the centre.

The grinding gas is delivered into an annular manifold (D), which feeds the four grinding nozzles (E). After entering the main chamber of the mill, the particles are accelerated in a circular motion. The centrifugal field generated by the high-pressure air causes the particles to form a dense bed along the outer wall of the chamber. Due to velocity gradient of the gas field, the bed forms layers of the particles that shear across one another resulting in size reduction. At the same time, particles in the jet streams are subjected to high-velocity collisions upon re-entering the bed. An induced free-vortex is formed around the classifier-ring (F) due to the constriction between the ring and chamber ceiling. Particles that are too large back into the chamber travel back towards the bed due to their own inertia. Only particles that are small enough travel out the mill due to the drag force of the gas. The AS-50 has a unique design, as the constriction is vertical and forces the gas upwards into a

hemispherical chamber. A vortex-finder (G) is then employed to force the gas downwards leading to the exit of the mill (H).

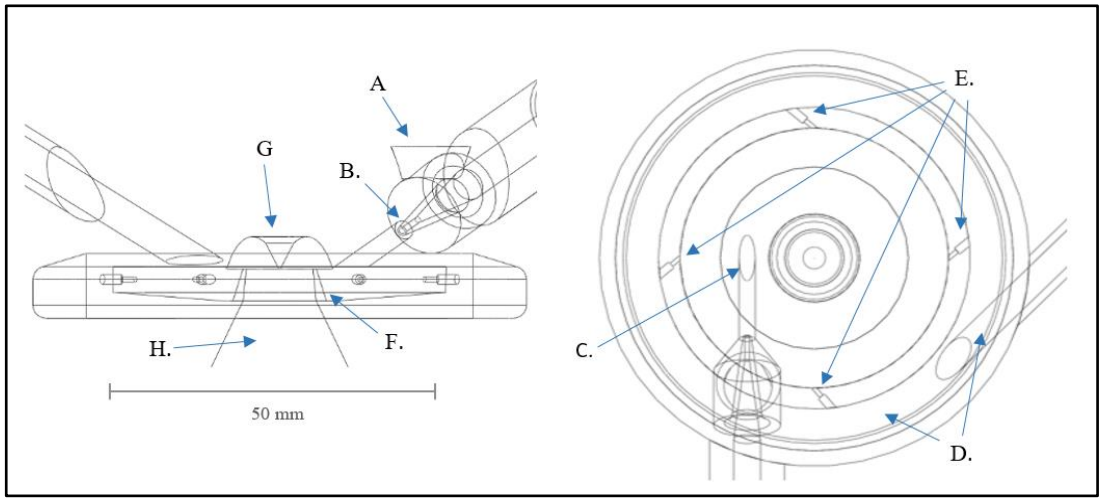

Figure 2-1: In-house CAD drawing of the Hosokawa AS-50 spiral Jet Mill (Runcorn, UK) with annotations; (A) hopper, (B) feed air nozzle, (C) feed entry point, (D) grinding air delivery pipe and annulus section, (E) grinding nozzles, (F) classifier ring, (G) vortex finder, (H) exit pipe form mill. Side view with the diameter of the main chamber (left) and top-down view (right).

2.4. Computational Fluid Dynamics

Computational fluid dynamics (CFD) is the numerical approach of predicting the motion of turbulent fluids using a set a partial differential equations, known as the Reynolds-Averaged-Navier-Stokes (RANS) equations. The geometry or volume that the fluid will travel through is divided down into a number of cells, when combined, is referred to as the mesh. A set of input parameters, referred to as boundary conditions are provided to model and with the RANS equations, each element of the mesh is solved in turn to determine the pressure gradient, and therefore, the direction and rate of flow. Typically, a known pressure or velocity is used as an input. The system may be under vacuum or the pressure may be atmospheric at the outlet, hence the system is solved in reverse from the exit.

One problem with the RANS equations is that it cannot be solved out right, due to the non-linearity of the Navier-Stokes equations. Attempting to resolve this equation creates a new term referred to as the Reynolds stress term:

$$R_{ij} = -\rho\overline{\boldsymbol{v}'_{\boldsymbol{\iota}}\boldsymbol{v}'_{\boldsymbol{J}}} \quad [1]$$

where R_{ij} is the Reynolds stress term, ρ is the fluid density, and $\boldsymbol{v'_i}$ & $\boldsymbol{v'_j}$ are the instantaneous velocities in their respected directions.

Therefore, to close the RANS equations a turbulence model is needed. There are three common choices when selecting a turbulence model for simulation; these are the *k-ε*, *k-ω* and RSM. Both the *k-ε* and *k-ω* are two-equation models, based on the original Boussinesq's (1877) eddy-viscosity model. Therefore, in both these models turbulence is assumed to be isotropic. The *k-ε* model by Launder and Spalding [6] describe the evolution of turbulent eddies by their kinetic energy and the amount of energy they dissipate; *k* and *ε*, respectively. The two terms are described by the following equations:

$$\frac{\partial(\rho k)}{\partial t}+\frac{\partial(pk\boldsymbol{u}_i)}{\partial x_i}=\frac{\partial}{\partial x_j}\left[\frac{\mu_t}{\sigma_k}\frac{\partial k}{\partial x_j}\right]+2\mu_t E_{ij}E_{ij}-\rho\varepsilon \quad [2]$$

$$\frac{\partial(\rho\varepsilon)}{\partial t}+\frac{\partial(p\varepsilon\boldsymbol{u}_i)}{\partial x_i}=\frac{\partial}{\partial x_j}\left[\frac{\mu_t}{\sigma_\varepsilon}\frac{\partial \varepsilon}{\partial x_j}\right]+C_1\frac{\varepsilon}{k}2\mu_t E_{ij}E_{ij}-C_2\rho\frac{\varepsilon^2}{k} \quad [3]$$

where $\boldsymbol{u}_i$ is the velocity component in a given direction, E_{ij} is the rate of deformation, μ_t is the eddy viscosity given by:

$$\mu_t=\rho C_\mu\frac{k^2}{\varepsilon} \quad [4]$$

The constants in these equations (C_μ, C_1, C_2, σ_ε and σ_k) are what allow for the RANS equations to be solved. These constants are adjustable; however, they have been fitted over multiple studies to suit a wide range of turbulent flows. The *k-ω* model differs to the *k-ε* model, as it describes the kinetic energy and specific rate of turbulent energy decay into thermal energy, *k* and *ω* respectively. Proposed by Wilcox [7] and later modified by the same author in 2008 [8], the two terms can be expressed by the equations:

$$\frac{\partial(\rho k)}{\partial t}+\frac{\partial(\rho\boldsymbol{u}_j k)}{\partial x_j}=\rho P-\beta^*\rho\omega k+\frac{\partial}{\partial x_j}\left[\left(\mu+\sigma_k\frac{pk}{\omega}\right)\frac{\partial k}{\partial x_j}\right] \quad [5]$$

$$\frac{\partial(\rho\omega)}{\partial t}+\frac{\partial(\rho\boldsymbol{u}_j\omega)}{\partial x_j}=\frac{\alpha\omega}{k}P-\beta\rho\omega^2+\frac{\partial}{\partial x_j}\left[\left(\mu+\sigma_\omega\frac{pk}{\omega}\right)\frac{\partial\omega}{\partial x_j}\right]+\frac{\rho\sigma_d}{\omega}\frac{\partial k}{\partial x_j}\frac{\partial\omega}{\partial x_j} \quad [6]$$

$$P=\tau_{ij}\frac{\partial u_i}{\partial x_j} \quad [7]$$

where P is the mean static pressure, τ_{ij} is the Favre-averaged specific Reynolds-stress tensor, α, β, σ_d are all closure coefficients for the specific dissipation rate closure equation, β and σ_k are the closure coefficients for the turbulent kinetic energy equation. As with the *k-ε* model, the *k-ω* has been

investigated many times since its inception and therefore common values for the coefficients exist. Both models remain popular due to their low computational cost; however, each model has its disadvantages from their isotropic assumption of turbulent eddies. In reality turbulent eddies behave in an anisotropic manner. Hence, for some complicated fluid fields, two-equation models are no longer suitable and more equations are needed to describe a turbulent system. One of the most common and popular models is the Reynold's Stress Model (RSM). The RSM model is a second order closure model and is constructed from 6 partial equations, more easily written as:

$$\frac{dR_{ij}}{dt} = D_{ij} + \mathrm{P}_{ij} + \Pi_{ij} + \Omega_{ij} - \varepsilon_{ij} \quad [8]$$

where R_{ij} is the Reynolds stress transport kinematic, D_{ij} is the diffusion term, P_{ij} is the production term, Π_{ij} is the pressure term, Ω_{ij} is the rotation term and ε_{ij} is the dissipation term. Out of all the terms, only the production term can be solved directly, the other five terms require closure modelling.

2.5. Discrete Element Method Modelling

There are two different approaches for describing the motion of solids; either as a continuum or by tracking each individual particle in a system [9]. In continuum modelling, the solids are treated similarly to CFD modelling. A volume of material is modelled over a grid and subjected to stress. The stress can be applied anisotropically, allowing particle behaviour on the microscale to affect the macroscopic flow of the material [10]. The benefit to treating the solid material in such a way is that it allows for less expensive computation requirements. Yet, the main disadvantage of this technique is that the solid material is modelled by averaging its bulk behaviour and motion. . For Discrete Element Method (DEM) modelling this is not the case, as it is possible to track the trajectory of each single particle in the assembly. However, this type of modelling comes at great computational expense, and therefore, limits the total volume that can be tracked. The particles motion is described using Newton's second law of motion, whilst their location is tracked using a grid.

In DEM modelling, the particles are treated as distinct bodies that are able to come into contact. Depending on the system being studied, the contact mechanics can be changed so that the particles behave differently during collision events. The particles can be treated either as a soft-sphere; allowing deformation to be inferred, or as a rigid, hard-sphere [11]. Of the two models, the hard-sphere model is less complex, as deformation of the particle is

ignored. This makes it ideal for larger simulations where particle interactions are less significant, such as within bulk solids handling and the transport on conveyor belts [12].

If particle interactions cannot be neglected, then a soft-sphere model can be used. Instead of modelling surface deformation, the particles in contact are allowed to overlap and the region in contact is treated as a spring under compression. The relative velocity and total size of the overlap is used to calculate the collision force. One example of this type of model is the Linear Spring-Dashpot model. Within the model, the normal force is broken down into the repulsive term (i.e. the spring) and the dashpot term that dampens the kinetic energy. The tangential force is calculated in a similar manner to the normal when modelling the elastic behaviour in the tangential direction. However, the total force calculated is limited by the Coulomb's frictional limit, representing the point at which shearing at the contact will be present [13]. The two major equations for each force component can be expressed as:

Normal force component: $F_n = k_n \Delta x + C_n v_n$ [9]

Tangential force component: $F_t = \min\{\mu F_n, k_t \int v_t dt + C_t v_t\}$ [10]

where k_n and k_t are the respective spring constants, Δx is the total overlap, C_n and C_t are the respective dampening coefficient based on the coefficient of restitution, v_n and v_t are the velocity components and μ is the friction coefficient.

2.6. CFD-DEM Coupling

CFD-DEM coupling is the method of solving the motion of discrete particles within a fluid domain, whilst recording the individual history of each particle. The motion of the particles is still calculated using Newton's second law motion. However it is extended to encompass the force of the fluid, as well as any other non-contacting forces; i.e. Van der Waals forces. The resulting can be written as:

$$m_i \frac{dv_i}{dt} = \sum_j F_{ij}^c + \sum_k F_{ik}^{nc} + F_i^f + F_i^g \quad [11]$$

$$I_i \frac{d\omega_i}{dt} = \sum_j M_{ij} \quad [12]$$

where m_i, v_i, ω_i is the mass, velocity and rotational velocity of particle *i*, F_{ij}^c and M_{ij} is the contact forces and torque of a particle *j* or wall that is acting on particle *i*. F_{ik}^{nc} is the non-contact forces exerted by another particle *k* or external

force onto particle *i,* F_i^f is the force a fluid acting on particle *i* and F_i^g is the force due to gravity.

The methodology was originally proposed by Tsuji *et al.* [14] and later refined by Xu and Yu [15]. The fluid and discrete phases are solved consecutively using an Eulerian-Lagrangian approach. However, during the resolution of the fluid phase, the scheme used to solve the system is that of an Euler-Euler approach [16]. The fluid is treated as a continuum and is solved using the locally averaged Navier-Stokes approach within the fluid cell. To predict the effect each phases has on one another, the volume-weighted average of the discrete phase is used within the pressure-drop calculation, hence a continuum-continuum solution. This can be seen in Figure 2-2 where the discrete media is represented as a fraction of the cell. Gidaspow [17] proposed two models when calculating the pressure drop:

Model A.

$$\frac{\partial \varepsilon}{\partial t} + \nabla.(\varepsilon \boldsymbol{u}) = 0 \quad [13]$$

$$\frac{\partial (\rho \varepsilon \boldsymbol{u})}{\partial t} + \nabla.(\rho \varepsilon \boldsymbol{u}\boldsymbol{u}) = -\varepsilon \nabla \mathrm{p} - F^A + \nabla.(\varepsilon \boldsymbol{\tau}) + \rho \varepsilon g \quad [14]$$

Model B.

$$\frac{\partial \varepsilon}{\partial t} + \nabla.(\varepsilon \boldsymbol{u}) = 0 \quad [15]$$

$$\frac{\partial (\rho \varepsilon \boldsymbol{u})}{\partial t} + \nabla.(\rho \varepsilon \boldsymbol{u}\boldsymbol{u}) = -\nabla \mathrm{p} - F^B + \nabla.(\varepsilon \boldsymbol{\tau}) + \rho \varepsilon g \quad [16]$$

where $\boldsymbol{u}$ is the fluid velocity, ρ is the fluid density, $\boldsymbol{\tau}$ is the Reynolds stress tensor, ε is the porosity of the fluid cell, g is the gravity constant, F^A and F^B are the fluid-particle interaction forces.

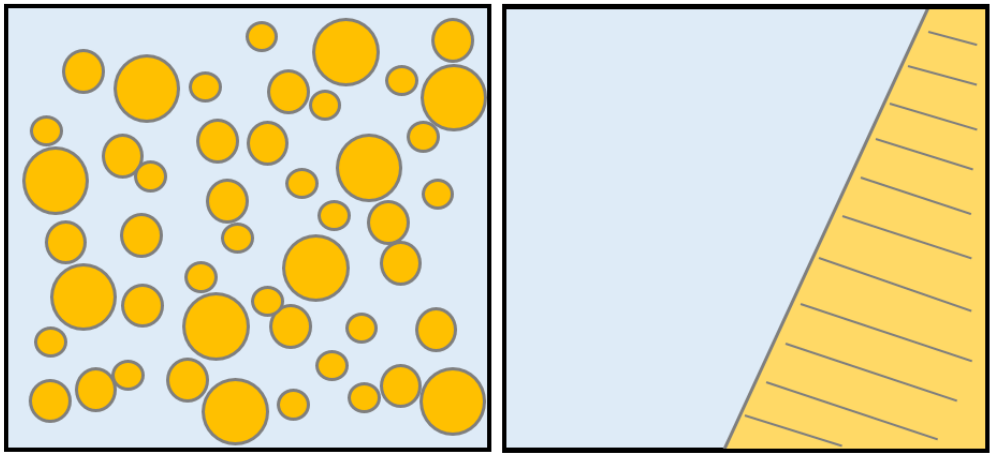

Figure 2-2: Schematic of conversion from discrete media (left) to a continuum (right) of a single fluid cell volume.

Once the pressure gradient and velocity of each fluid cell has been calculated with the fraction of solid material present, a new fluid drag constant for each corresponding cell is computed and passed back to the DEM solver. The drag force is treated as an additional body force acting on the particle and is used the next time the position of a particle is updated. The DEM solver will then update as many times as required using the calculated fluid drag force until the fluid field is updated once again. Norouzi *et al.* [16] recommend that the Rayleighs time-step should be between 10-40 times smaller than the fluid time step, i.e. the DEM solver will compute the particle field between 10 to 40 times before the fluid field is updated.

Finally, different schemes of coupling exist depending on the users preference or need, but is subject to whether the CFD is coupled to a Langrangian Particle Tracker (LPT) solver or a DEM solver. Since particle interactions can be neglected in LPT solvers, a total of four schemes exist to capture increasing levels of simulation detail [16].

2.6.1. One-Way Coupling

Only the particle are influenced by the fluid field, but do not affect it. Their presence on the fluid field is viewed as negligible and can therefore be ignored. If the fluid field is also considered constant, then it does not need to be recomputed after the DEM solver updated. One-way coupling is only suitable for dilute particle systems.

2.6.2. Two-Way Coupling

In two-way coupling, momentum is exchanged between the fluid and particle phases as outlined; i.e. the presence of one is able to affect the motion of the

other, and vice versa. This exchange of momentum makes this scheme suitable when there is a high concentration of particle present. Two-way coupling is also seen as sufficient to represent most cases when coupled with a DEM solver. Throughout this body of work a two-way coupling scheme is used, as EDEM^{TM} is employed to track both particle motion and collisions.

2.6.3. Three-Way Coupling

Three-way coupling refers to the consideration of particle collisions that can occur during a simulation, yet its use is only needed during LPT coupling since it can be neglected. When coupled with a DEM solver, collisions are handled outside the coupling scheme by the solver itself. Therefore, it is an unnecessary consideration. However, a two-way scheme is used to update the particle and fluid phases.

2.6.4. Four-Way Coupling

Four-way coupling schemes refers to a three-way scheme with the addition of fluid wake forces. Particles indirectly influence one another as they create eddies in the fluid that in turn create localised wakes.

Chapter 3 Literature Review

This section will discuss the background research regarding the spiral jet mill. The aim of this chapter is to give the reader a deeper understanding of how the spiral jet mill operates, introduce the key parameters that aid size reduction and predicting the product size. Any details that are necessary and related to a particular section of work will be included in the relevant chapter.

3.1. Operational Considerations

3.1.1. Grinding Gas Pressure

The grinding gas pressure is considered one of the main parameters that enables size reduction in the mill [18,19]. A number of studies report a decrease in particle size as the gas pressure is increased [4,20,21]. An increase in the grinding gas pressure, increases average gas velocity; in particular the relative tangential velocity component. The particles travelling inside the vortex experience an increase in momentum transfer from the gas and begin colliding with each other and the chamber walls at larger relative velocity compared to lower pressures. Therefore, accelerating breakage.

The grinding gas pressure also effects how particles break and final product produced by the mill. At low gas pressures, the vortex can become unstable and its shape oscillates, as the energy requirement is not met to sustain it. This allows for “shortcutting” of the mill, as particles travel radially along the base of the milling chamber and out of the mill. Müller *et al.* [4] reported an uneven classification size of particles as they decreased the grinding pressure.

Providing a high enough grinding pressure will stabilise the vortex [4]. However, at lower pressures, abrasion is dominant as the layers of particles shear over one another in the particle bed. Only once there is sufficient pressure delivered to the mill, the particles collide with a relative velocity that will allow for fragmentation to occur. This is because fragmentation is more destructive than abrasion, as it can lead to distribution of particle fragment, and hence, requires more energy. Therefore, as the pressure is increased, the dominant breakage mechanic changes, and fragmentation, not abrasion is most prevalent inside the milling chamber [21,22].

Since the grinding pressure can alter the major breakage mechanic, the final shape of the product can also be influenced in some instances. When

abrasion is dominates inside the mill, the particles can become more spherical. In contrast, Palaniandy *et al.* [22] found that when fragmentation is major breakage mechanic, particles can become more elongated in shape. This is because the particle break directionally down the most weakly bonded planes first, leading to a non-spherical shape. However, this suggests that the final shape of the particle is affected by the material structure when fragmentation is prevalent.

3.1.2. Material Feed Rate

Feed rate is the second most effective way to control the breakage rate, and therefore, the final product size distribution that exits the milling chamber. High feed rates result in the build-up of material in the mill and therefore, lower the acceleration time in between collisions and reduce the average velocity of the particles [4,21]. Dogbe, et al. [23] showed that as the particle number was decreased from 10,000 to 5,000, particles began colliding with greater kinetic energy and attributed it to increase in acceleration time in between successive collisions. Scott, et al. [24] showed a decrease in both the fluid velocity magnitude and the tangential component as the particle mass increased, which lead to an overall decrease in the particle velocity. It was reasoned that as the particle mass increases, more momentum is transferred to the particles form the air leading to a reduction in the gas field velocity.

3.1.3. Hold-up and Residence Time

During operation of the mill, there is a constant amount of material trapped within referred to as the hold-up. Increasing this instantaneous amount of material increases the probability of successful collisions between particles, and therefore, reduces the time required for the particle to spend in the mill [18,22]. That is until the average relative velocity of a collision decreases substantially enough that the breakage rate is negatively impacted, such as shown in the Dogbe [25]. Thus this indicates that there is an optimum set-up. The hold-up can also be increased by increasing the grinding gas pressure. Increasing the gas pressure leads to more efficient breakage, however, it also increases the tangential velocity component of the gas. The particles that should have been allowed to exit the mill at lower gas pressures now become trapped, as they travel with greater tangential velocity and their own momentum holds them in bed and circulating the mill.

Residence time describes the length of time needed for a particle to enter the mill, break, and become entrained in the gas flowing out of the mill. It is calculated by dividing the amount of material hold-up by the material feed rate.

Müller et al. [4] found that the time spent by particles in the mill decreased if the feed was increased during lean operations. However, they also showed the time became constant as the feed rate was increased further. As with hold-up, the resdience time of particles increases when the grinding gas pressure is increased. Increasing the relative tangential gas velocity decreases the size of particle that can sucessfully leave the mill [4,18].

3.1.4. Mass Loading

As described for the feed rate, the average relative velocity of a collision will decrease as the number of particles in the chamber increases and grinding pressure is held constant. However, as the number of particles deceases, the mill is said to be in 'lean' operation. This is where little material is circulating inside the chamber, and therefore, the particles have more space and time in between collisions. Both Mebtoul *et al*. [26] and Dogbe *et al*. [23] noted that when the mill is in lean operation particle-wall collision dominates breakage and size reduction. As the particle number increases and the bed grows in size, it becomes more probably that the particles will collide with one another. Hence, under normal loading conditions, interparticle collisions are most prevalent and account for the highest amount collisions that successfully lead to breakage.

3.1.5. Feed Gas Pressure

Katz and Kalman's [21] paper is one of the few pieces of work to consider the role of the feed gas pressure on particle breakage. They showed that when the feed gas pressure is sufficiently high breakage could still occur in the mill, even when the grinding pressure is very low. However, particle breakage occurs on entry into the chamber with the walls. Once the grinding gas pressure is increased once more, the effect of the feed gas on the fluid field becomes less pronounced. As a result, Ramanujam and Venkateswarlu [18] found no change in the product size distribution when they experimented with different feed gas pressure. The same findings were also concluded by Teng et al [27]. One final note on the feed gas pressure is that during operation, it must be set higher than the grinding gas pressure. If the feed gas is reduced significantly or shut off whilst the mill is in operation, then the feed flow will be reverse. This allows the material to escape using the feed pipe, as the feed port to the mill is usually at atmospheric pressure.

3.2. Design Aspects

3.2.1. Grinding Gas Nozzle Transport

MacDonald, et al. [28] describe three unique scenarios when transporting particles around the mill. The first and most ideal is when particles meet in the jet stream, as they particles collide with the highest relative velocity. However, this scenario relies on a particle being ejected from the bed and entering the proceeding jet region, only to collide with an accelerating particle.

The second scenario is a collision between two particles in the lean area of the mill and outside the jet regions. This collision is less preferable as the relative velocity of the collision will be lower, even though the particles may be travelling substantially faster than the particle in the bed. This type of collision occurs when the nozzles are placed too close together along the chamber wall.

The final scenario occurs when the angle of the grinding gas nozzles is too small relative to the outer wall. In this case, the majority of the particles collide and re-enter the particle bed before reaching the next jet. This phenomenon results in a reduced relative velocity during particle collisions and leads to decreased breakage by fragmentation. However, since particles travel for larger periods in the particle bed, size reduction by attrition is increased.

3.2.2. Nozzle Angle

Rodnianski, et al. [29] found that 54° relative to wall was optimum for their set up. Their finding show that the nozzle angle had minimal effect on the radial velocity component of the gas. Therefore, lowering the angle would increase the tangential component, but could hinder the transport of particles from one jet to the next. This finding was substantiated by Tuunila and Nyström [19]. They showed that breakage effiency increased when the nozzle anagle was increased from 23° to 43°. The Hosokawa micron AS-50 nozzle angle is set to 50° relative to the wall. Unlike the larger mills in the AS range, the AS-50 the nozzle angle cannot be altered. Hence, no investigation regarding nozzle angle could be investigated using this mill.

3.2.3. Nozzle Size

Both Katz and Kalman [21] and Rodnianski, et al. [29] suggested that reducing nozzle size is beneficial for breakage when the gas pressure is held constant, as it results in collisions with increased relative velocity. Rajendran [20] did show enlarging the gas nozzles can increase milling efficiency, as it creates a larger jet area, and therefore, more particles can be accelerated towards the

mill centre. However, the paper also concludes that widening the nozzles is less effective than narrowing the nozzle size to increase the rate of size reduction. Nair and Ramanujam [30] findings are comparable to others on the topic of nozzle size. They analysed a number of different configurations and found smaller nozzles using high pressure at low energy throughput leads to improve size reduction, when compared to a set of larger nozzles using a lower pressure.

3.2.4. Nozzle Number

Teng, et al. [27] found using six nozzles was preferable to using just two nozzles, as they were able to increase the energy input more efficiently into the milling chamber. They noted decreased wear along the walls of the chamber when six nozzles were used. This leads to the conclusion that increasing the number of nozzles is preferable for size reduction. Rodnianski et al. [29] showed that a smaller number of nozzles is better for milling performance. However, their work considered eight nozzle configurations ranging from 1-18 nozzles. Figure 3-1 is an example of a spiral jet mill with 12 nozzles, as used by Rodnianski et al. [29].

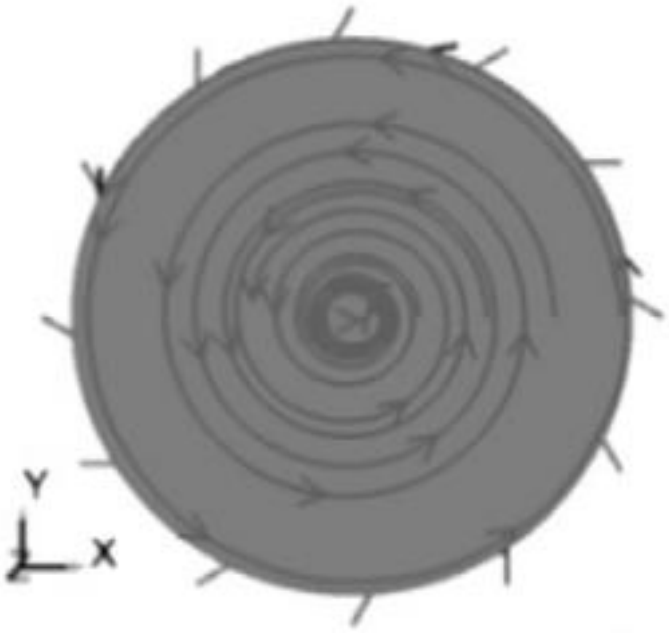

Figure 3-1:Image of a spiral jet mill with 12 grinding jet nozzles. Taken from Rodnianski et al. [29]**.**

In their work, they describe the relationship of tangential gas velocity to its radial component, which they term the spin number. The spin number $\left(\frac{v_t^2}{v_r^2}\right)$ is expressed as:

$$\frac{\boldsymbol{v}_t^2}{\boldsymbol{v}_r^2} = f(\alpha, d, h, n, r, \dot{m}) \quad [15]$$

where $\boldsymbol{v}_r, \boldsymbol{v}_t, \alpha, d, h, n, r$ and $\dot{m}$ are the radial gas velocity component, tangential gas velocity component, nozzle angle, nozzle diameter, chamber height, nozzle number, chamber radius and mass flow rate, respectively. They found that the spin number decreased when the number of nozzles was increased. This decrease was detrimental to size reduction, as particle leaving the mill were larger.

Luczak, et al. [31] analysed three different nozzle numbers configurations, these were 4, 8 and 12 nozzles. They showed that the jet region elongated when fewer nozzles were used, leading to an increase in milling efficiency.

3.2.5. Classifier Ring

The classifier ring is an inner wall that partially shields the exit of the milling chamber, leaving only a small gap that allows the gas and particles to escape. It is also referred to as a vortex finder, which are commonly found in cyclone [4,32]. As particles travel closely around the ring, they are accelerated due to the increasing gas velocity in proximity to the vortex finder. This causes separation of the particles by size; those that are small enough are entrained out of the mill, whilst those too large are carried back towards the bed by the centrifugal force exceeding the radial drag force. This was shown by Luczak, et al. [31] using particle velocimetry. The classifier ring can either create a constriction at the base of the mill, or close to the ceiling, as is found inside the Hosokawa micron AS-50. Müller, et al. [4] found that increasing the diameter of the classifier ring improved separation, as the surrounding gas velocity increased due to the decrease in volume available. In the work by MacDonald, et al. [28], they describe the classifier indirectly by the free space it creates. They found that as the product size is proportional to the the size of the constriction, as decreasing the gap improved classification.

3.3. Cut Size

The circular motion of the particles in the mill is due to the fluid drag force created by the inclined gas jets that forms a vortex in the milling chamber [21,29]. The particles ejected by the gas jets travel towards the centre of the mill; however, if they are too large, then they are carried back towards the wall by their momentum. By knowing the mass of the particle and gas velocity components, it was Dobson and Rothwell [33] who first reasoned a cut-size could be predicted. The cut-size is the common name for the particle size d_{50};

the median diameter at which all particles under that value will be removed from the mill. To estimate the cut-size, it is assumed that the tangential velocity of a particle is close to the tangential velocity of the gas in which it is entrained. This assumption simplifies the force balance needed to calculate the cut size and results in following set of equations:

Centrifugal force: $\boldsymbol{F} = \frac{\pi}{6} d_{cut}^3 \rho_P \frac{v_t^2}{r}$ [16]

Radial drag: $\boldsymbol{F} = \frac{\pi}{8} C_D d_{cut}^2 \rho_g \boldsymbol{v}_r^2$ [17]

which simplifies to:

$$d_{cut} = a \cdot \frac{v_r^2}{v_t^2} \quad [18]$$

where $a = \frac{3}{4} C_D r \frac{\rho_g}{\rho_p}$, d_{cut} is the maximum diameter of any particles that can leave the mill, C_D is the drag force coefficient, r is the radial distance, ρ_g and ρ_p are the densities of the gas the particles, and $\boldsymbol{v}_r$ and $\boldsymbol{v}_t$ are the radial and tangential gas velocity components.

One problem with the approach described by Dobson and Rothwell [33] is that it still requires the trial and error to achieve the correct product size. As described, the material feed rate and grinding gas pressure are the two principal parameters that dictate the rate of size reduction, yet they are not present in the prediction of the cut size. Müller, et al. [4] suggested that the force balance between radial drag of the gas and momentum of the particle could be simplifed further and include aspects of the mill and gas input:

$$\frac{\rho_g}{2} c_D \frac{\pi}{4} {d_{cut}}^2 v_r^2 = \rho_p \frac{\pi}{6} {d_{cut}}^3 \quad [19]$$

where v_r is:

$$v_r = \frac{Q}{\pi d_v h} \quad [20]$$

and Q is the volumetric gas throughput, d_v is the diameter of the classifier and h is the height of the milling chamber. However, there is an issue with this approach, as the equation is now dimensionally inconsistent and an acceleration term appears to missing on the right-hand-side.

Within the same study, the group investigated four different sized mills. The size of each milling chamber used was 80, 170, 450 and 800 mm. The authors write that they scaled pressure so that comminution remained constant across all four mills. This led to classification being dependant on the diameter of the classifier ring and led them to derive the following relationship:

$$d_{cut} = \left(\frac{\boldsymbol{v}}{\boldsymbol{v}_r d_v}\right)^{\frac{3}{8}} \left(\frac{\rho_g}{\rho_p}\right)^{\frac{5}{8}} \left(\frac{\boldsymbol{v}_r}{\boldsymbol{v}_t}\right)^{\frac{5}{4}} d_v \quad [21]$$

where $\boldsymbol{v}$ is the particle velocity. Finally, they related the tangential gas velocity to mass of material entering the mill through a dimensionless number K:

$$K = \mu^{0.5} \frac{PD^4 \rho_p}{Q_m} \quad [22]$$

where P is the grinding gas pressure, Q_m is the mass throughput of gas and μ is the fractional mass throughput of solids. It can be seen in the paper how the tangential velocity relates to the dimensionless number K, however, they do not offer an explanation as to how they arrived at this result. However, the relationship between K and the tangential velocity has been used again by Rodnianski, et al. [29], in which they arrive at the relationship:

$$v_t = \beta \cdot [K]^{-1.3} \quad [23]$$

where β is the breakage propensity constant for a material.

MacDonald, et al. (2016) approached calculating the cut-size in a different manner. They formed a relationship between the specific energy that is consumed during size reduction to the mass flow rates of the gas and solid material. From their work, they derived a semi-analytical correlation for the cut-size:

$$d_{cut} = \left(\frac{h_1}{h_2}\right)^2 \left(\frac{C_2}{s_n^2} + \frac{x_1 k}{s_n^2 d_{Reynolds} \dot{m}_g} + \frac{C_2 \dot{m}_s}{s_n^2 x_2} + \frac{x_1}{s_n^2 d_{Reynolds} x_2} \frac{1}{E_{sp}}\right) \quad [24]$$

where h_1 is the height of the free space in between the classifier ring and grinding chamber ceiling, h_2 is the height of the chamber before the classifier ring, $\dot{m}_g$ is the gas mass flow rate, $\dot{m}_s$ is the solids mass flow rate, $d_{Reynolds}$ is the Reynolds length scale; a number used to describe the size of high-energy eddies, E_{sp} is the specific energy consumed to operate the mill and S_n is the spin number $\left(\frac{v_t^2}{v_r^2}\right)$. C_2, k, x_1, x_2 are correlations and individual constants, that relate the particle and gas properties; see Macdonald et al. [28].

The issue that remains with this method of predicting the cut-size is that it relies upon calculating or measuring the tangential velocity component of the gas. This is something that is not directly discussed commonly in the literature given the difficulty. In one paper, Tanaka [34] reasoned that around the classifier ring the gas should follow the path of an Archimedes spiral. Form this assumption he derived the equation:

$$v_t = k_2 \left(\frac{Q}{D^2}\right) \left(\frac{D}{d_j}\right) \left[\left(1 - \frac{D_o}{D}\right) - 2k_3 \left(\frac{d_j}{D}\right) \cos(\alpha)\right] \quad [25]$$

where D is the diameter of the milling chamber, D_o is the diameter of the outlet, d_j is the diameter of the nozzles, k_2 and k_3 are both dimensionless constants, and α is the angle of the grinding nozzles with respect to the outer wall. However, Rodnianski, et al. [29] did not find this correlation to fit well when compared to their own model after computing the theoretical tangential velocity.

Chapter 4 Preliminary Work

4.1. Mill Design

During the original design of the in-house CAD model, only the milling chamber and nozzle size and position were accurately modelled from measurements taken of the Hosokawa Micron AS-50. The grinding nozzle dimensions are critical as they dictated the high-pressure gas flow into the mill and nearest the wall. However, when creating the mesh, the fluid cells cannot be too small due to the presence of particles that would be simulated over the fluid field. The first iteration of the fluid mesh can be seen in Figure 4-1.

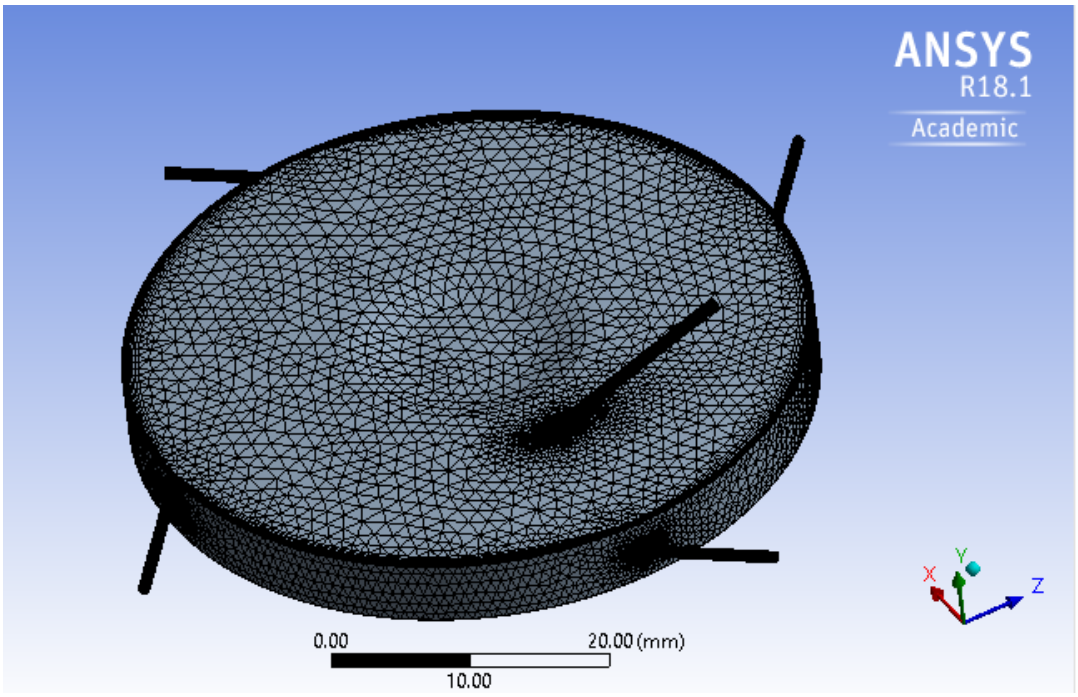

Figure 4-1: CFD mesh of mill during the initial set-up

To establish when the meshing component is complete, it is standard to carry out a mesh independence study. During a mesh independence study, the mesh is altered until the fluid field no longer changes based on the size of the fluid cells. The process requires knowledge of how the fluid will flow through the geometry and what behaviour is most relevant to capture, to optimise the total cell number. For the mill, it is important to capture the fluid behaviour around the outer wall, due to the dynamics of the jets and presence of the particle bed. During mesh independence simulations it is also common to use different turbulence models as they might affect the flow dynamics. This step was followed and confirmed the previous work of Dogbe [25], who found that the *k-ε* model was sufficient to capture the behaviour of the fluid, whilst

maintaining accuracy and lowering the overall simulation time needed. The RSM model was used in the comparison; however, there was no noticeable difference in the fluid flow field for the increase in time taken. The boundary conditions as well as the other main parameters used are given in Table 1.

Table 4-1: Parameters used during the mesh independence study

Turbulence model	k-ε
Solver	Pressure-based; Transient
System	Air
Gas law	Ideal gas law
Compressibility	Compressible
Grinding pressure (bar)	3.0
Feed pressure (bar)	3.2
Outlet pressure (bar)	1.01
Time-step	10^{-4} - 10^{-6}

To assess when mesh independence has been achieved, the velocity profile was recorded through the mill once the fluid field had been solved. However, it is an iterative process, as the geometry must be re-meshed and solved each time a change is made to one of the meshing parameters. A number of profiles depicting the tangential velocity can be seen in Figure 4-2.

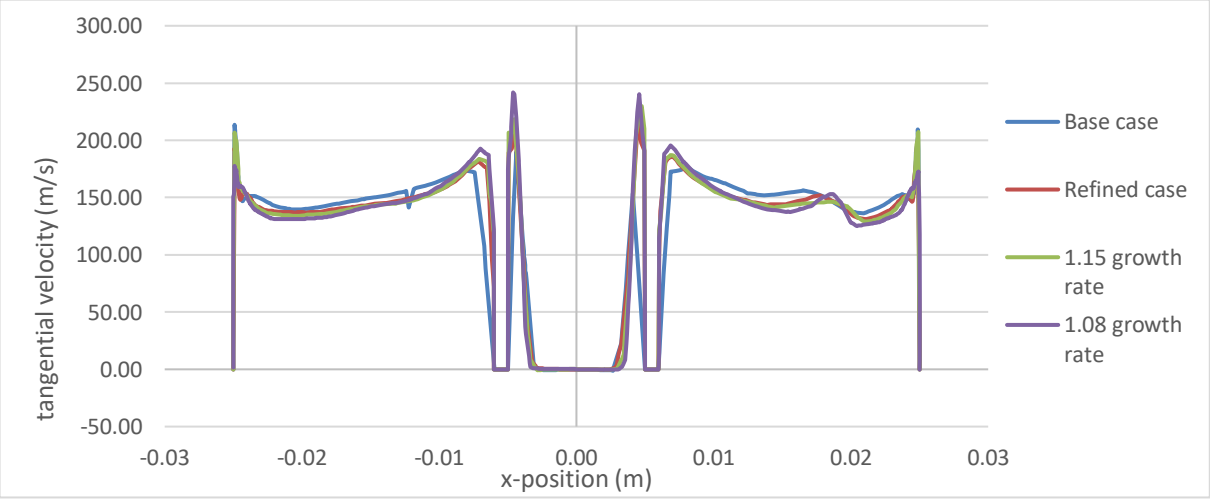

Figure 4-2: Tangential gas velocity profile from across the milling chamber.

The base case was the unrefined mesh before any modifications were made. Next, refinement was made to mesh layers around the outer wall. This was achieved using an inflation rate that grows the cell diameter by a certain fraction based on the previous layer. This is referred to in Figure 4-2 as the growth rate. The mesh independence study was concluded at a growth rate of 1.08, as there was a small degree of change from the refined case. However, many small optimisations were made to achieve the final mesh, such as setting the global minimum and maximum cell sizes and meshing individual sections separately.

4.2. Mill Redesign

After some initial simulations, the mill was redesigned to represent the Hosokawa micron AS-50, which can be seen in Figure 4.3. Inside the milling chamber, the hemispherical section with the conical vortex finder was added. The gas flow is now constricted upwards and circulates the vortex finder, before changing direction and travelling down the exit pipe. Another change made to the milling chamber was the sloping base of the chamber. The base slopes downwards towards the centre and increases the maximum height of the chamber directly before the particles are classified out of the mill. This design feature aids classification and stops larger particles escaping.

The next feature to be changed was the annular gas manifold ring that feeds each of the grinding gas nozzles. Dogbe [25] found that this feature was important to include, when compared to simulating the nozzles that are fed individually. The reason found was that depending on the position of the bed and local build-up of particles around the jets, the upstream pressure behind the jet will change. Hence, it will have a direct impact on the fluid flow field inside the chamber, as the gas pressure equalises around the other three jets.

Finally, the hopper section was added and improved upon from Dogbe [25] own work. The hopper section was difficult to design, as there was no plans available, so a limited number of measurements could only be made. The gas feed nozzle was particularly difficult to place as it must be positioned the correct distance to induce a vacuum, yet far enough away from the feed pipe that it does not cause recirculation in the small chamber.

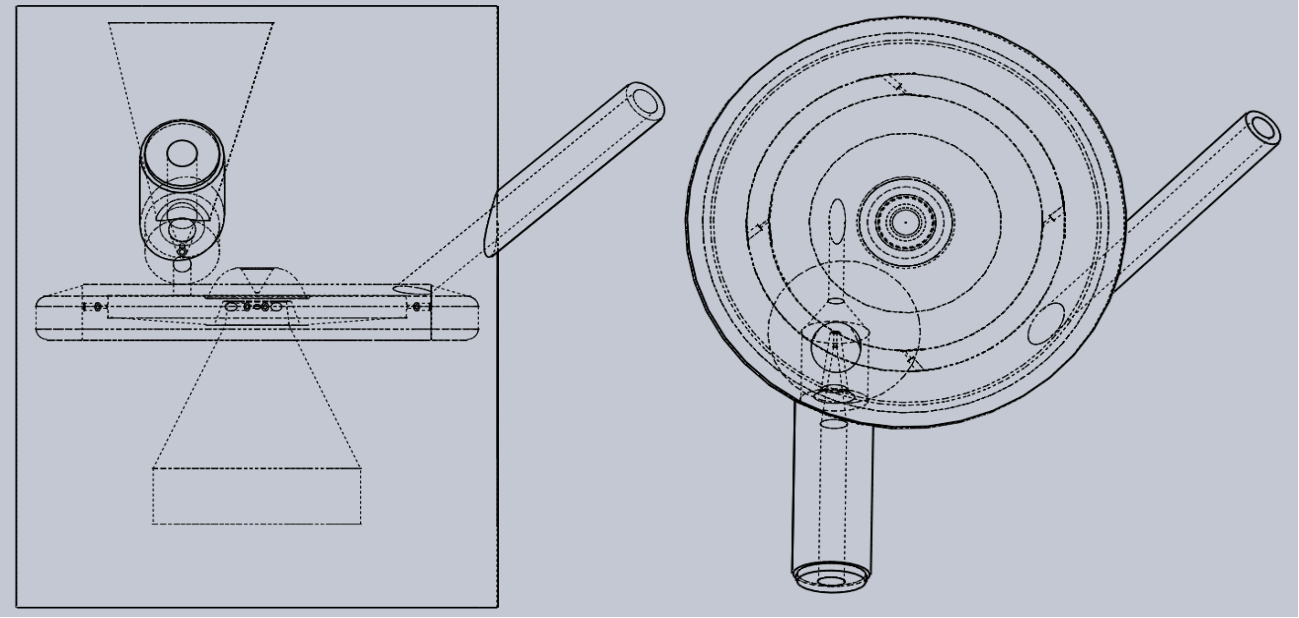

Figure 4-3: Face-on (left) and top-down (right) views of the mill after all modifications had been made.

Error! Reference source not found. depicts the dimensions (mm) of the mill as a 2-D drawing. Thedrawing is then extented around a central axis to create the hollow space of the mill. For clarity the measurement R0.40, is the radius of the arc from an imaginary central point. The 0.10 measurement is the radial thickeness of the vortex finder tip. Finally, the ceiling surrounding the vortex finder is created using a single curved line using specified measurements as shown.

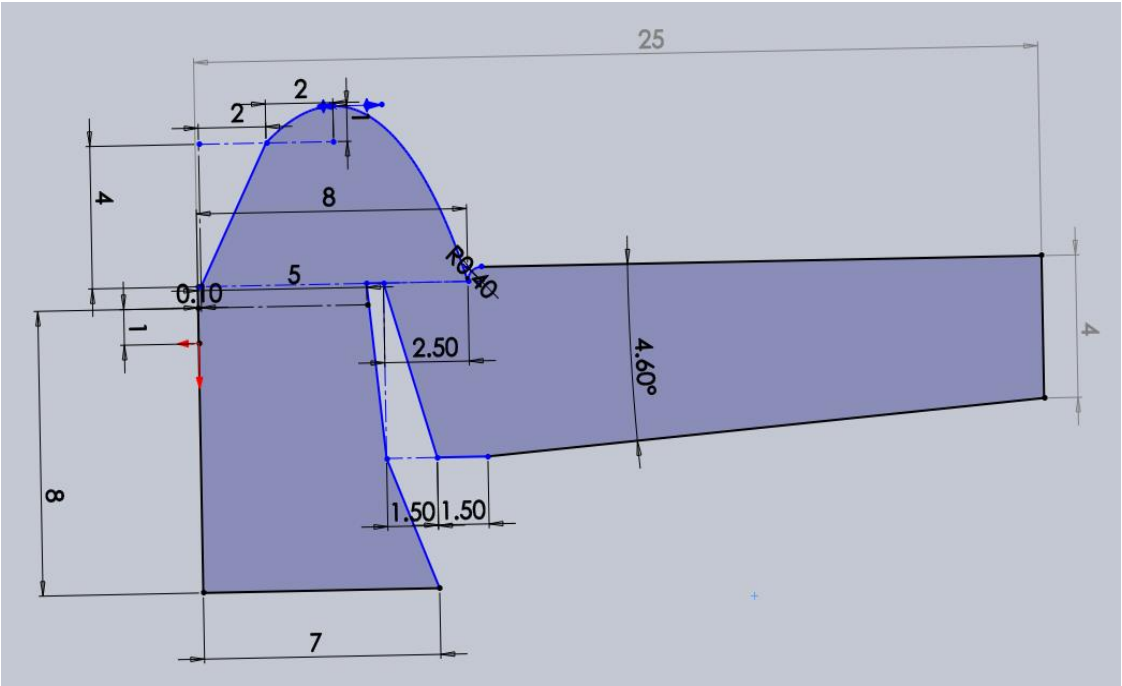

Figure 4-4: Two dimensional CAD drawing of the mill. Dimensions given in mm.

Chapter 5 Hold-up and gas/particle flow regimes

5.1. Introduction

Whilst the design and operational parameters of the spiral jet mill have been researched extensively, the underlying mechanics of size reduction in the mill remain poorly understood. This is largely because of the complex flow regime inside the milling chamber and material properties that influence breakage. Overall, the mill is very simple to operate. However, it is difficult to tune size reduction without a trial and error approach. This is because slight variations in the feed material or gas pressure will change the flow dynamics in the milling chamber. Kürten and Rumpf [35] carried out some of the earliest experiments to analyse the flow regimes in the spiral jet mill using triboluminescence; closely investigating the jet regions (area of high velocity gas directly in-front of the grinding nozzles). They found that size reduction was favoured along the *Rückseite* (backside) of the jet; i.e. the side at which particles exit the jet and return to the bed. However, this did not meet their expectations, as they had theorised that size reduction should be prevalent along the *Vorderseite* (frontside) of the jet [36]. This is because the material should be entering the jet from the frontside, and therefore, will come in contact will other particles before reaching the backside of the jet region. Luczak [37] showed this to be true using particle image velocimetry. Breakage is favoured along the frontside of the jets, as particle enter the jet region and collide with other accelerating particles.

Equally, analysing hold-up and it role on size reduction remains problematic. The bed itself is always in a state of flux, as the material rotates around the mill. The jets propel particles from the bed, which later re-enter if they are too large to leave. Hence, the bed is not just in motion, but also its mass changes with time. Furthermore, the particle bed has its own velocity gradient, as the layers of the bed shear over one another due to the varying gas pressure at different positions. Müller, et al. [4] investigated residence time using a radio-active tracer. They found that the amount of hold-up decreased as the grinding pressure increased and were able to correlate their findings with an empirical equation for the cut-size. However, this equation included gas throughput and the mass fraction of solid material. It does not relate the hold-up to the gas flow regime in the mill. In the work by Luczak [37], they analysed how hold-up was effecting particle acceleration in the jetting region using particle image velocimetry. They showed that as the amount of hold-up increased, the

particles in the jetting regions began to become impeded, as they with other particles before being exiting the bed.

Given how difficult it is to obtain data form the spiral jet mill, it should be easier to simulate a spiral jet mill. However, that is not the case. The difficulty with DEM simulations is that a very small particle size is needed to predict the dynamics of the material bed and the liberated particles in the jet regions and lean section (region of the milling chamber that surrounds the classifier). The computational requirements increase as particle size decreases and particle number increases, resulting in what is feasibly possible given the hardware available to the user. Therefore, this has often led to simplifications in an effort to reduce computational power [23,38–40]. Rodnianski, et al [29] only simulated the gas component of the mill in conjunction with physical experiments to predict classification. They produced a predictive model for the cut-size using the velocity component ratio $\left(\frac{v_t^2}{v_r^2}\right)$ of the gas they termed the spin ratio. Where v_t is the tangential velocity component and v_r is the radial velocity component used to describe the direction of the gas in the forward and inward direction, respectively However, they concluded that CFD is only possible at predicting the fluid flow field when there is no particle hold-up present. Teng, et al. [41] analysed particle collisions, and found that contact force was eight-times greater (8x) in the tangential direction compare the normal component. Therefore, they suggested that particles collide with a “side-swipe” action. This finding led to collision that abrasion was dominant cause of size reduction in their mill. However, they only simulated 1000 particles. This would have created a very dilute system and not reflective a standard mill in operation. Brosh, et al. [42] managed to successful simulate a spiral jet mill using Fluent as CFD component and an in-house DEM code. Later, Brosh, et al. [43] included breakage by particle fatigue and impact. However, they resulted in artificially lowering the particle stiffness to decrease computational time. They also removed particle directly out of the simulation once they achieved a certain size.

Dogbe [25] and Dogbe, et al. [23] simulated enough material that they were able to show the point at which inter-particle collisions become the dominant mechanic for energy dissipation that would lead to size reduction. However, Dogbe [25] also reported that although they used a suitable amount of solid material and particle size distribution, no particles were able to leave the mill during the simulations. Bnà, et al. [40] used a one-way coupled CFD-DEM scheme to predict classification size. They found good agreement with the cut-size equation proposed by Dobson and Rothwell [33]:

$$r_{cut} = \frac{3}{4}\frac{c_d \rho_g r_c}{\rho_p}\left(\frac{v_{r,g}^2}{v_{t,g}^2}\right) \quad [28]$$

where r_{cut} is the cut-size radius of the particles, r_c is the radius of the classifier, c_d is the particle drag force coefficient, $v_{r,g}$ and $v_{t,g}$ are the radial and tangential components of the gas velocity, and ρ_g and ρ_p are the gas and particle density, respectively. However, Bnà, et al. [40] express that the one-way coupled system is only sufficient to predict particle cut-size when it is being operated as a classifier. The issue at larger particle loading is that the particles dampen the fluid field and alter the local velocity of the gas. This necessitates a fully coupled CFD-DEM scheme to capture all fluid-particle and interparticle behaviour that occurs.

This study investigates the role of hold-up on the fluid flow field and influence on particle dynamics. To achieve this, a 4-way coupled CFD-DEM is used and a range of mass loadings is analysed. There is no breakage model present in this study and particle size is too large for classification to be feasible. However, inter-particle and particle-wall collisions are analysed as a function of kinetic energy dissipated, and classification is addressed by analysing the fluid flow field surrounding the classifier.

5.2. Methodology

The AS-50 spiral jet mill is simulated using a four-way coupled CFD-DEM simulation. The milling chamber is 50 mm in diameter with four angled jet nozzles to provide the gas necessary to create the vortex. In Figure 5-1, both the CAD drawing (left) used to create the simulated geometry and EDEM geometry (right) with the particle factory are shown. Further information on the mills design and operation is given in Chapters 1 & 4. However, one feature of the mill that is important to this study is the annular gas feed section surrounding the milling chamber. Dogbe [25] found that the fluid field fluctuated due to particle mass in-balance in the mill, which was not present when it was not included.

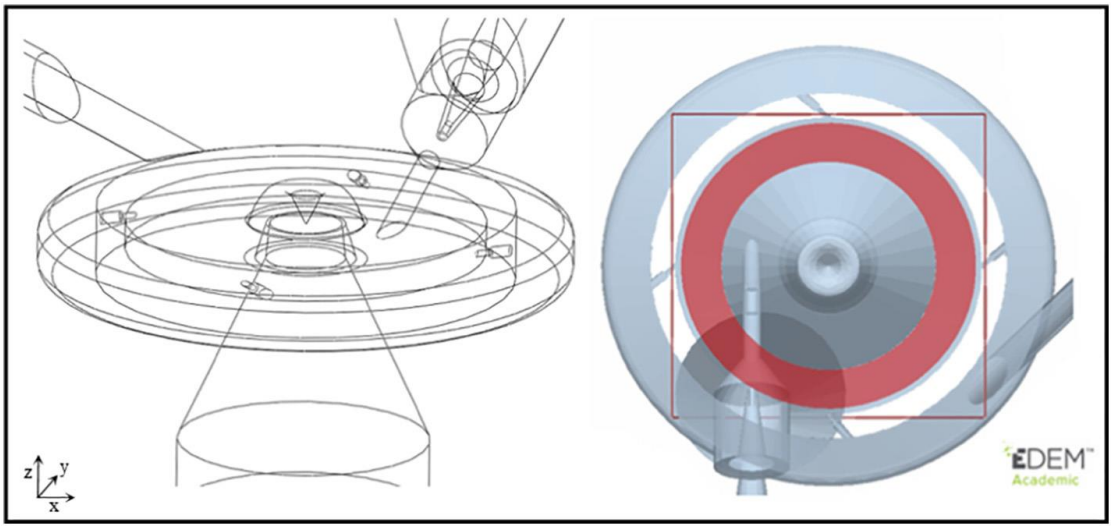

Figure 5-1: In-house CAD drawing of the Hosokawa Micron AS-50 mill (left). Empty simulated geometry (right) with particle factory highlighted (red) [24].

Within this study, the particles are not feed using the hopper, but added directly into the milling chamber using the EDEM™ particle factory. The material addition rate varies depending on total mass added. To ensure all particles are added by 0.01 s, the mass addition rate was changed for each simulation. The particle motion is simulated using the DEM software EDEM™ 2019 (Altair, UK). The particle simulated were single spheres using the Hertz-Mindlin contact model [11]. The time step was varied in between simulation based on the number particles being simulated. However, the time step never exceeded 25% of the Rayleigh's time step.

The fluid flow field is resolved using ANSYS Fluent 18.1 and the k-ε-RNG turbulence model with scalable wall functions. The gas density is calculated using the Ideal gas law. A tetrahedral mesh pattern is used for the fluid cells. The minimum cell size is based on the maximum particle dimeter (300 µm) present. To calculate the minimum cell size that can be used, a 40% cell-to-particle ratio is employed as suggested by Norouzi, et al. [16]. To capture the effect of the particle volume on the fluid domain, the Morsi and Alexander [44] fluid drag law was used. As EDEM™ 2019 was used for the particle tracker and collision handler, there is no further action required to capture all fluid-particle interactions in the simulation. The coupling scheme is based on the work of Tsuji, et al. [45] and Xu and Yu [15].

Five mass loading are investigated in this study. The list mass loading used, as well as the particle number and size distributions can be seen in Table 2. The associated particle and fluid properties can be viewed in Table 3. The fluid field is first resolved without the particles present. A pressure of 3 barg

for the grinding pressure has been selected, with an feed pressure of 3.2 barg. This pressure may be considered low for a mill operating under normal conditions. However, the mill has been simulated and researched extensively at that particular pressure [23,25]. Hence, the reason for its selection. After the fluid field has finished solving, the particles are added and bed is allowed to form and reach a pseudo-steady-state. After a period of time has passed (0.03 s), data collection can begin up until the simulations are stopped at 0.1 s.

Table 5-1: Mass loadings investigated and size distribution used in the simulations.

Mass loadings (g)	0.4, 0.8, 1.2, 1.6, 2.0	
Particle diameter (μm) and size distribution (wt%)	300	20
	240	40
	200	20
	160	20
Number loading for each mass loading (g)	0.4	54321
	0.8	111005
	1.2	168013
	1.6	224206
	2.0	280366

Table 5-2: Fluid and particle properties and simulation condition used in the investigation.

Phase	**Parameter**	**Value**
Fluid	System	Air
	Viscosity, Pa/s	1.8×10^{-5}
	Grinding nozzle pressure, kPa	300
	Feed nozzle Pressure, kPa	320
	Outlet Pressure, kPa	
	Fluid time step, s	$8 \times 10^{-6} – 2 \times 10^{-5}$
	Minimum cell edge length, μm	670
	Equation of state	Ideal gas law
Particle	Density, kg/m^3	1500
	Shear modulus, MPa	10
	Poisson’s ratio	0.25
	Coefficient of restitution	0.5
	Coefficient of static friction	0.5
	Coefficient of rolling friction	0.01
	DEM time step, s	$4 \times 10^{-7} – 1 \times 10^{-6}$

5.3. Fluid Field

The fluid velocity gradients can be seen in Figure 5-2. Each contour plot depicts the velocity magnitude for it respected mass loading. It cannot be seen, but the velocity of the air entering the milling chamber is around 300 m/s. However, the velocity in each of the contour plots has been clipped to enhance recognise of the lower velocities. The velocity depicted ranges from zero to 100 m/s. There are three regions in the mill, which are visible in each plot; these are the particle bed, the lean phase, and the gas region directly before the classifier ring. The slowest region in the mill is depicted in dark blue in ranges up to maximum of around 10 m/s. The green zones correspond to a velocity of around 50 m/s, whereas the red regions of the mill depict a velocity of 95+ m/s.

Along the wall of the milling chamber, the air is denoted in dark blue. This indicates that air is much slower in the presence of the particle bed. The fluid field in this position experiences a large amount of particle damping, which results in air moving much slower through this region of the mill. Moving radially from the wall, the colour of the contour plot turns light blue indicating that the velocity is increasing. There is still an amount of particle damping in this position, however, this region is still exposed to the air exiting the jet regions, and therefore, is higher than within the bed. Moving further into the mill, the contour plot changes colour once again to green. This section of the mill is the lean region. In this region there an insignificant amount of particles, which can dampen the vortex and alter the velocity profile of the gas. Moving inwards once again, the colour of the contour plots shift once more. This time to yellow, orange and then red. Here a free vortex is formed due to the air travelling closely to the classifier ring. The air is directed upwards into the hemispherical section, before it is redirected back down due to the presence of a conical vortex finder. Compared to the work of Luczak [37] and Luczak, et al. [31], there is good qualitative agreement with the fluid field data they recorded, despite the fact that a different mill size and nozzle configuration was used.

In the 2.0 g case, the boundary layer between the dense bed and lean regions of the mill is very distinct. Most of the particles now reside in the particle bed, which is indicated by the large dark blue section of the image. The jets have also shortened in length and no longer penetrate as far into the chamber, due

to the effect of the particles dampening the fluid field. At the lowest mass loading (0.4 g), the jets extend past the bed and through the lean region. The 1.2 g case produces a jet length somewhere in between of these two cases.

As the jet penetration length decreases, so too does the velocity of the free vortex surrounding the classifier ring. The gas velocity in the 0.4 g case approaches 100 m/s, whereas the velocity of the air does not reach 80 m/s once the mass loading is increased to 2 g. The size of the area occupied by the fast moving air also decrease as the mass loading is increased from 0.4 – 2.0 g. However, the particles in this simulation are too large to travel towards the centre, and therefore, any that do by chance would cause such a change in fluid low field. Hence, the change in the area and velocity of the free vortex is due to the size of the particle bed. As the mass loading increases, more momentum is between the air and particles, and the ability of the jets to penetrate through the bed is diminished.

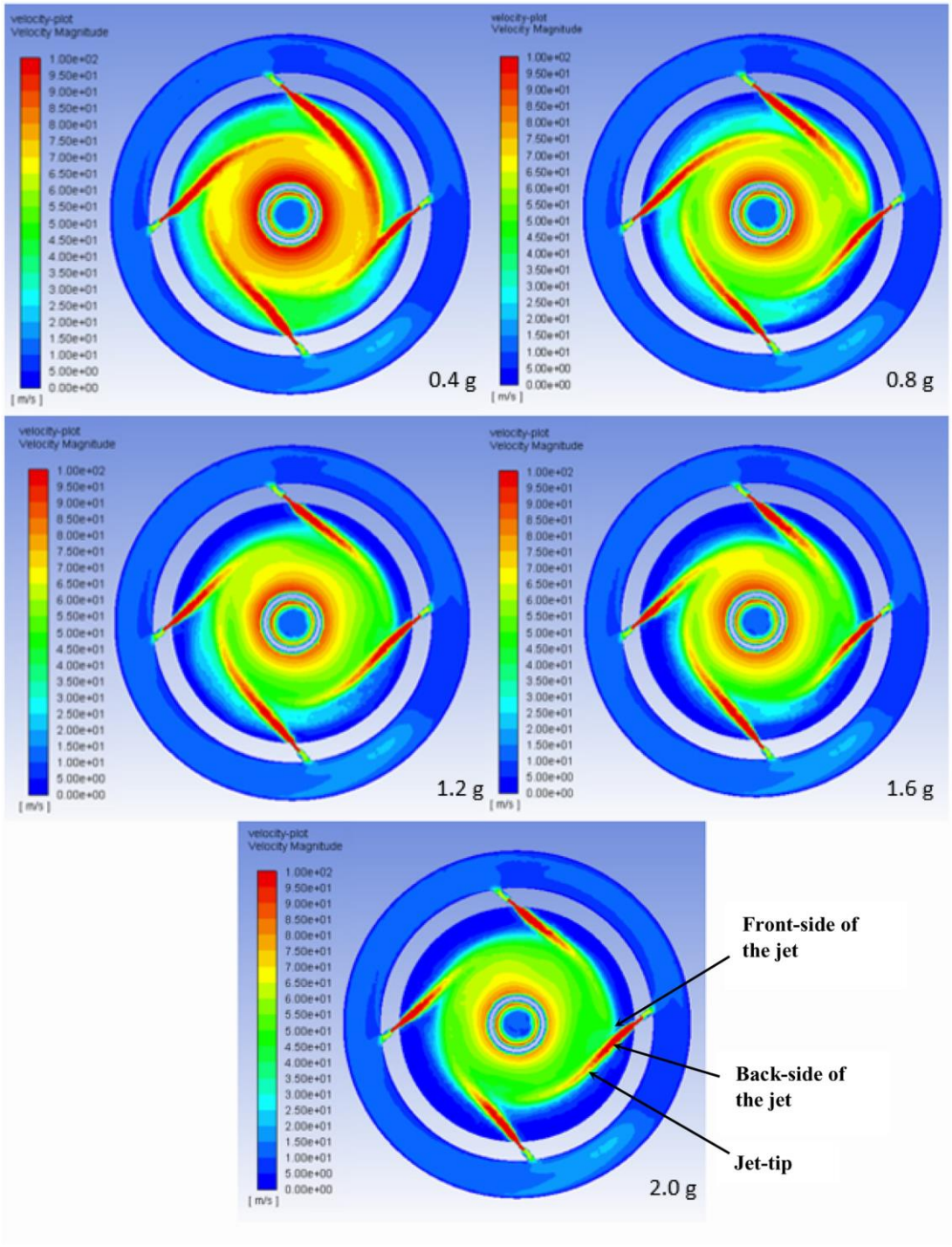

Figure 5-2: Velocity gradient in the mill as a function of velocity magnitude and mass loading.

To highlight this phenomenon more, the radial and tangential velocity components of the air have been plotted in Figure 5-3. Images (a) and (c) depict the radial velocity component of the gas for the 0.4 and 2.0 g cases, respectively. The velocities have once again been limited to aid visualisation of key area, which would otherwise not be visible due to velocity gradient present. In the 2.0 g case, the velocity is largely positive (between 10-25 m/s)

around the jets. This suggests the air around the jets is moving outwards and entrainment into the jets. In most other positions in the chamber, the velocity is around 0 m/s, with the exception of the jets. Along the jet length, the radial velocity is negative, indicating direction towards the mill centre. In comparison, the 0.4 g displays a largely negative radial velocity in the lean section of the mill, with the exception of the velocity behind the jet at the 3 o'clock position. The tangential velocity is shown in images (b) & (d) for the 0.4 g and 2.0 g cases, respectively. The velocity has been limited once again to -120 – 20 m/s, to highlight key areas in the chamber. The tangential velocity component is much greater than the radial; hence, this is the reason why the profiles correspond to the velocity magnitude of the respected cases in Figure 5-2. Comparing the two images, the effect of solid material hold-up is clear. There is a shortening of the gas jet length, as the bed impedes the high-pressure jet reaching the centre. There is a high amount of momentum transfer between the fluid and particles, as the space occupied by the bed decreases the velocity of the air in that position. The combination of these two points results in the free vortex tangential velocity decreasing. It is also noteworthy that the fluid flow field is not symmetrical. This is caused by the position in the feed pipe, which is located at the 9'clock position.

Overall, the fluids ability to drag particles to the centre of the mill increases as the mass loading also increases. The larger tangential component decreases, as the mass loading increases and radial component compensates to preserve the volumetric flow of air. Theoretically, this shift in tangential to radial velocity would increase the cut-size due to the component ratio $\left(\frac{v_t^2}{v_r^2}\right)$. However, the particles used in these simulation were too large, and therefore, this prediction could not be verified.

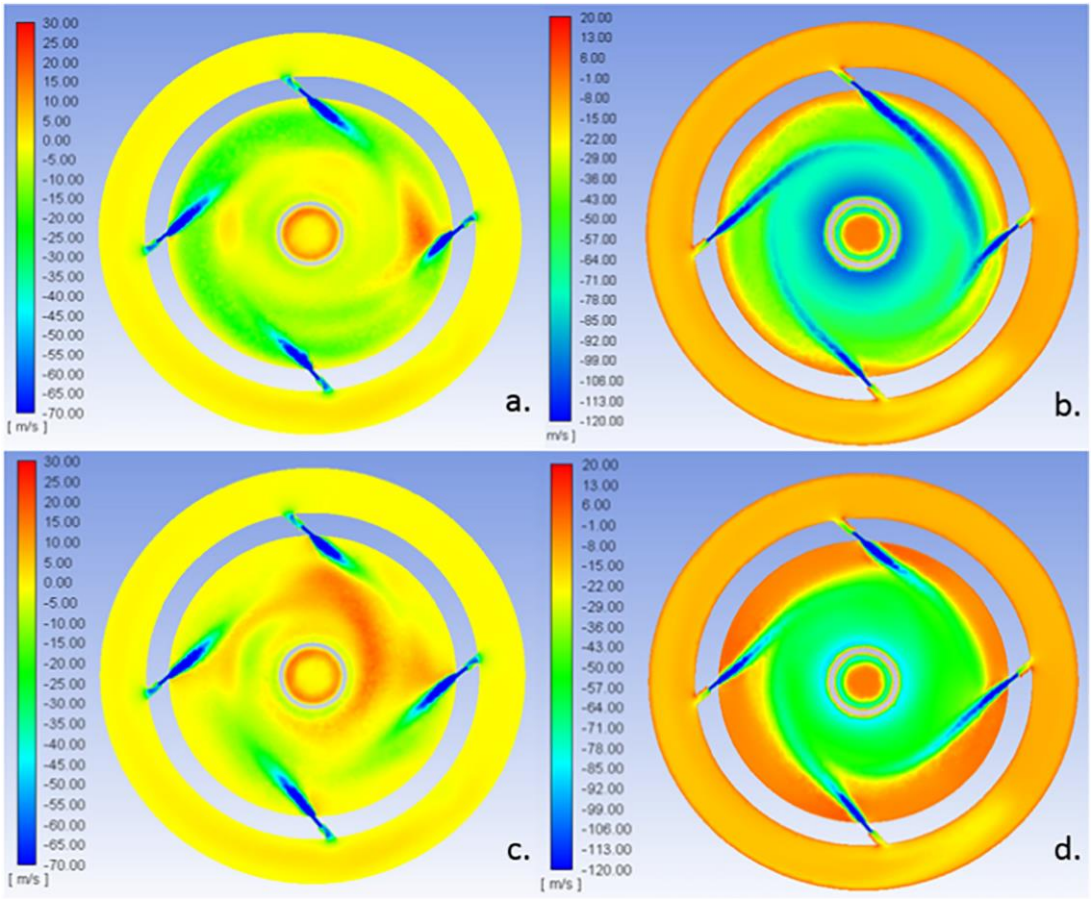

Figure 5-3: The radial and tangential gas velocity components for the 0.4 g mass loading are shown in images (a) and (b), respectively. Images (c) and (d) present the radial and tangential component for the 2.0 g loading case, respectively [24].

Another reason as to why the velocity of the fluid is decreasing, is due to the variation in the fluid turbulent properties as the mass loading changes. Particles should attenuate turbulence present in the fluid field, locally however, the particles can increase the shear rate of the fluid and the production term of turbulence though the creation of wakes [46]. When particles group together in a large cluster, or in a dense bed, they also greatly affect the finite fluid volume cell, leading to a change in thr flow pattern of the fluid. The turbulent kinetic energy (J/kg) for the 0.4 g and 2.0 g cases is shown in Figure 5-4 after 0.06 s in time has elapsed. It can be seen that the mass loading has effected the turbulent kinetic energy term, causing it to increase. This was something that was also noted by Luczak [37], as they saw an increase in the turbulent kinetic energy in the lean phase of the mill during the particle image velocimetry study when mass loading was increased.

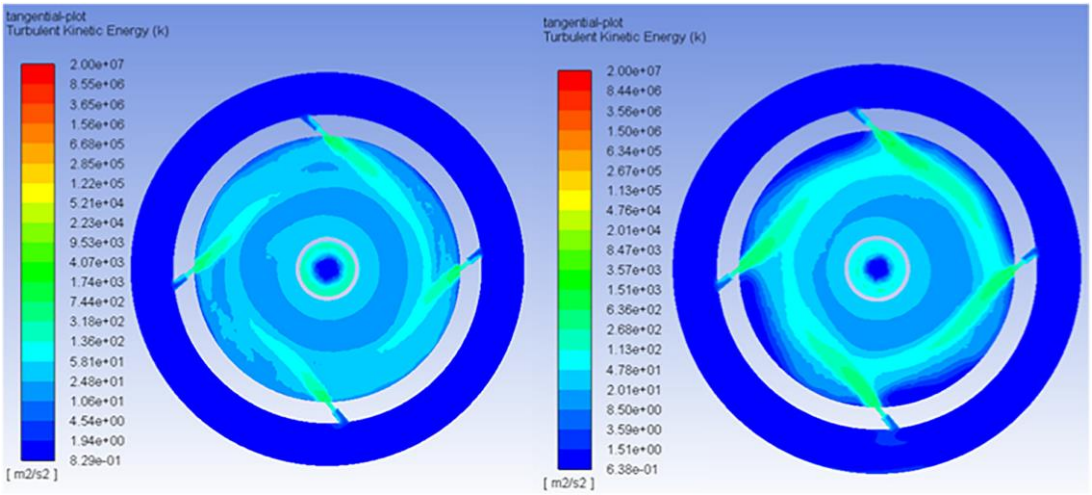

Figure 5-4: Turbulent kinetic energy (J/kg) plot of the fluid field for the 0.4 g and 2.0 g loading cases after t = 0.06 s [4]

5.4. Particle Phase Results

Each of the average particle velocity profiles as a function of radial position is shown in Figure 5-5. Each is constructed using the moving average with an interval window size of 30 measurements. Data points are collected from a slice with a width of eight particle diameters and a length spanning from the out wall to the centre. The data was collected at 45° between nozzles (N1) and (N2), which can be seen in Figure 5-6. The datum from 200 time intervals is used to construct each profile; however, it was necessary to remove data points past 12 mm, as there are too few particles that can travel this far toward the mill centre.

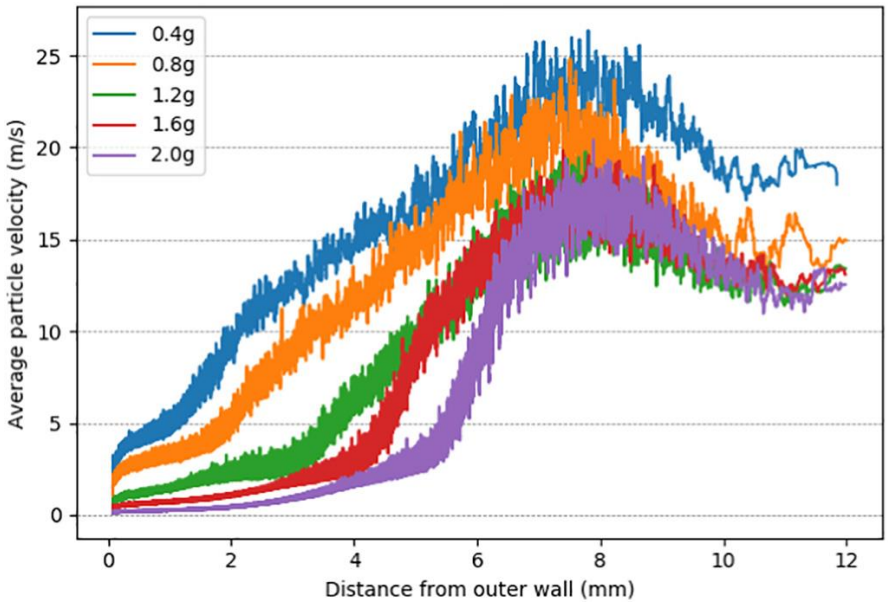

Figure 5-5: Average particle velocity profile for each mass loading as a function of distance from the outer wall of the mill [24].

The 0.4 g case has a highest velocity profile out of the five mass loadings. There are fewer particles to accelerate compared to the other cases and this results in a higher average velocity. As there are fewer particles, the mean free path of a particle also increases resulting in longer period of time to accelerate before a collision takes place. Particles next to the wall travel at around 3 m/s, as there is some damping of the fluid field caused by the bed at this position that limits acceleration. However, the particles increase in velocity moving radially towards the centre until approximately 7.5 mm, at which point the particle velocity begins decreasing. In this case the bed is around 1 mm thick. There is also an amount of shearing present between the layers of bed that is indicated by the velocity gradient. Similar results can be seen for the 0.8 g case to a lesser extent due to larger amount of material present, and once again for the 1.2 g case.

The 1.6 g and 2.0 g case show a different trend to the other three cases. The highest velocity is still around 7.5 mm, however, the velocity gradient in the bed is much shallower. The profiles indicates very little difference in velocity between the shearing layer and display an almost ‘plug-flow’ like behaviour. If this is the case, then size reduction due to abrasion would be diminished.

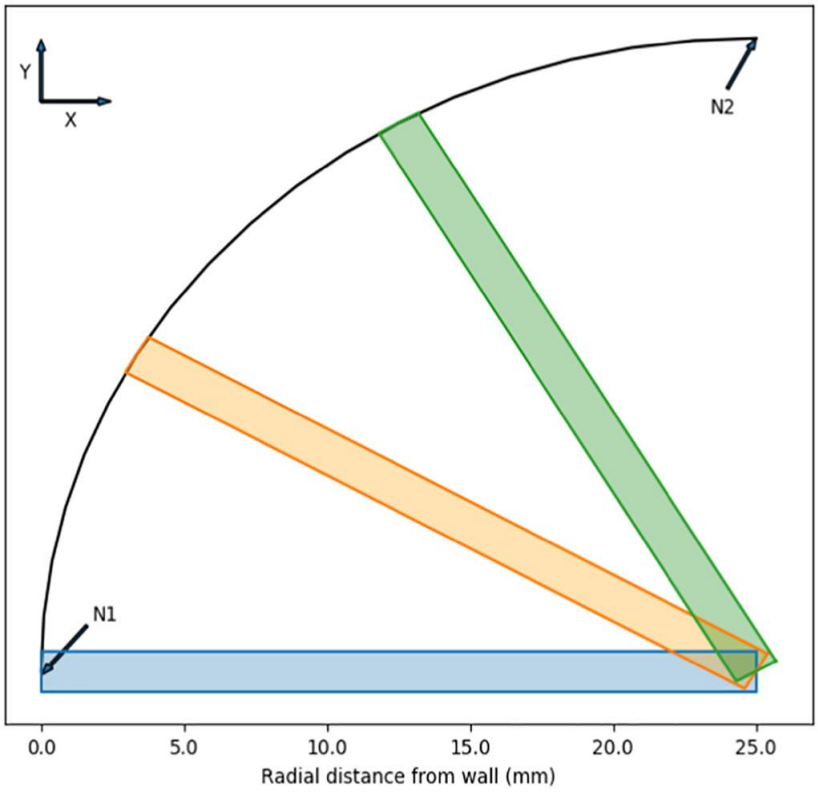

Figure 5-6: Projection of slices used to collect data located at 0° (blue), 30° (orange) and 60° (green) past the nozzle (N1) located at the 9 o'clock position.

Figure 5-7 depicts the average velocity magnitude for each mass loading, but for the entire mill. The velocity is calculated using the radial position of each particle. To highlight key area of interest and avoid ambiguity, the velocity is plotted from 0 – 30 m/s and coloured using the default colour scheme found in Fluent. Dark blue indicates the slowest velocity found in the mill. There is a ring in each image colour dark blue that designates the size and position of the particle bed. Particles travelling at high velocities are denoted in dark red. These can be seen in the jet regions, particularly in image (a). As mass loading increases, the bed develops as seen in images (a) – (e). The bed depth increases and its shapes begins to alter. It becomes shallower after a jet, as material is ejected out of the bed. However, the bed grows once more as particles in the lean region return, and further still, as they begin to impinge on the next jet region.

The behaviour of the particles as they travel in and out of the bed, as well as the velocity of each shearing layer advocates the use of a full four-way coupled CFD-DEM model. Bnà, et al. [40] showed that wall-collisions occur with greater velocity than inter-particle collisions, and exceed 110 m/s. However, the results shown in Figures 5-3 and 5-5 do not agree with their findings. This

study shows that as the bed grows its velocity decreases, and particles closest to wall experience the largest decrease. However, the inconsistency in results is due to a difference in models used. Bnà, et al. [40] used a one-way coupled system, and as a result, the local gas velocity remained unchanged.

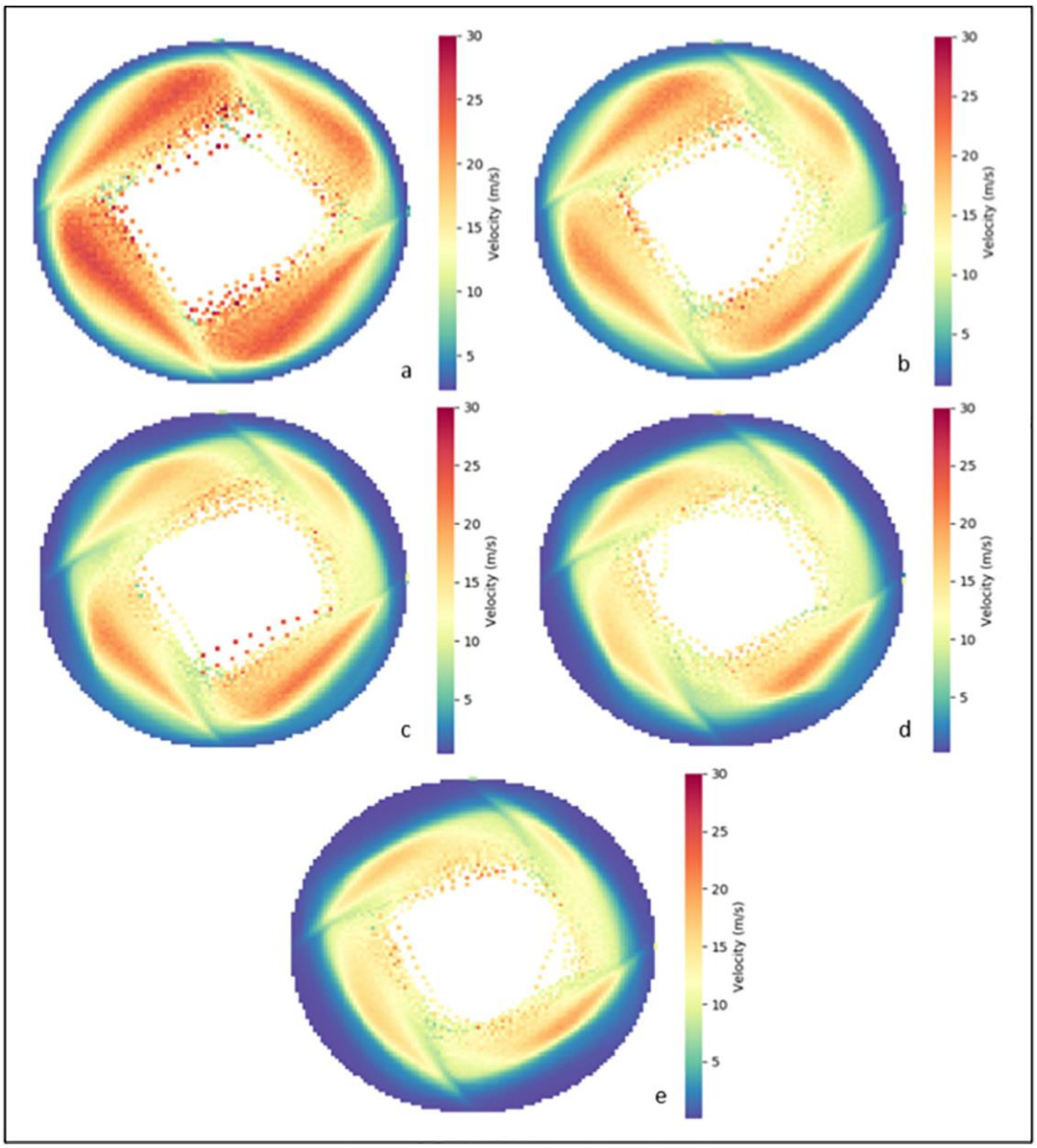

Figure 5-7: Top-down view (z-plane) of particle velocity presented as a contour plot. 0.4 g (a), 0.8 g (b), 1.2 g (c), 1.6 g (d) and 2.0 g (e) cases, respectively.

To depict the evolution of the particle distribution as they travel from jet to jet and how this effects the shape of the bed, data is collected once again from radial slices in between two jets. Three slices are used (Figure 5-6) and capture the velocity of the particles at 0°, 30° and 60°, relative to the jet (N1).

A width of $8d_p$ is used to record the data so that enough particles are captured in each instance. The data is then plotted as a dot, colour-coded by velocity on a 2D plane (r-z) in Figure 5-8. In the 0.4 g case, there is little of significance between images (a), (c) & (e). Material is ejected; however, the shape of the bed appears constant at this lower loading.

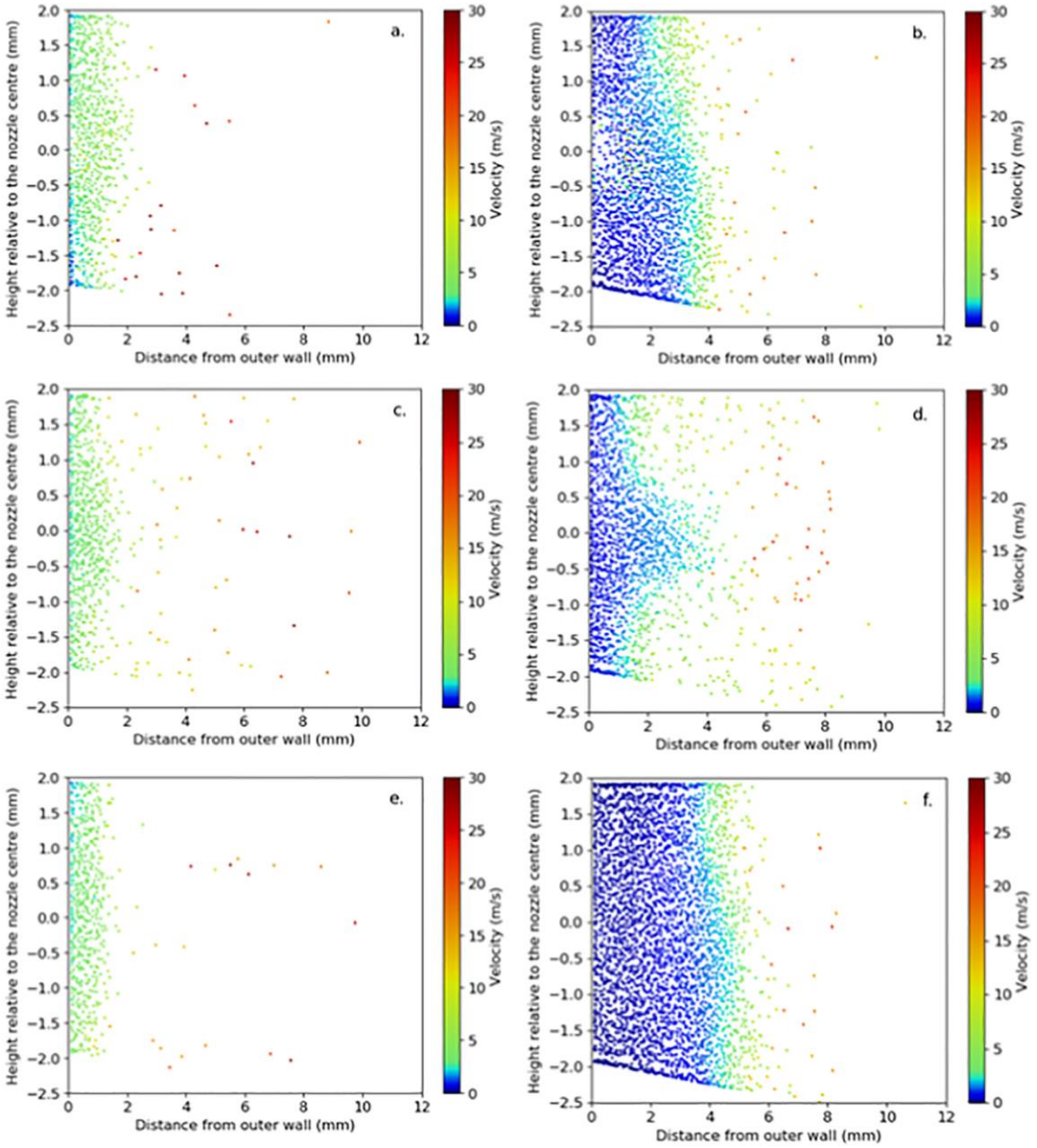

Figure 5-8: Scatter graphs depicting particle position relative to the jet (N1). Images (a), (c) & (e) correspond to a mass loading of 0.4 g at 0°, 30° & 60°, respectively. Images (a), (c) & (e) correspond to a mass loading of 1.6 g at 0°, 30° & 60°, respectively

Instead, the influcnce of the high pressure jets can be seen more clearly in the 1.6 g case. Upon entering the jet region at N1, the particle bed almost

occupies the space uniformly in the z-direction, as can be seen in image (b). However, there is some variation in the bed in three locations. The first is mid-height along the wall, as this correspond to the nozzle position and where air will be ejected at high pressure. The area appears devoid of particles, as they are accelerated out the bed by the jets. The second and third are along the ceiling and base of the mill. Particles in these positions seemed to be more tightly packed together. The angled base of the mill is also clear from this image, and is the reason why the points on the scatter grpahs slope downwards. Image (d) depicts the bed 30° past the nozzle. The surface of the bed is now undulated in shape. The reason for this change in shape, is due a loss of material from the top and bottom of the bed. The material is ejected from the centre and particles move to fill the space created. In doing so, the bump visible in the centre appears, as particles are carried out of the bed. Particle ejected by the jets are easily recognised as they are colour red, and travel with upwards of 20 m/s. As mentioned previously, the particles in this study are too large to leave the simulation. Hence, the momentum of a particle in the tangential direction will force it back towards the bed. It can be seen in image (f) that the bed is at its deepest when compared to images (b) & (d). The velocity gradient in the highest layers of the bed is also clear. This suggests a large of amount of interparticle collisions are taking as the layers shear past one another. The 1.6 g case also depicts the small velocity gradient close to wall, which can also be seen in Figures 10 & 12. Hence, this implies that interparticle collision between particles returning to the bed, and layers of the bed experiencing high shear are repsonible for size reduction in the mill.

The instantaneous total kinetic energy ($E = \sum_{i=1}^{n} M_i v_i^2$) of the particle system is shown in Figure 5-9. The energy of the system is recorded from t = 0.0 s to t = 0.06 s for all five cases. The steep increase in the energy at the beginning of each profile is due to their sudden accleration as they are added into the mill. Upon addition to the mill a particles velocity is initially set to zero. The particle addition rate also creates a environment where fewer particles exist for a period of time. Hence, they are rapidly accelerated and receive a larger proportion of the fluid energy without the presence of bed. The energy profile increases until around 0.01 s. This is when all particles are added, but the bed is still largely uniformed. Therefore particles still receive a large proportional of the available fluid energy. After 0.03 s, the system can be regarded as operating under steady-state conditions, as the bed particle bed has fully formed and fluctations in the particle kinetic energy is at a minimal. Dogbe, et al. [23] also found that 0.03 s was a sufficient amount of time for the system to stabilise, when they carried out similar experiments.

Using the data collected between t = 0.03 s and 0.06 s, it was found that the approximate asymtopic value for the instantaneous velocity is 7 J. This was surpising given the change in mass between in case. However, it remains obvious that the fluid power did not change between cases. Hence, it should be expected that the kinetic energy of the particle system remains constant during increases in the mass loading. There was a noticable increase in the dissipated energy from 4.05 W to 4.65 W, around 15%. This suggests that as mass loading increases, the particle system begins dissipating more energy.

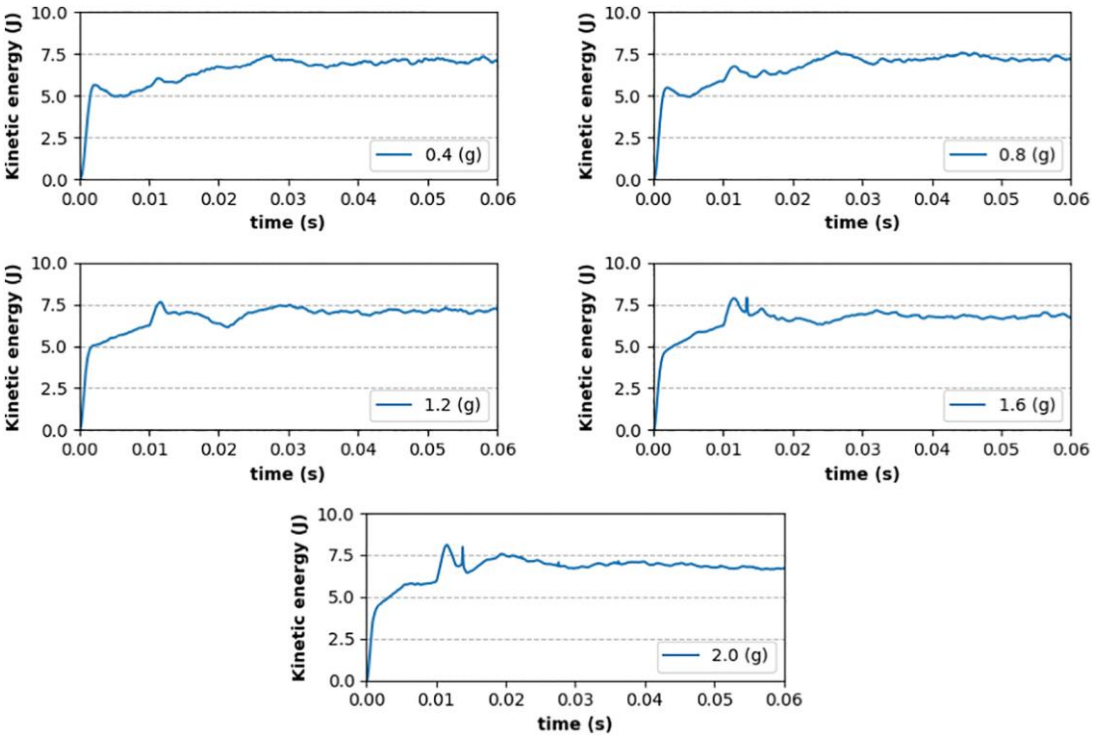

Figure 5-9: Instantaneous total kinetic energy of the particle system from time t = 0.0 s to t = 0.06 s

The spatial distributions of collision energy and frequency is presented in Figure 5-10. Each plot is constructed in the same manner as Figure 5-7 and using all recorded data between t = 0.03 s and t = 0.06 s. Images (i), (ii) & (iii) show the collision frequency for the 0.4 g, 1.2 g and 2.0 g cases, respectively. Where the collisions frequency is at its lowest, the plots appear blue in colour. This then scale through green, yellow, orange to red, where collision frequency is very high. Image (i) shows that collision frequency is highest closest to the wall, and increase slightly before each jet. Due to lack of material, the particle spread out leading to shallow bed. This results in shearing layers passing over one another very close to the wall. Particles also experience some minor pile-up behind the jet regions, as they are forced to

change direction by the high-pressure gas. Particles that travel in the lean region collide infrequently, as they travel with the same velocity and direction, hence this area is largely blue in colour. In image (ii), the thickness of the bed has increased and there is a change in the collision frequency. There is high amount of collision that have been recorded along the bed surface and along the front side of the jets. As discussed previously, the layers of the bed closest to the bed rapid shear and this brings the particles in contact more frequently than deeper layers in the bed. There is also a large number of particles returning to the bed (not visible in the image), which will collide with the bed surface and increases the number of collisions. Particle pile-up is also prominent in this image. Due to jets, the particle build-up and shear along the front-side of the jet due to the sudden change in direction caused by the air. The same behaviour can be seen in image (iii), however, there is now greater divergence in the collision frequency due to thickness of the bed.

The collisions with the largest energy dissipated have been recorded and plotted in images (iv), (v), (vi). The dissipated energy is calculated in EDEM^{TM} 2019 from the change in velocity after a collision has occurred. Again, the colour scheme used is depicted low to high using blue to red. For all mass loading, the largest recorded collision occurs in front of the jets and in a region of high shear. It can be seen when comparing the three cases, the amount of high-energy collisions decreases as the mass loading increases. This can be attributed to the decrease in the average particle velocity, as well as the increase in collision frequency.

The cumulative energy dissipated by particles over 0.03 s is shown in images (vii), (viii) and (ix). In the 0.4 g case, the image (vii) shows that the highest energy is occurring around the jets, due to the high collision frequency and velocity. However, the mill is under-filled at this mass loading, and therefore, this is depiction of energy dissipation is not realistic. Instead, the 1.2 g and 2.0 g cases depict a more accurate representation. It can be seen that there is a high amount of energy dissipated along the bed in a position directly across from the preceding jet, and in front of the nozzles. The combination of high shearing layers and particles returning to the bed is responsible for energy recorded along the layers at the surface. In front of the nozzles, the particles are accelerated and redirected. This leads to particle pile-up behind the jets, and a large amount of shearing to occur. This finding is in agreement with Luczak [37], who showed size reduction is prevalent along the frontside of the jets.

Once the particles enter the lean region, they travel with a similar velocity and direction to one another. Consequentially, the particles collide with a low relative velocity, which decreases energy dissipation. In the deepest layer of the bed, there is also a low rate of energy dissipation. However, this is due to the very high concentration of particles. The particles are always coming into contact, and therefore, inhibit acceleration and result in many low velocities collisions.

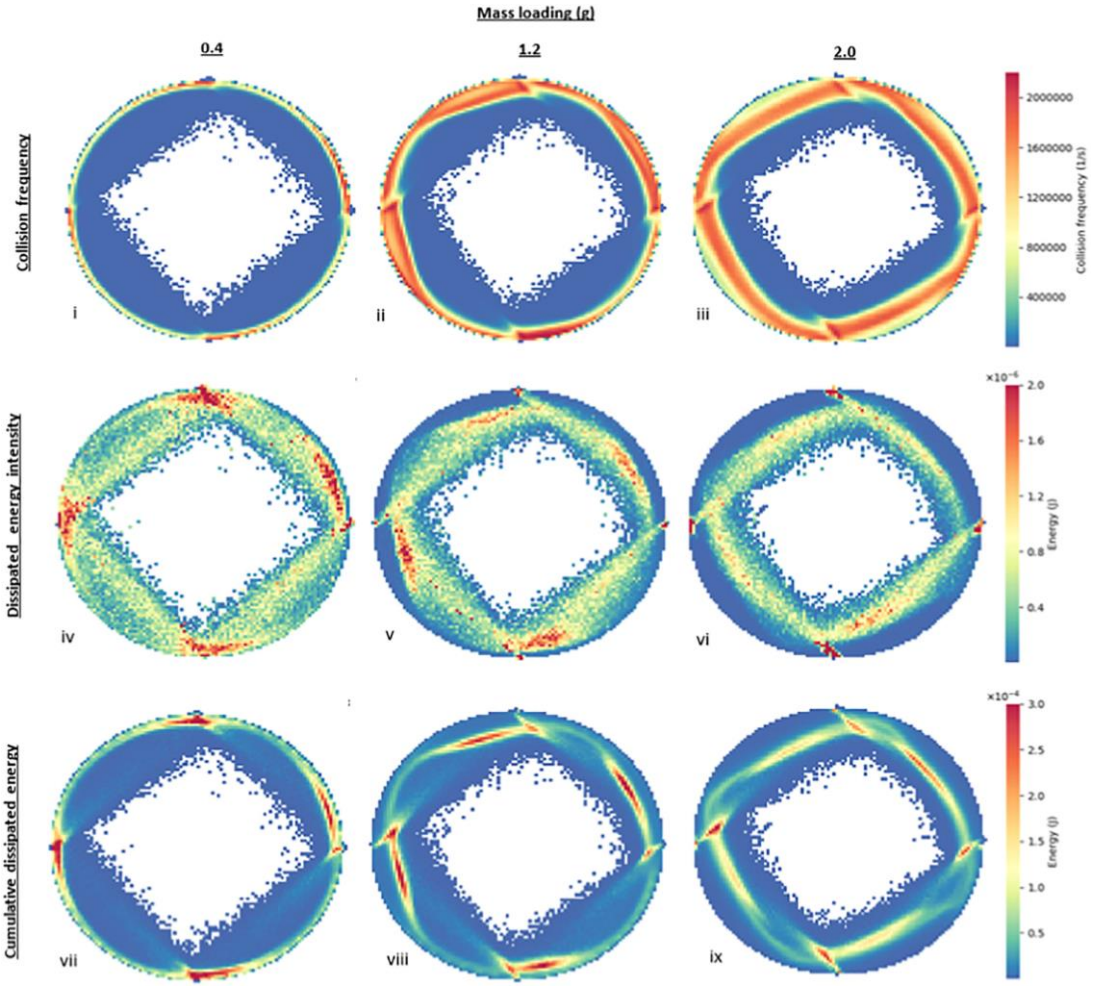

Figure 5-10: Figure 15: Contour plots depicting spatial distribution of collision frequency, energy intensity and energy dissipated for the 0.4 g, 1.2 g, and 2.0 cases. Data present was recorded from t = 0.03 s to 0.06 s

5.5. Conclusions

Particle and fluid motions was analysed as a function of mass loading (hold-up). This was achieved using a four-way coupled CFD-DEM simulation of the Hosokawa Micron AS-50 spiral jet mill. Four solid masses was studied in this work. It is shown that the air velocity surrounding the classifier is indirectly

affected by the hold-up and decreases as the number of particles increases. This is caused by the damping of the air as the jets pass through the bed. It was also shown that as the mass loading is increased, the tangential component of the gas velocity decreases. To compensate, the radial gas component increases to conserve the mass flow rate of gas through the mill. However, since the tangential velocity of the gas dominates the fluid field, this should lead to an increase in the theoretical cut-size.

Increasing the mass loading leads to an overall decrease in the particle velocity and less energetic collisions. However, particle collision frequency increased, and therefore, the total dissipated energy remained almost constant at different mass loadings.

The particle kinetic energy shows little change as mass loading is increased. However, since the fluid energy delivered to the mill does not change throughout the experiment, the particle kinetic energy cannot change.

Finally, the resulting high velocity collisions and frequency at which they occur along the bed surface, creates an environment of increased energy dissipation. The layers of the bed shear across one another at a high rate, whilst particle return at high velocity from the lean region. There is also a high rate of energy dissipation in front of the nozzles. Particle collisions in this region have a higher relative velocity due to sudden change of direction. Particles travelling along the frontside of the jet shear with others also in the jet and with others in the bed.

Chapter 6 Effect of grinding nozzle pressure on particle and fluid dynamics

6.1. Introduction

Increasing the grinding gas pressure, leads to a finer particle product size [21]. This is due to a larger amount of surplus fluid energy that is available and transferred to the particles. The energy transferred increases the average velocity of particles, and in turn, leads to higher energy collisions. The increase in grinding pressure is not linearly proportional to the increase in pressure [30,35]. Surface flaws in the material leads to the initial size reduction. However, due to size reduction in the mill, the particles begin to carry less momentum into further collisions; hence, reducing the rate of size reduction [47].

Using coupled CFD-DEM, Brosh, et al. [43] investigated the effect of reducing the pressure of the grinding gas on the particle product size. Along with an increase in the particle size leaving the mill, they also showed that the particle size distribution leaving the mill widened. During physical experiments, Müller, et al. [4] found that when the grinding gas pressure was sufficiently low, the vortex became unstable and this led to poor classification. For their mill, they considered 8 barg to an acceptable grinding gas pressure. However, using piezoelectric pressure sensors, they could produce images of the mill operating at lower grinding pressures. They noted that at 4 barg, the vortex inside their mill became unstable and this led to poor classification and a widening of the particle size distribution leaving the mill. Both Rodnianski, et al [29] and Bnà et al. [40] analysed the fluid dynamics in the mill, as a function of pressure. They showed that the gas velocity components $\left(\frac{V_t^2}{v_r^2}\right)$ remained constant, as the grinding gas pressure was increaased. However, in both studies, neither group used a fully coupled CFD-DEM approach. Rodnianski, et al [29], preformed their analyse on a CFD only simulation and Bnà et al. [40] only used one-way coulpled CFD-DEM. Since the effect of the particle bed has been shown to influnce the fluid flow field [24], it is unlikely that they were able to capture the behaviour of the fluid due to particle damping.

The pressure of the grinding gas determines both the stability of the vortex and finesse of the particles exiting the mill. In this investigation a range of grinding pressures is investigated using a four-way coupled CFD-DEM approach [14,48,49]. By varying the gas pressure and mass loading (hold-up), the fluid flow field, particle velocity and particle collision behaviour can be

analysed. As the focus of this study is effected of the grinding pressure of the fluid flield and particle dynamics, particle breakage has not been included. Hence, there is no size reduction mechanic in this simulation.

6.2. Methodology

The mill used in this study is based on the Hosokawa Micron AS-50 spiral jet mill. An in-house drawing of the mill can be seen in Chapter 5, Figure 5-1. Five grinding gas pressures are investigated (2, 3, 4, 5 & 6 barg). This was done in combination with six different particle mass loading (0.4, 0.8, 1.2, 1.6, 2.0 & 2.4 g). The gas pressure and mass combinations can be read in Table 6-1, along with the particle number associated with a particular simulation. A base particle size of 100 µm, with a random distribution of (0.8-1.2)*r*; where *r* is the particle radius. This is the reason for the slight variation in particle number. The feed gas pressure is simulated one bar higher than the grinding gas pressure. All the particles were added with a velocity of 0 m/s and before 0.01 s using the standard EDEM™ factory. This means that the addition rate of particles is varied for each mass loading to ensure the particle are added within the time allowed. Its has been found that 0.02 s from loading ends is typically enough time for the particle bed to develop. However, for any time-sensitive data, no results are collected before 0.07 s. The simulations are ended at 0.1 s.

Table 6-1: Gas pressures, mass loadings and particle numbers

Grinding Gas Nozzles Pressure (barg)	2	3	4	5	6
Mass Loading(g)	**Particle number**				
0.4	61857	61869	61701	61884	61822
0.8	123684	123481	123467	123404	123535
1.2	184576	184958	184796	184763	184596
1.6	246368	246025	246248	245892	245779
2.0	310191	308539	307964	307393	307675
2.4	383380	373565	371522	371471	370853

The particle motion is calculated using EDEM™ 2019 (Altair, UK) and the fluid flow field is resolved using ANSYS Fluent 18.1. A four-way coupled CFD-DEM scheme is used to capture all fluid-particle and interparticle interactions. The *k*-*ε*-RNG turbulence model with scalable wall functions and the ‘SIMPLE’

pressure-velocity coupling is used during the fluid time-step discretisation, along with the spherical drag law developed by Morsi and Alexander [44]. The density of the air is calculated by the ideal gas law. The mesh size used in the simulations is based on the largest particle size (240 µm), with a maximum particle-fluid volume ratio of 40%; this is the recommended by Norouzi, et al. [16]. The particle parameters such as the coefficient of restitution and friction, as well as the fluid parameters are listed in Table 6-2. The particle time step is varied due to the particle number, but is not allowed to exceed 25% the Rayleigh's time step. A ratio of 20 particle time steps to 1 fluid time step has been selected, once again, recommended Norouzi, et al [16]. The values used for both the fluid and particle time-steps are also presented in Table 6-2.

Table 6-2: Fluid and particle parameters and properties

Phase	Parameter	Value
Fluid	Viscosity, µPa/s	0.018
	Fluid time step, µs	$8 - 20$
	Minimum edge length (particles present), µm	630
	Minimum edge length (no particles present), µm	400
	Equation of state	Ideal gas law
Particle	Radius (µm)	100
	Density, kg/m^3	1500
	Size distribution	0.8-r-1.2
	Shear modulus, MPa	10
	Poisson's ratio	0.25
	Coefficient of restitution	0.5
	Coefficient of static friction	0.5
	Coefficient of rolling friction	0.01
	DEM time step, µs	$0.4 - 1.0$

6.3. Results

Each particle velocity magnitude as a function of radial distance is shown in Figure 6-1 for each mass loading and grinding gas pressure. The data for each profile are collected from an $8d_p$ in width slice of the bed. The slice is positioned at an equal distance between two nozzles, as shown in Figure 6-2. Data was not collected until 0.07 s of the simulation had elapsed; this allowed the particle bed to reach a pseudo steady state. A total of 300 time steps of data are then collected. Particles were only recorded up to a radial distance of 12 mm, as too few particles travel radially past this point at this

size. The moving average with a maximum of 30 data points is used when creating each profile.

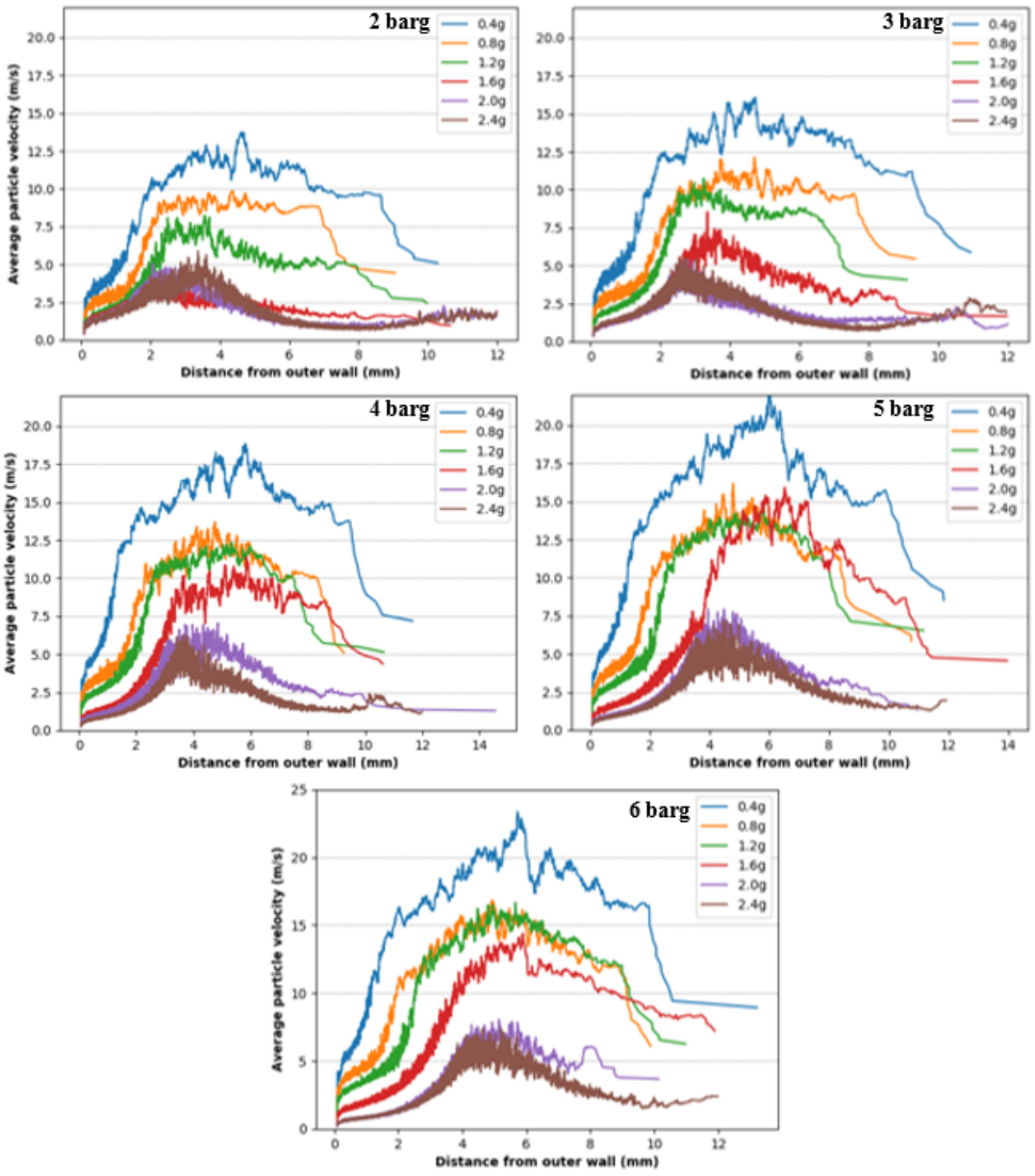

Figure 6-1: Profile of particle velocity magnitude as a function of distance from the outer wall, for each combination of mass loading and grinding gas pressure [50].

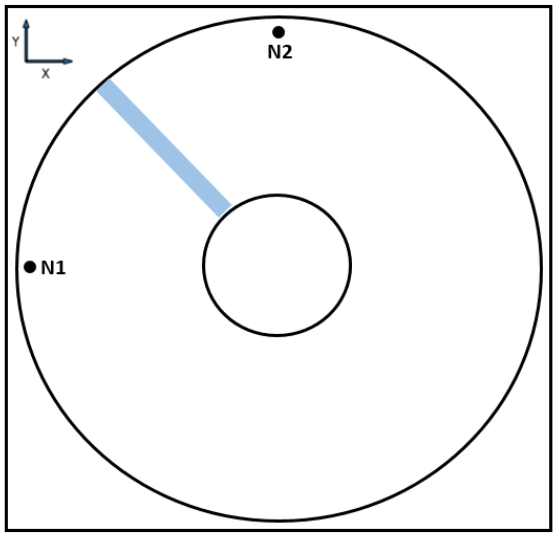

Figure 6-2: Schematic of slice position used to collect particle velocity data (shown in blue). Placed at an equal distance from two nozzles N1 and N2.

As would be expected, the lowest particle velocity distribution for all pressures investigated was recorded when the grinding pressure was set to 2 barg. The highest velocity distribution for the 2 barg pressure is recorded in the lowest loading case (0.4 g). The decreases the mass loading results in the highest velocity due to the increased time in between collisions. A maximum of 13 m/s was recorded. As the mass loading is increased, the particle velocity distribution decreases each time. It can also be seen that velocity gradient of the bed decreases as the mass loading increases. This decrease in velocity causes the bed to behaviour with near 'plug-like' flow next to outer wall at the highest mass loading. In each case, the beds never achieve plug flow, as the particle layers always shear past one another at different velocities. Beyond the 10 mm range on each profile, the particles enter the lean phase and the data become unreliable due to the low number of particles that exist in this region.

Increasing the grinding gas pressure to 3 barg results in an increase in the particle velocity magnitude. The same trend between the profiles match that of the 2 barg case. The 0.4 g case depicts the highest recorded velocity out of all cases, whilst the 2.0 g and 2.4 g overlap with the slowest velocity recorded. As the mass loading increases, the low velocity region extends further towards the centre. This indicated the bed is growing, as would be expected. In all cases, there is rapid shearing at the surface of the bed.

The particle velocity distributions in the 4, 5 & 6 barg cases all produce similar profiles to that seen in the 3 barg. Incrementally increasing the grinding gas pressure, increases the overall particle velocity at a given radial position in the milling chamber. However, it can also be seen that the velocities distributions notably shift towards the right, as grinding gas pressure is increased. This indicates a change in the bed dynamics, as the low particle velocity gradient found in the bed extends further towards the centre of the mill. This would also suggest that there is a lack of shear straining in the particle bed and would limit size reduction from occurring there. Since the particle velocity profiles for the 2.0 & 2.4 g cases align so closely near to the outer wall, this suggests that the bed is 'fully saturated' in terms of particle arrangement and mass loading.

The fluid velocity gradient as a 'heat-map' is shown in Figure 6-3. The plots depict fluid flow field along the mid-plane for each pressure and 1.2 g mass loading. In each image, the velocity has been clipped to 120 m/s, as this ensures each region and their boundaries are highlighted. As expected, it can be seen that as the grinding gas pressure is increased, so too does the fluid velocity. However, it can also be seen that when the grinding gas pressure is increase, there is little change in the fluid velocity in the region occupied by the bed. This is because the jets more efficiently penetrate through the bed at higher pressures and eject their fluid energy into the lean region. Whereas, at the lower pressures (2 & 3 barg), the jets dissipate before appearing to breach the bed surface. Hence, it appears that little fluid energy is directly transferred to the bed region for any of the pressures used.

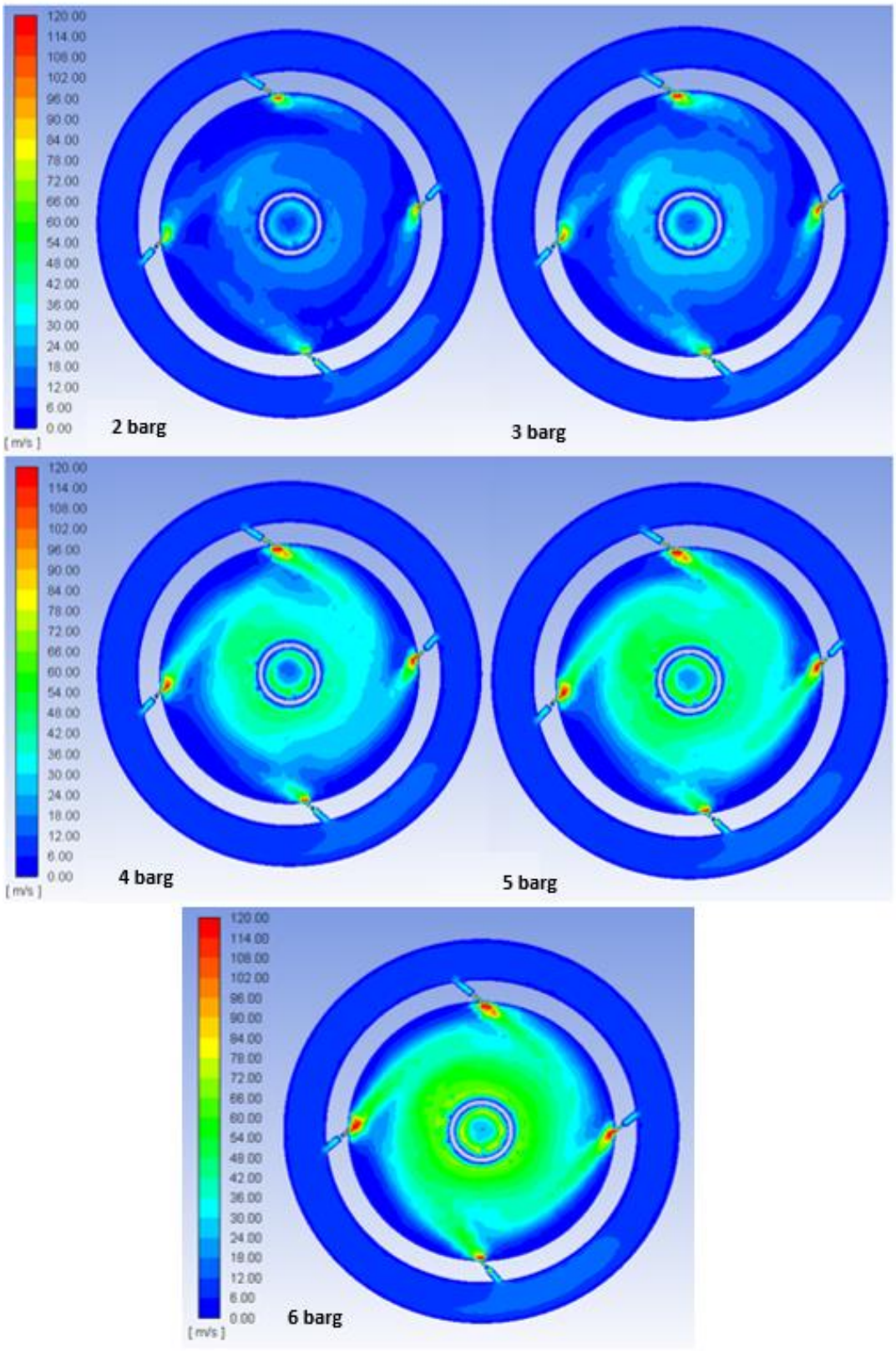

Figure 6-3: Heat map of air velocity (m/s) for each grinding gas pressure used at 1.2 g sold mass loading.

Once the jet region penetrate through the bed, a forced vortex prevails before a free-vortex is created due to the proximity of the high velocity gas next to the classifier ring. The pressure field is depicted in Figure 6-4 for the 5 barg case with 1.2 g of solid material forming the particle bed. The pressure field has been clipped to 10000 Pa, to highlight the all areas of the mill and there boundaries once again. As can be seen, this limit is necessary as the range of interest is very tight over milling chamber and could not be viewed if the entire range from 0-5 barg is used. In the left image of figure 19, the z-plane along the mid-height of the mill can be viewed. In the right image, the z-plane is used to show the mid-plane between two opposing jets. It can be seen, that inside the mill, there is little change in the pressure gradient from the wall to the classifier ring. After passing through the nozzles the gas rapidly expands and results in a pressure of around 7 kPa above atmospheric pressure. At higher pressures (4 barg and above) the jets penetrate through the bed, and therefore, there is limited opportunity to exchange energy with the particle bed directly. It can be seen in Figure 6-4, that there is a another pressure drop, which occurs in the classifier section. The air is accelerated through the constriction, created by the classifier ring. However, the pressure drop is not recovered as the volume increases once again. The air then travels downwards and out of the mill, exiting to atmospheric pressure.

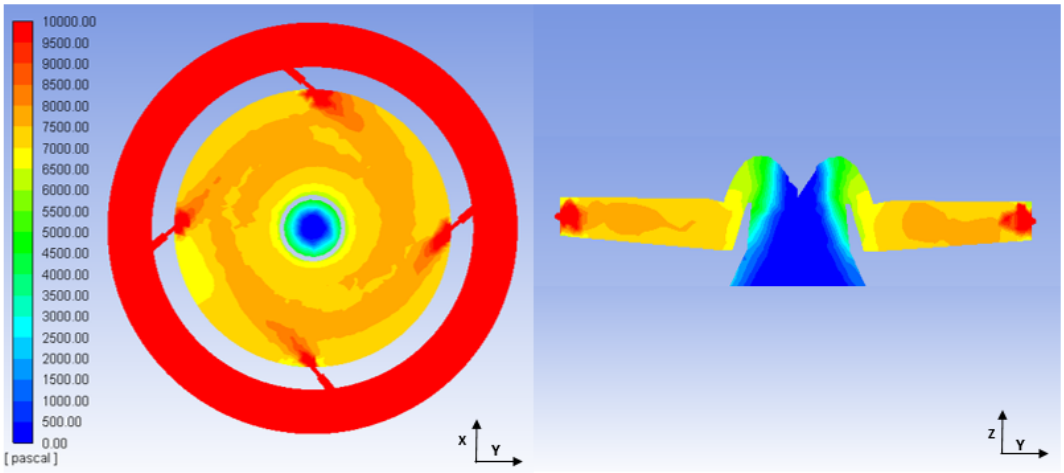

Figure 6-4: Mid-plane (left) and x-plane view (right) of the pressure field for the 5 barg case with 1.2 g of solid material present.

To understand how each particle system is affected by the incremental increase in the grinding gas pressure, the total instantaneous kinetic energy of the particle system is shown in Figure 6-5. Each plot depicts how the kinetic

energy of the particle system evolves for every combination of mass loading and grinding gas pressure, from time t = 0.0 s till t = 0.1 s. At the beginning of each profile, there is sharp increase in the total kinetic energy, until around 0.01 s. This is because the particles are added to the mill with their velocity set to 0 m/s. After the rapid acceleration, there is a noticeable peak in each profile just after 0.01 s. The increased kinetic energy occurs due to random placement of particles by the EDEM^{TM} factory and the undampened fluid field. At the start of each simulation, the particle bed is unformed, so the fluid field receives lower amounts of localised damping. Hence, as the simulation progresses and particle bed is formed, the area occupied by the particle bed heavily dampens the fluid field and reduces the total kinetic energy available.

Looking at the 2 barg case, it can be seen that there is some initial variation between the different mass loadings. However, as the simulations continue, each profile reaches the same asymptotic value before the experiment ends at 0.1 s. The same trend is also roughly true for the 3 barg case and each of the mass loadings. This finding is unexpected for the lower pressures, as it suggests that regardless of mass loading, the kinetic energy of the particle system reaches the same asymptotic value. However, it can be understood by re-examining the jets in Figure 18. For the 2 & 3 barg cases, the jets appear to be unable to penetrate through the bed. Hence, the jets remain submerged and more energy that is available is directly transferred to the particle bed before the air enters the lean phase. In contrast, the 4, 5 & 6 barg cases show some disparity between the total kinetic energy of the particle systems. However, the total kinetic energy of the particle system does not simply decrease with mass loading; instead, it varies depending on the behaviour of the jets. When the mass loading is low, the jets penetrate through the bed. This limits the exchange of fluid energy to the particle bed, as only a fraction of particles will be within jet boundaries. Consequentially, this behaviour culminates at the mass loading 1.6 g where the lowest kinetic energy profile was recorded for the 4, 5 & 6 barg cases. After which, increasing the mass further results in jets inability to directly penetrate through the particle bed. More fluid energy is once again transferred to the particle bed, before the air enters the lean phase. Hence, the total kinetic incrementally increases for the 2.0 & 2.4 g cases. Nevertheless, the kinetic energy of the 1.2 g particle system increases proportionally from 5 mJ to 14 mJ, as the grinding gas pressure is increased from 2 – 6 barg. However, it is relative velocity of a collision that is responsible for size reduction, rather than the kinetic energy of the particle system. Hence, the change in jet penetration depth will have an overall effect on the energy utilised for breakage. The submergence of the gas jet regions

also advocates why there is a large decrease in the velocity gradient when the mass loading is too high. When the jets cannot breach the surface of bed, no particles are able reach the highest velocity found in the lean phase.

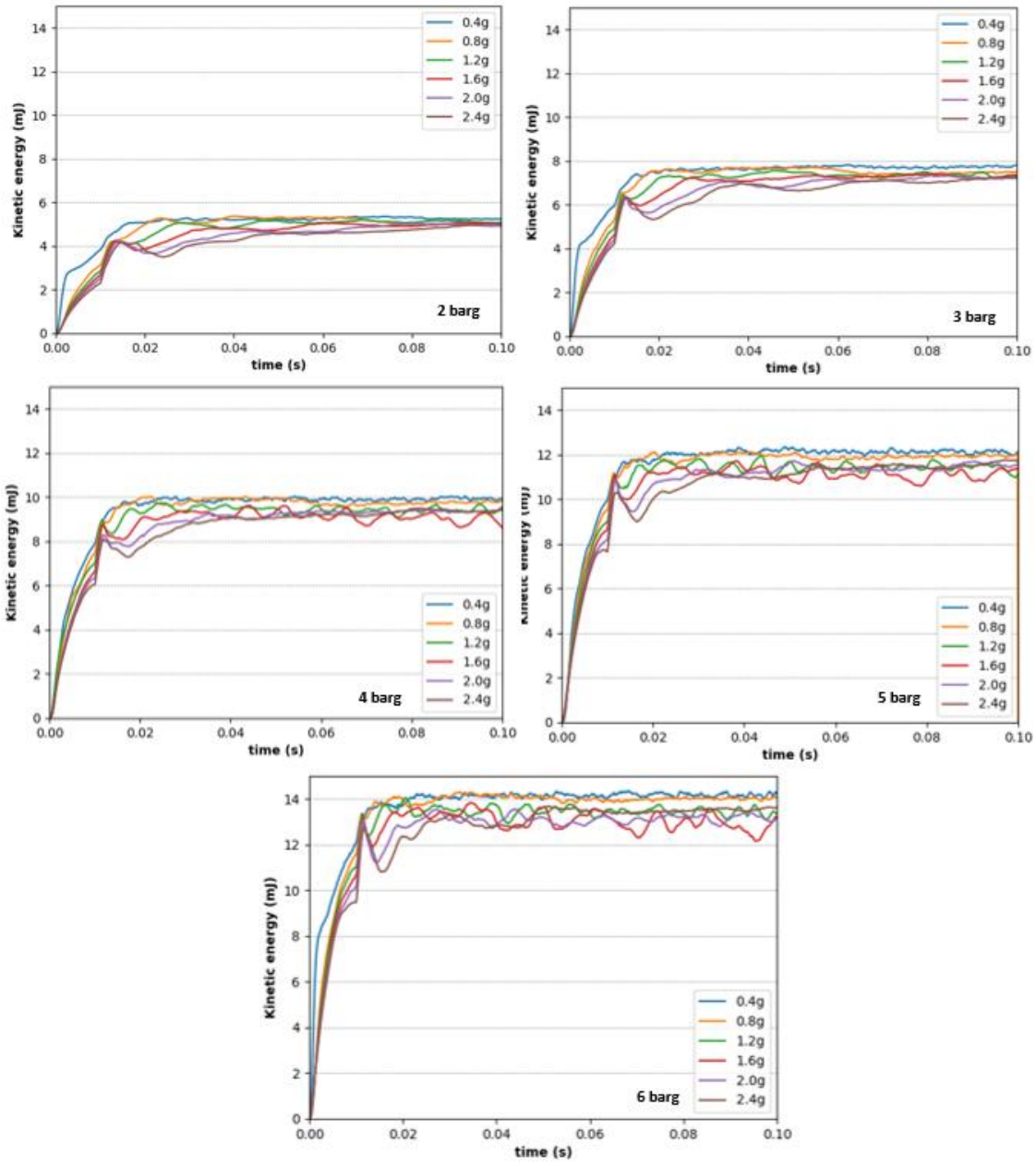

Figure 6-5: Kinetic energy profile for each particle mass loading and grinding gas pressure combination [5].

The dissipated energy from all collisions recorded between 0.07 – 0.1 s, for the 1.2 g mass loading at all five pressures is shown in Figure 6-6. The dissipated energy is found as by calculating the difference in kinetic energy of a particle before and after a collision has taken place. As expected, as the

pressure is increased, so too does the dissipated energy recorded for the entire particle system. However, it is interesting that the increase from 5 to 6 barg is much smaller, than the otherwise proportional increase for the other lower pressures. This finding is in line with analysis of Ramanujam and Venkateswarlu [18] and Kürten & Rumpf [35], who both found that increasing the grinding gas pressure does not lead to a proportional decrease in the product. Instead, the particle system under-utilises the energy available in the fluid.

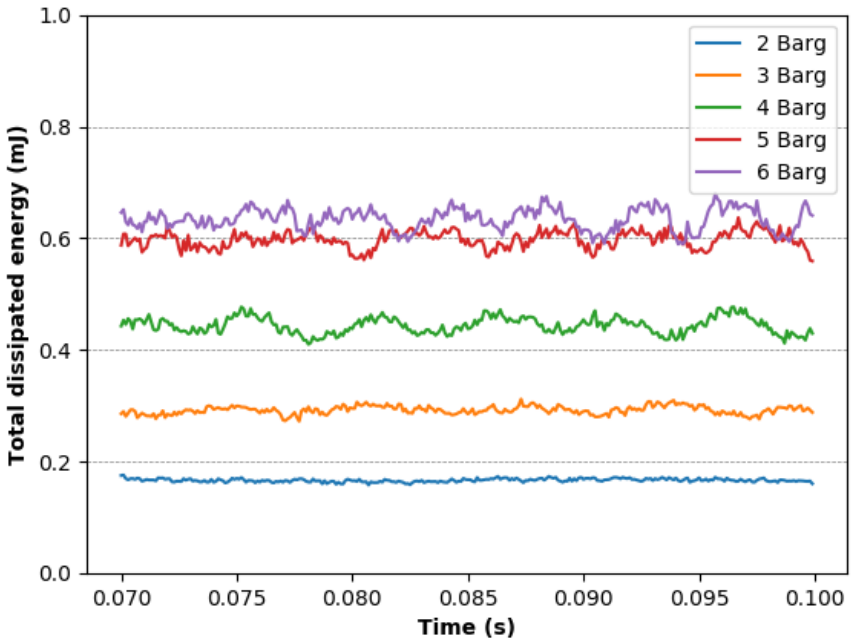

Figure 6-6: Total instantaneous energy dissipated through particles collisions from time 0.07 s to 0.1 s for the 1.2 g mass loading [50]

The spatial maps of dissipated energy recorded can be seen in Figure 6-7. Each image depicts the cumulative dissipated energy recorded over the final 0.03 s of each simulations. It can be seen in each image that a square boundary exists, rather than an expected circular one. This is because the high-pressure jets transport the particles from nozzle to nozzle, and no particle has the required size to make it to the centre. Hence, this creates the square shape that can be seen. Due to the feed pipe, the dark blue lean section is also not symmetrical. The high velocity feed air diverts the milling chamber fluid flow field where it enters.

Although the pressure is increased from 2 – 6 barg, there is no noticeable change in colour in some areas of the particle bed closest to the wall. This

shows that the dissipated energy through collisions is largely unchanged, and advocates the idea that mechanical energy exchange with the particle becomes more limited, as the grinding gas pressure is increased. When particles come into direct contact with the high-pressure gas, there is increased energy transfer, which subsequently leads to high-energy dissipation rates. However, areas of the bed close to wall, do not receive an increase in energy as the gas pressure is increased, as the jets bypass the bed once they are able to penetrate the surface.

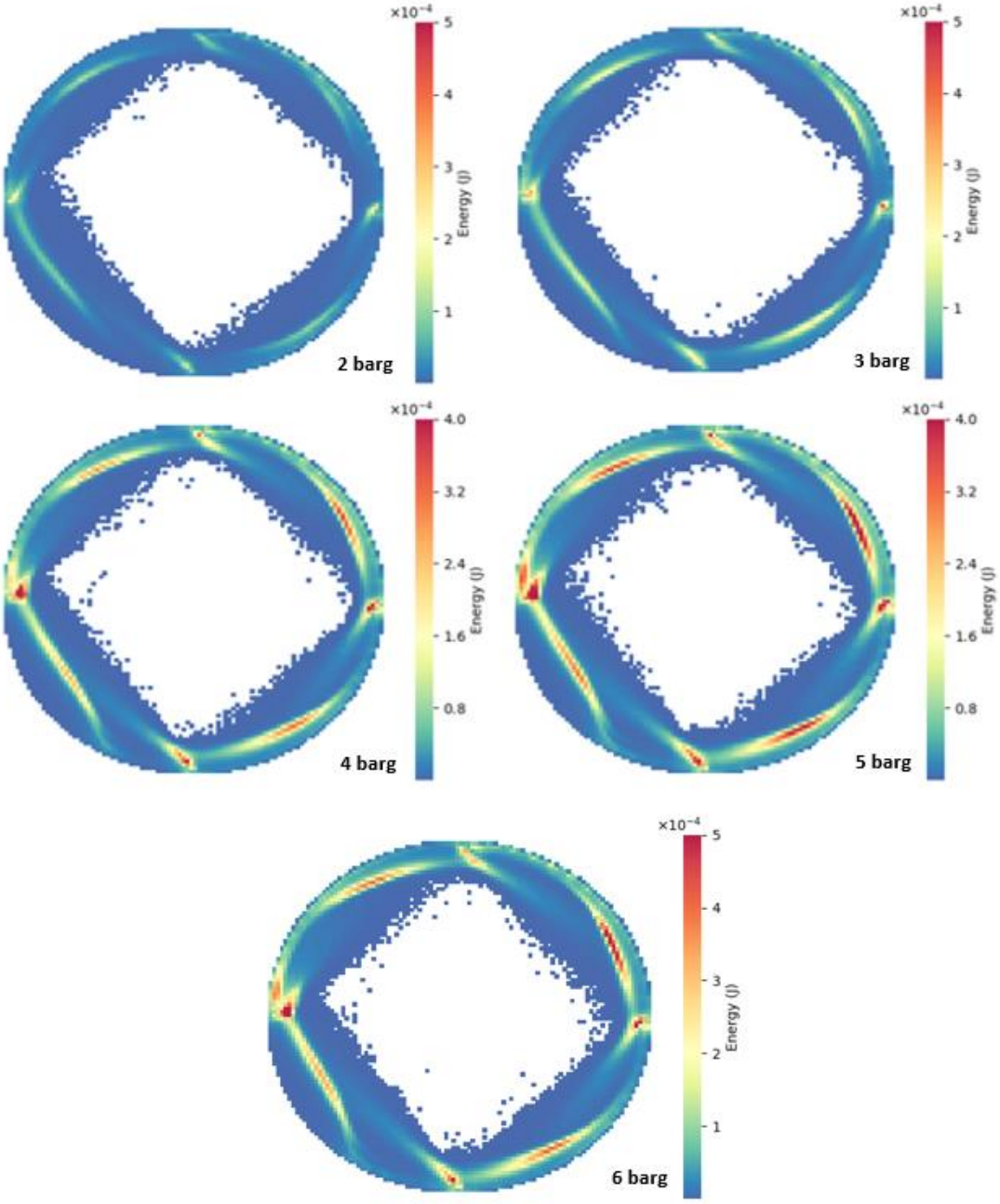

Figure 6-7: Heats maps of cumulative dissipated energy recorded over 0.03 s for the 1.2 g mass loading at each grinding gas pressure [5].

The final section of work relates the system kinetic energy and energy dissipated through particle collisions, with the grinding gas fluid power (*W*). A theoretical value of fluid power can be calculated from the pressure drop and mass flux across a nozzle, as described by Green and Southard [51]:

$$G = P_o \sqrt{\frac{\gamma M_w}{RT_o}} \frac{M_1}{(1+\frac{\gamma-1}{2}M_1^2)^{(\gamma+1)/2(\gamma-1)}} \quad [29]$$

where G is the mass flux, P_o is the upstream gas pressure and T_o is the upstream gas temperature. R is the gas constant, M_w is the molecular weight of the gas, M_1 is the Mach number and γ is the ratio of specific heat capacities at constant pressure and constant temperature. In Figure 6-8, it can be seen that as the mass loading increases, the kinetic energy of the system decreases. This is until the trend reverses for 2.0 g. The lowest kinetic energy is consistently recorded for the 1.6 g case at fluid powers higher than 600 W. This is because the jets can breach the surface of the bed and less mechanical energy transfer takes place with the particles. Once again, the jets can longer penetrate the surface of the bed in the 2.0 g and 2.4g, and so more energy is directly transferred to the particles before the air enters the lean region.

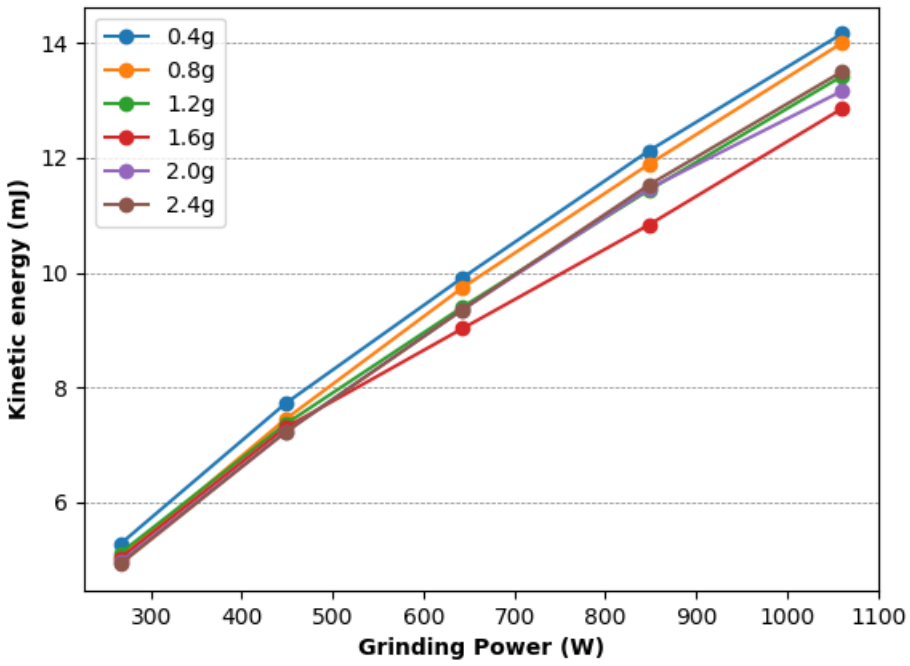

Figure 6-8: Average particle system kinetic energy as a function of theoretical fluid power for each mass loading [5].

Figure 6-9 depicts the dissipated energy of the particle system recorded over 0.03 s for the 1.2 g and 2.4 g cases, as a function of the theoretical fluid power. These two cases were chosen, as it is shown in Figure 23 that these particle systems have the same kinetic energy at all calculated fluid powers. However, the 1.2 g case consistently manages to transfer more energy through collisions than the 2.4 g case. This highlights the change in particle dynamics once the jets become submerged, as the fluid power is less efficiently

transferred to the particles. The sudden change in trend in the 1.2 g case, is related to the point at which the jets penetrating through the bed and leave the mill without the energy being fully utilised.

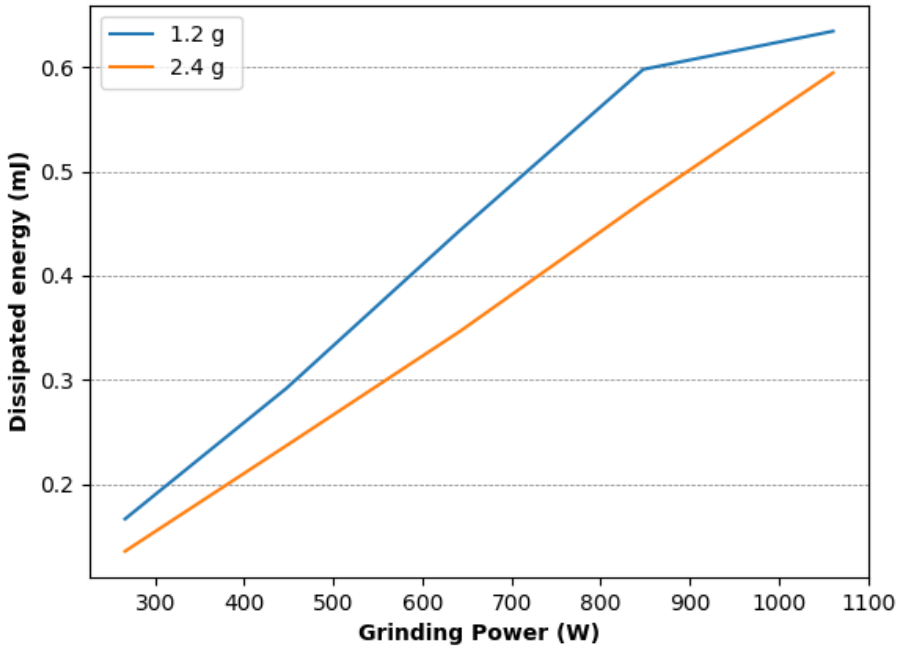

Figure 6-9: Average particle dissipated energy that is lost through particle collisions as a function of fluid power supplied [5].

6.4. Conclusions

Using a four-way coupled CFD-DEM simulation, the effect of grinding pressure was analysed in the spiral jet mill (Hosokawa Micron AS-50). In total five grinding pressures (2, 3, 4, 5 & 6 barg) were investigated at six different mass loadings (0.4, 0.8, 1.2, 1.6, 2.0 & 2.4 g). The results show that as the grinding gas pressure is increased, the average particle velocity also increases. However, for the largest mass loading (1.6, 2.0 & 2.4 g), the velocity gradient within the bed decreases and the particle closest to wall seem unaffected by the increase in pressure.

Once the jets become submerged, there is a large decrease in the particle velocity. Particles in the jet region are no longer accelerated into the lean region, and therefore, are not exposed to the high velocity are associated there.

Finally, the kinetic energy of the particle system increases proportional as the pressure is increased from 2 to 6 barg. However, the dissipated energy lost through particle collisions and accountable for size reduction is highly dependent on the jet behaviour and its ability to penetrate through the surface of the bed. If the high velocity jets can penetrate through the bed, then the particles are exposed to higher shear rate and accelerated into the lean phase. Therefore, this promotes size reduction in the mill. However, once the jets become submerged in the bed region, fluid power is more effectively transferred to the bed, but particles do not reach the higher velocities, as they are no longer ejected into the lean phase. This leads to preservation of kinetic at higher mass loadings, but a decrease in particle dissipation energy.

Chapter 7 Application of the Coarse Grain method in a spiral jet mill

7.1. Introduction

The main issue of using coupled CFD-DEM to simulate a spiral jet mill is the limitation particle size and number imposes due to computational memory (hardware) available. The total number of particles that can be simulated limits how large a mill can be, whereas the size of the particle directly effects the time step used during each calculation. Hence, it is unrealistic to simulate large spiral jet mills, which produce a product size between 5-20 µm without some form of scaling solution being used. Teng *et al.* [41] were able to analyse the interparticle collisions, which indicated a main cause of size reduction was due to a shearing action of particles. Dogbe [25] analysed the combination of particle sizes that were responsible for size reduction. However, both investigations were limited by particle number and size. As a result, neither saw particles allowed to exit the mill. Brosh *et al.* [43] did simulate breakage using an in-house code. However, they manually removed fines directly from the simulation. They mention the impracticability of simulating the fines with the hardware available to them.

Furthermore, it is not practical to use anything other than a fully coupled system. Rodnianski *et al.* [29] determined the particle classification size through the velocity ratio of the tangential and radial components. However, they concluded CFD is not sufficient on its own, as the particle weighting on the fluid field is not captured. Bnà *et al*. [40] used a one-way coupled system so that the fluid transferred momentum to the particles, and their results agree well with the cut-size equation proposed by Dobson and Rothwell [33]:

$$\delta_{cut} = \frac{3}{4}\frac{c_d \rho_g r_c}{\rho_p}\left(\frac{(\boldsymbol{v}_{r,g})^2}{(\boldsymbol{v}_{t,g})^2}\right) \quad [30]$$

However, the authors suggest that their simulation is only acceptable for predicting the product size if the mill was operated as a classifier, not under normal operation.

Bnà *et al*. [40] also discuss the use of scaling to increase the size of the simulation. They approach scaling by manipulating the particle density to inflate the particle size:

$$d_{p,fake} = \frac{d_p \cdot \rho_p}{\rho_{p,fake}} \quad [31]$$

where d_p and $d_{p,fake}$ are the original and scaled particle diameters, and ρ_p and $\rho_{p,fake}$ are the particle density and scaled particle density, respectively. They concluded that this method of scaling was suitable for predicting the translation component of particle motion, yet was unable to predict the rotation component after the particles had been scaled.

The Coarse Grain (CG) method is a non-exact scaling solution for predicting the bulk behaviour of a large particle assemblage. Unlike methods that scale each individual particle, i.e. density scaling used by Bnà *et al*. [40], a group of particles are replaced by a single larger particle of the same envelop density. The CG method is based on the assumption that the number of particles used will statistically represent the group of particles it replaces without altering the bulk mechaincs of the particle system, or fluid field if CFD is combined in the simulation. Hence, any external forces, such as fluid drag, are also scaled to maintain all forces that would act on the original particles [32,52]. The CG method has also been used successfully to model a number of CFD-DEM application, such as pnematic conveying [53], fluidised beds [54–58], flow patterns in a cyclone system [32,59], depositing powder in a dye [60] and sedimentation in water [61]. The CG method has also been used in molecular dynamics. One notable example is the work by Klein and Shinoda [62] where they reduced the number of atoms from 10 million to 3265 individual bodies. The benefit of coarse-graining is two-fold for simulations to run to completion, as a group of particles are replaced by a single, larger particle. This decreases the total number of particles present and calculated Rayleigh's time step will increase with particle size.

The CG method allows the time required for simulating complex particle-fluid interactions to be decreased in operations where dense particle systems can be observed. Hence, it may offer an opportunity to allow larger simulations in the spiral jet mill. The CG method scales the particles based on the number of particles being replaced and preserves mass and volume in an effort to maintain the bulk mechanics of the material. In this study, the CG method is investigated to determine its suitability for predicting its effect on particle behaviour and fluid field in the AS-50 spiral jet mill. In total, four scaled cases are compare to an unscaled simulation. Particle velocity and the dissipated energy of collisions are used to determine the success of the model. The CG method is applied using the same methodology as Sakai [39] and does not include material property scaling. The study does not also consider breakage, so no model to capture size reduction has been implemented.

7.2. Coarse Grain Method in CFD-DEM Framework

The CG method is used only to scale the particles in the simulation, and therefore, the DEM model [63] inside the CFD-DEM framework [15,45] is not altered. To scale particle size, only particles of the same diameter and material may be grouped together. Grouping particles of a different size or material property will alter either translation or rotational component of motion once exposed to the fluid field. There are three criteria that must be ensured when apply the CG method. (i) The number of CG particles must be statistically analogous to the original particle system, so that bulk behaviour is not altered because of scaling. (ii) The collisions that occur between CG particles represents the collective group of particles colliding, hence particle momentum and energy must be preserved during contacts; (iii) The number of CG particles that occupy the fluid cell must occupy the same volume as the original particles, so that the fluid-particle interaction is not miscalculated [32]. To ensure the final criteria, Di Renzo *et al.* [58] suggest that it is necessary to scale the fluid domain when applying the CG method.

Each CG particle represents a number of the original particles and its size can be determine through cube root of the number particles it represents:

$$\varphi = \sqrt[3]{n_p} \quad [32]$$

where φ is the scaling factor used to calculate the new radius of the CG particle and n_p is the number of particles it represents. It then follows that:

$$r_{cg} = \varphi r_o \quad [33]$$

where r_{cg} and r_o is the radius of the CG and original particle, respectively. Furthermore, since the envelop density of the particle is kept constant, the mass and volume of the CG particle can be calculate as follows:

$$m_{cg} = \varphi^3 m_o \quad [34]$$

$$V_{cg} = \varphi^3 V_o \quad [35]$$

where m_{cg} and m_o are the mass, and V_{cg} and V_o are the volume of the CG and original particles, respectively. Since the CG particle represents a group particles, its velocity must equate to the average of the original particles to conserve the kinetic energy of the system:

$$\boldsymbol{v_{cg}} = \overline{\boldsymbol{v}}_{\boldsymbol{o}} \quad [36]$$

where $\boldsymbol{v_{cg}}$ is the velocity of the CG particle and $\overline{\boldsymbol{v}}_{\boldsymbol{o}}$ is the velocity of the original group of particles. When calculating each of the force terms in the momentum

and impulse equation for spherical particles, Sakai [39] suggests that the final equation will be related by the cube power of the scaling factor:

$$\begin{aligned} m_{cg}\boldsymbol{v_{cg}} &= \boldsymbol{F_{f,cg}} - V_{cg}\nabla P + \sum \boldsymbol{F_{c,cg}} + \boldsymbol{F_{g,cg}} \\ &= \varphi^3 \boldsymbol{F_{f,o}} - \varphi^3 V_o \nabla P + \varphi^3 \sum \boldsymbol{F_{c,o}} + \varphi^3 \boldsymbol{F_{g,o}} \end{aligned} \quad [37]$$

where $\boldsymbol{F_c}$ is force due to contact, $\boldsymbol{F_g}$ is the force due to gravity, V is the volume of the fluid cell and ∇P is the pressure gradient. $\boldsymbol{F_f}$ is the fluid drag force and can be written as:

$$\boldsymbol{F_{f,cg}} = \frac{\beta}{1-\varepsilon}\left(\boldsymbol{u} - \boldsymbol{v_{cg}}\right)V_{cg} = \varphi^3 \frac{\beta}{1-\varepsilon}(\boldsymbol{u} - \boldsymbol{v_o})V_o \quad [38]$$

where $\boldsymbol{u}$ is the fluid velocity, ε is the void fraction of the fluid cell and β is the gas-particle momentum transfer interphase coefficient.

7.3. Methodology

The mill used in this study is based on the Hosokawa Micron AS-50 spiral jet mill. An in-house drawing of the mill can be viewed in Chapter 5, Figure 5-1. The mill construction and important features are mentioned there. Its operation is described in Chapter 2. In each case, 1g of particle material is simulated. A base particle size of 100 µm has been chosen. To stop structuring forming in the dense bed brought upon by a mono-sized particle system, a random distribution of (0.8-1.2)r; where *r* is the radius, has been selected for the particle radius upon creation. As well as the original case, four CG cases are investigated. The four CG numbers, n_p are 2, 4, 8 and 10. A value of 40 % particle-to-cell volume ratio is maintained, as suggested by Norouzi *et al.* [16]. However, the highest CG number is limited by the fluid cell volume, since increasing the cell volume can be detrimental to the resolution of the fluid field. Information regarding the mass of particles and gas delivery pressure can be seen in Table 7-1. Each simulation was run for 0.1 s. The particles are added directly into the milling chamber using the standard EDEM™ factory from time t = 0.0 s until 0.01 s in each case. The particle bed is then allowed to form and the particles reach a pseudo-steady state; typically, this occurs at around 0.03 s. Any time sensitive data is only recorded in the final 0.03 s of each simulation.

Table 7-1: Particle amounts per case and fluid pressure

Mass of particles simulated (g)				1
Base particle size (µm)				100
Feed gas pressure (kPa)				500
Grinding gas pressure (kPa)				400
Case	**Coarse grain number (n_p)**	**Scaling Factor (φ)**	**Minimum fluid cell edge length (mm)**	**Particle number**
1	1	1	0.4	233213
2	2	1.26	0.56	117057
3	4	1.58	0.71	58664
4	8	2	0.9	29397
5	10	2.154	1	23550

To calculate the particle motion and collision mechanics is calculated using EDEM™ 2020 (Altair, UK), whereas the fluid flow field is resolved by Fluent 18.1. All particle-fluid interactions are captured in the coupling scheme. To model the gas component of each simulation, the *k*-*ε*-RNG turbulence model is used with scalable wall functions. The 'SIMPLE' pressure-velocity coupling scheme for spatial discretisation is also employed. A tetrahedral mesh is used with the minimum edge length based on the size of an equilateral tetrahedron. Morsi and Alexander [44] drag law is used within Fluent, since spherical particles are being modelled in EDEM™. The particle-drag force is scaled by the corresponding φ value for each case. The particle and gas properties can be seen in Table 7-2.

Table 7-2: Particle and gas properties used in the simulations

Phase	Parameter	Value
Fluid	Viscosity	1.8×10^{-5}
	CFD time step, µs	$8 - 30$
	Minimum cell edge length (no particles), mm	0.4
	Outlet pressure kPa	101
Particle	Density, kg/m^3	1500
	Shear modulus, MPa	10
	Poisson's ratio	0.25
	Coefficient of restitution	0.5
	Coefficient of static friction	0.5
	Coefficient of rolling friction	0.01
	DEM time step, µs	$0.4 - 1.3$

7.4. Results

An image from each DEM simulation taken at time t = 0.1 s is shown in Figure 7-1. Comparing each image, there is no obvious change in the shape of the bed that is the result of applying the CG method. There is some variation in the bed height at different positions, located mainly where the particles approach the jet nozzles. However, this is normal fluctuation of the particle distribution, as the material at the surface of the bed is not as tightly bound and is easily influenced by the high-pressure jets. Noticeable, the jet regions appear to become leaner as the CG number is increased. This difference is less obvious when comparing the cg-1 and cg-2 cases. However, there are dramatically fewer particles in the jets regions of the cg-4, cg-8 and cg-10 cases. This result is predictable, as the number of particles in each system decreases, as the CG number is increased.

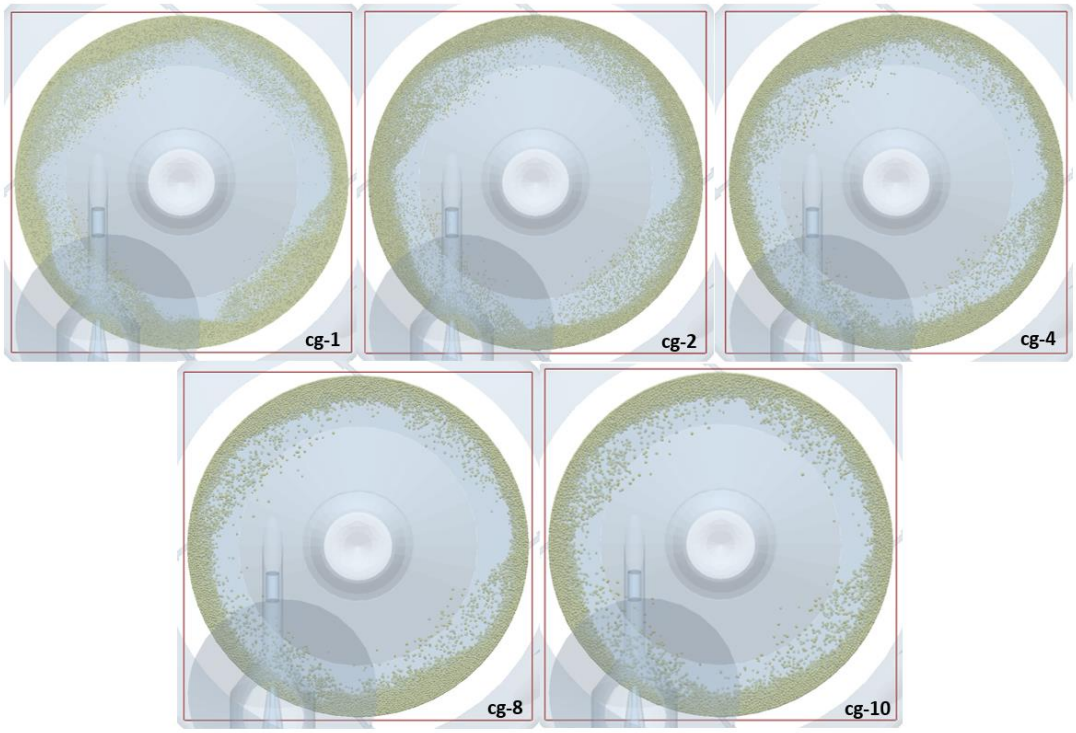

Figure 7-1: Images of the original and CG cases at time t = 0.1 s

Figure 7-2 shows the modulus of the average particle velocity plotted with their position along the x-y plane. The data is collected from 100 random time steps between 0.07 - 0.1 s. The particles are binned by their x and y coordinate positions and the mean value is taken. The velocities shown range from 0 m/s (dark blue) to 30 m/s (dark red). The areas in the images coloured light-blue/teal represents the bed surface, which undulates due to exposure to the jet regions. Particles at this position either are accelerated out of the particle bed, or are shear in the fast-moving layers its surface. The heat maps produced are very similar for all the cases. The particles in the bed travel at a velocity just above 0 m/s to 7 m/s and those in the jet regions travel between 7-20 m/s. Due to the size of the particles used, very few particles travel within the lean region of the mill, and fewer still make it to the centre. As the majority of particles outside the bed travel in the jet regions, this creates a ‘square shape’ that is visible at the centre of each image. The particles motion is govern by the jet direction, and therefore, they are projected the jet axes.

Of the five images, there appears to be some unevenness in the cg-4 case. At the 12 o’clock position, a large amount of particles has piled-up behind the jets. This has lowered the average particle velocity in the jet region, as more energy is dissipated by the jet as it travels through the bed [50]. Despite appearing to have an even in particle bed loading, the cg-10 case has a lower particle velocity in the jet regions than all other cases. Therefore, it can be

concluded that this is a result of the CG method. The particle number has decreased sufficiently that the number of particles no longer represents the original (cg-1) case.

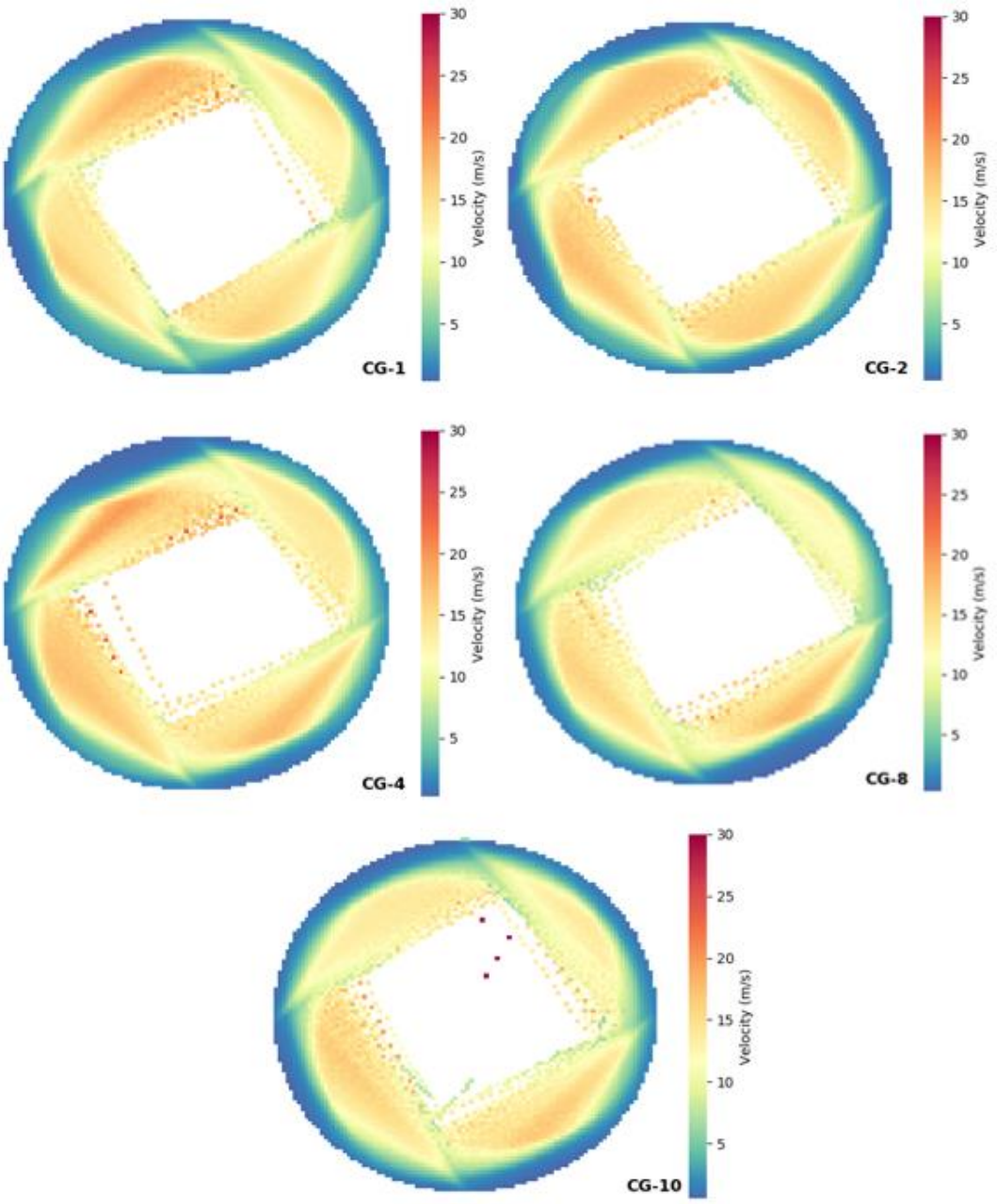

Figure 7-2: Heat map of average particle velocity (m/s) in the mill as a function of their x-y position

Figure 7-3 shows each of the fluid flow fields after the simulation has been stopped at 0.1 s. The velocity ranges from 0 m/s (blue) to 120 m/s (red). Each image is capped at 120 m/s, as this increases the visibility of each region of

the mill and the velocity gradients along their boundaries. There is no significant change in the colour profiles of the mill. The size and shape of the volume occupied by the bed and the lean region all appear similar across the five cases. The jets, coloured red, also do not vary in length. This is an important finding, as it shows that applying the CG method has not adversely affected the jet penetration depth through the bed, and the air has no easier path to the centre of the mill as the particle number decreases. Comparing each image there is some minor variation in colour behind the 12 o'clock jet. Once again, this is can be attributed to particles building-up behind the jet, and will naturally vary with time.

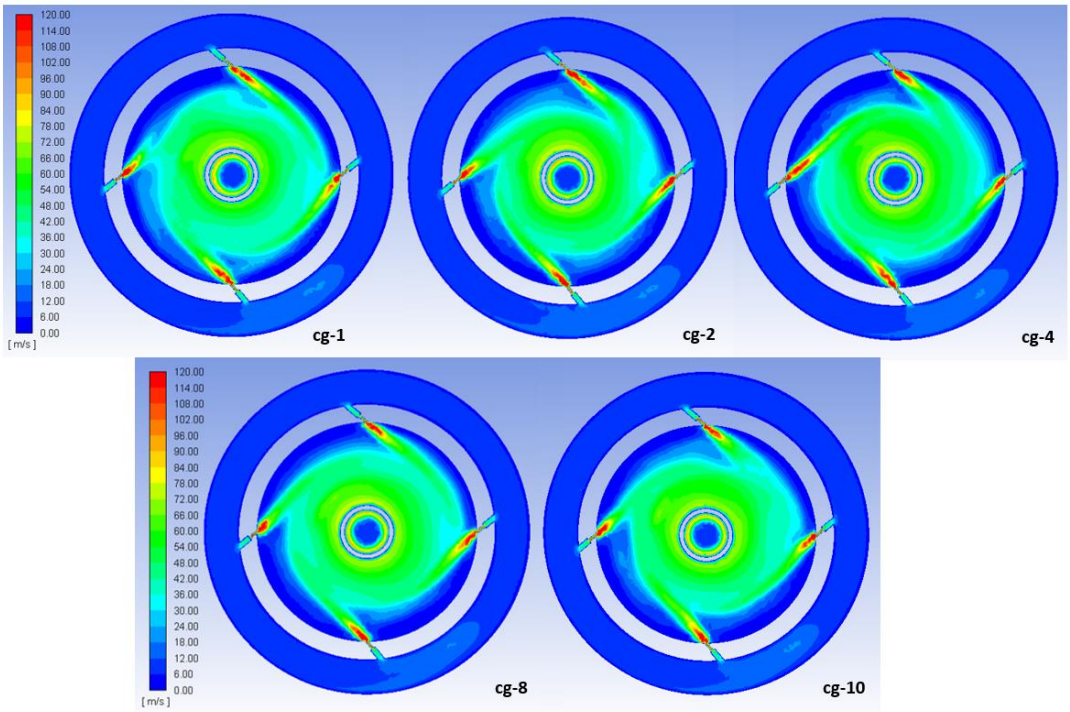

Figure 7-3: Fluid velocity (m/s) along the z-plane at the mid-point of the mill.

The kinetic energy of each particle system is shown in Figure 7-4. Each case starts with an energy value of 0 mJ, at time t = 0.0 s. This is because the particles are created with their velocity equal to zero. However, the value quickly increase, as more particles are added and because the bed remains unformed. Whilst the bed remains unformed, more energy is transferred to the particles. There is a peak in all profiles at time t = 0.01 s, when no more particle are added and the bed is forming. Once each system reach a pseudo-steady state, the kinetic energy reaches an asymptotic value. From this point, the kinetic energy of the particle system naturally fluctuates, as the material

circulates the mill. Overall, there is good agreement between all five cases, even though the particle number has decreased ten-fold. This suggests that the drag force calculation has been correctly applied to the particles.

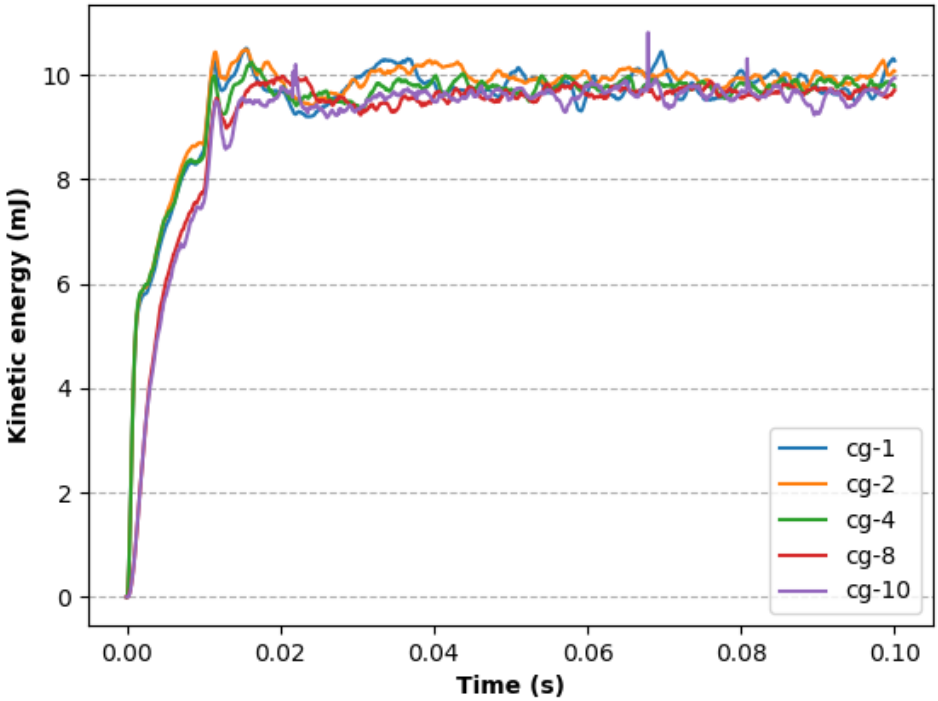

Figure 7-4: Kinetic energy of the particle system against time for each case

Figure 7-5 depicts the velocity profile of the particles in the radial direction from the outer wall. The plot is constructed by using x-y positions of all particles in the mill to calculate the radial distance from the outer wall. The values are then binned by distance and the mean value is taken. The data are collected after 0.07 s from 100 different time steps. It can be seen that there is good agreement between the cases up until 3 mm, as all profiles depict the same velocity gradient. However, after this point, the cases begin to deviate, with the cg-4 case showing the largest deviation. The cg-4 case appears to under-predict the velocity gradient up until around 7 mm, and then over-predict further into the mill. The under-estimation in the velocity could be due to the build-up of particles at 12 o'clock position, as previously discussed. However, the difference in the profile from the original case suggests that the CG method is failing to predict the particle velocity outside the bed region.

The cg-2 case seems to over-predict the particle velocity outside the bed region. There is no unevenness in the particle bed distribution; therefore, scaling the particles may be the cause of the issue. It is interesting that the highest CG cases, cg-8 and cg-10, are more agreeable with the original

particle system, even in the lean region. However, for all CG cases, the results will become unreliable and it is unrealistic that there is enough particles present for the CG model to be correct. Yet, this point is less significant at this distance from the wall. Size reduction is most prevalent in the top layers of the bed and close to the jets [24,31,50].

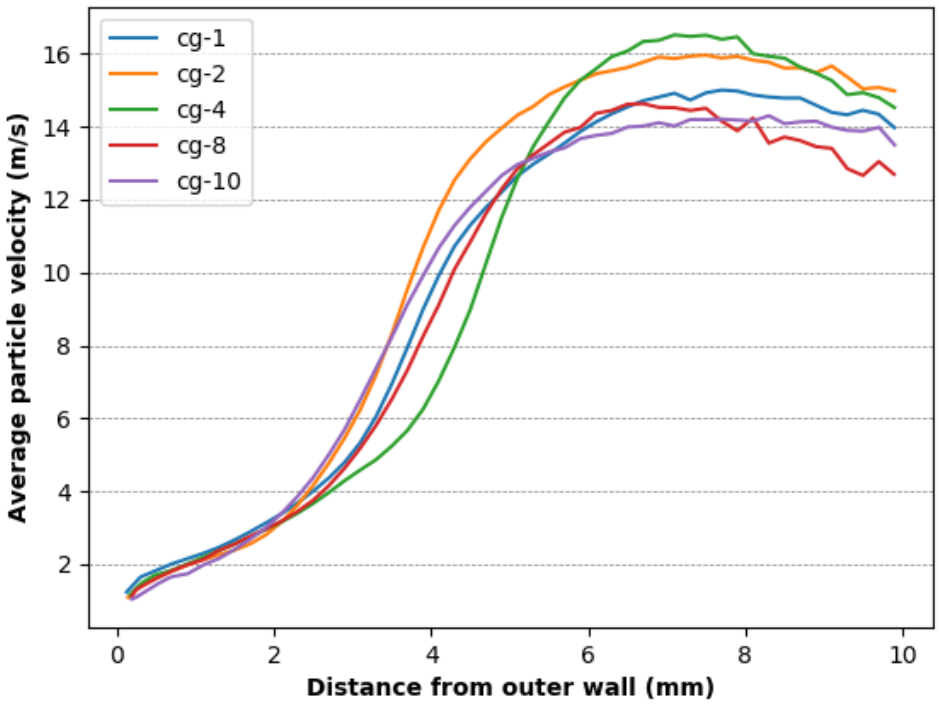

Figure 7-5: Profile of particle velocity plotted as a function of distance from the outer wall. Data collected after 0.07 s.

As expected, the number of collisions decreases, as the number of particles present also decreases. This can be seen in Figure 7-6. The collision frequency is calculated for collisions occurring between time t = 0.07 – 0.1 s. This includes both interparticle and particle-wall collisions. From cg-1 to cg-2, the collisions frequency decreases by around 55%. From cg-2 to cg-4, the collision frequency decreases by a further 60% and from cg-4 to cg-8 by another 65%. This decrease in collision frequency is substantial considering the computational effort in modelling the contact mechanics, as well as detecting collisions that might occur in that time step.

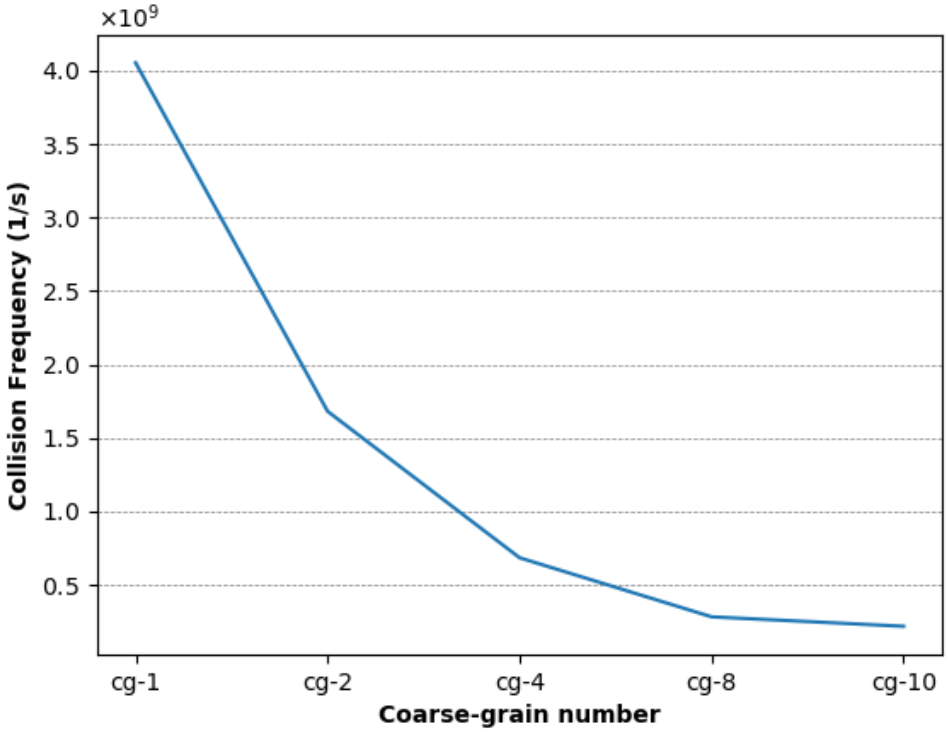

Figure 7-6: Calculated collision frequency (1/s) for each case between time t = 0.07 – 0.1 s

Finally, the dissipated energy through interparticle and particle-wall collisions is presented in Figure 7-7 for all cases. To improve the readability of the plot, the mean value for the collisions in a time step is used. When comparing the graph, the cg-1, cg-2 and cg-4 profiles agree well, even though the number of particles has halved and quartered, respectively. However, the cg-8 and cg-10 profiles present a decrease in the recorded collision energy. The most likely explanation for this decrease in the dissipated energy is the decreased number of particle contacts occurring outside the bed region. Since there are fewer particles that exist outside the bed for these cases, the CG methodology will not hold true. Therefore, this scaling method may not be suitable at high CG numbers within the spiral jet mill, if the lean region is of importance.

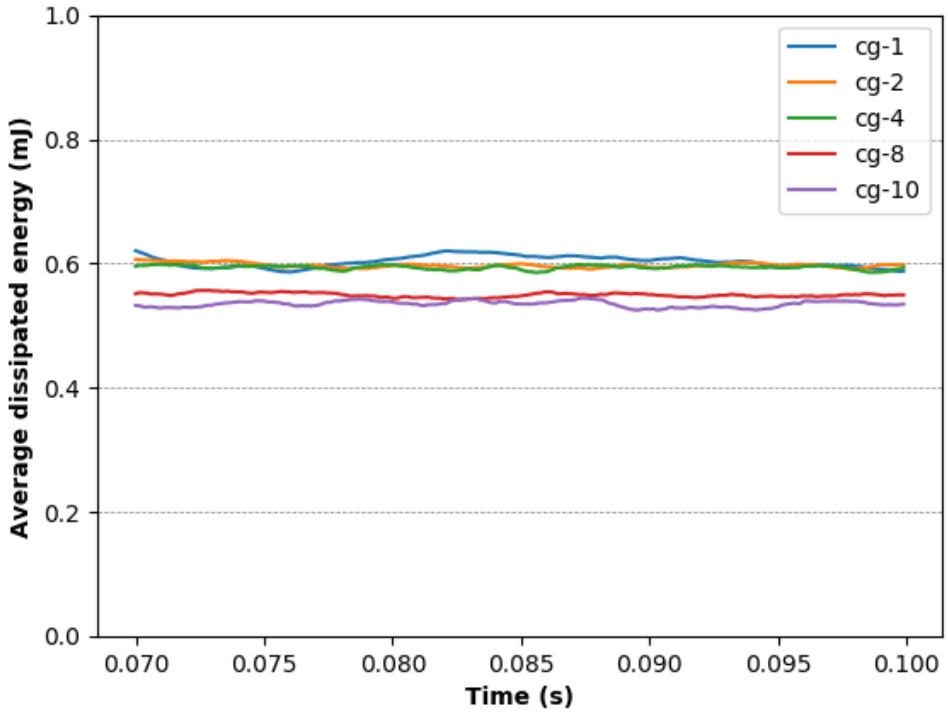

Figure 7-7: Energy dissipated through particle collisions from time t = 0.07 – 0.1 s.

7.5. Conclusions

The CG method was applied to a coupled CFD-DEM simulation of the Hosokawa Micron AS-50 spiral jet mill. The validity/applicability of the model was assessed based on the behaviour of particles at different scaling factors. In total, five cases were analysed, the original and the four scaled cases (n_p = 2, 4, 8, 10). The shape of the bed and the fluid field was first analysed qualitatively. There was good agreement between each of the scaled cases against the original case, even though the particle number had been severely reduced. Overall, the bed shape was maintained and there was no change in the fluid velocity profiles. Only in the cg-4 was there some change in the bed depth found. However, this was attributed to normal particles build-up behind the jets.

The system was allowed to reach a pseudo-steady-state and the kinetic energy of the particles was monitored before any quantitative data was recorded. It was found that there was good agreement between all systems when modelling the particle velocity in the dense particle bed. However, outside the bed region, the velocity profiles became dissimilar. It was concluded that the number of scaled particles outside the bed could no longer represent the particles in the same positions in the original case. Yet, this may

not disadvantage the CG method form being used to model the spiral jet mill, as milling predominately occurs in the rapid shearing layer at the bed surface.

Finally, as expected, the collision rate decreased, as the scaling factor was increased. However, for the two lowest CG cases (cg-2 & cg-4), the dissipated energy agreed well with that of the original case. However, the two larger cases (cg-8 & cg-10) underestimated the energy dissipated thorough particle collisions. Hence, this leads to the conclusion that applying the CG method may be beneficial for simulating the spiral jet mill to decrease the computational requirements. However, there are limitations, as both lean and dense phases need to be modelled if a complete simulation of the mill is required.

Chapter 8 Modelling breakage in the spiral jet mill

8.1. Introduction

The difficulty in modelling the spiral jet mill accurately is due to the small size and large number of particles present in the mill. The spiral jet mill is capable of producing a very fine powder (5-20 µm) with a narrow size distribution. This constrains DEM simulations to what is physically achievable given the computational requirements. Hence, in most cases large-scale CFD-DEM simulations are infeasible even without breakage modelling present.

Breakage has been previously modelled in the spiral jet mill. Brosh *et al.* [43], using an in-house code, modelled breakage in coupled CFD-DEM simulation. Their breakage model, based on the work of Han *et al.* [64] and Kalman *et al.* [65], included both size reduction and fatigue, allowing the particle to weaken if they did not meet the criteria to break. To speed up their simulations they did not model the fine material; as they assumed it would leave the mill shortly after being produced. Unrelated to the spiral jet mill and using a different model, Bonakdar and Ghadiri [66] investigated high velocity impacts in a pin mill. Through experimental acquisition, they describe the shift in surface area during breakage as a function of particle size, velocity and material properties:

$$\frac{\Delta SSA}{SSA_o} = \frac{\beta \rho_f \bar{d}_f v_i^2 H}{K_c^2} \times \frac{\bar{d}_f}{\bar{d}_d} \qquad [39]$$

where ΔSSA is the change in surface area, SSA_o is the original surface area, $\bar{d}_f$ is the average diameter of the feed particles, $\bar{d}_d$ is the average diameter of the debris, ρ_f is the envelope density of the feed particles, $v_i$is the relative impact velocity, H is the material hardness, K_c is the fracture toughness and β is a proportionality constant. The material hardness, fracture toughness and proportionality constant can be grouped in a single term ($\beta H/K_c^2$) known as the breakability index and determined through linear regression to obtain a final breakage kernel. Using the determined breakage kernels for three separate materials, the authors found agreement with the experimental data for predicting size reduction by chipping.

In this section the breakage by chipping in the spiral jet mill is investigated. To model breakage, the Ghadiri and Zhang chipping model [67] was implemented in conjunction with the work of Dogbe [25] and Bonakdar and Ghadiri [66]. Size reduction is expressed in terms of fractional loss of material from the mother particles herein referred to as mass loss. The collision frequency and position is also analysed as a function of successful breakage events. Finally, the milling efficiency is calculated as a function of the fluid power (Equation

[29]) injected into the mill by the jets. This work only considers size reduction by high velocity collisions, and therefore, does not consider the size reduction by shear straining.

8.2. Methodology

The Hosokawa Micron AS-50 spiral jet mill is used in this study. The in-house drawing of the mill can be viewed in Chapter 5, Figure 5-1, and its operation is described in Chapter 2. Three mass loadings; 1, 1.4 and1.8 g are simulated, as well as three grinding pressures; 3, 4, 5 barg. The feed gas pressure is maintained at 1 barg above the grinding gas pressure, so that no backflow is possible and the outlet pressure is set to atmospheric. Spherical particles are simulated with a base radius (r) of 100 μm and a random size distribution of (0.8 – 1.2)r. The use of a size distribution stops the creation of structures forming in the dense packed bed brought upon when using a mono-sized particle. The solid material investigated in this study is modelled on paracetamol, whereas the gas is based on air. The material properties and simulation values that are used in this study can be seen in Table 8-1 and breakability values were found experimentally by Bonakdar and Ghadiri [68]. Size reduction is calculated as a function of particle radius and velocity; however, it is limited to 0.6r. This is to limit the reduction in the Rayleigh's time step. The fine material removed from the particles due to size reduction is assumed to exit the mill, without becoming trapped in the bed. Therefore, the fine material is not simulated to reduce the computational overhead required.

Table 8-1: Material properties and simulation values based on the work of Bonakdar and Ghadiri [68].

Phase	Parameter	Value
Particle	Shape	Spherical
	Particle radius (µm)	100
	Mass loading (g)	1, 1.4 & 1.8
	Density (kg/m^3)	1290
	Shear Modulus (Pa)	1×10^8
	Coefficient of restitution	0.35
	Coefficient of static friction	0.5
	Coefficient of rolling friction	0.01
	Breakability index	0.0841
	Breakage coefficient	-1.2142
Fluid	Material	Air
	Grinding gas pressure (barg)	3, 4 & 5
	Feed gas pressure (barg)	4, 5 & 6
	Density (kg/m^3)	1.225
	Specific heat capacity (J/kg.k)	1006.43
	Viscosity (kg.m/s)	1.78×10^{-5}
	Minimum cell length (mm)	0.4
	Outlet pressure (kPa)	101

To calculate the motion of the particles EDEM^{TM} 2020 (Altair, UK) is used, whereas the fluid field is resolved by ANSYS Fluent 18.1. The two software packages are coupled using a two-way scheme. To model the gas (Air), the *k*-*ε*-RNG turbulence model with scalable wall functions is used. The SIMPLE coupling scheme for spatial discretisation is used to predict the pressure and velocity values. A tetrahedral mesh is used, with a minimum edge length of 0.4 mm. Since the particles in this study are spheres, the Morsi and Alexander [44] drag law is used inside Fluent. A solution for the fluid flow field is first found before any solid material is added into mill. Once solved, the particles are added directly into the milling chamber in an annular ring as described in Chapter 4 and using the standard EDEM^{TM} factory. Each simulation is allowed to run for a total of 0.1 seconds of real time.

8.3. Results

Figure 8-1 depicts the average particle radius with respect to time for each combination of pressure and mass loading, and it is clear that in all cases using a larger grinding gas pressure leads to a greater extent of size reduction. In the 1.0 g case, the average particle radius only decreases by a small amount when 3 barg of pressure is used. In comparison, at 5 barg grinding gas pressure, the particle size has decreased so significantly the cap of 0.6r

has almost been achieved. As the particles reach their terminal size, the gradient of slope in the 5 barg case begins to decrease, as breakage becomes less likely due to small particle size. The 4 barg case follows a similar trend as the 5 barg, but size reduction is slightly diminished.

In the 1.4 g it is clear that mass loading has had an effect on the rate of size reduction, as all cases have a larger particle size at time t = 0.1 s, when compared to the 1.0 g cases. The growth of the particle bed and the reduction in the mean-free-path of the particles decreases the time allowed for particles to accelerate in-between collisions. In Figure 8-1 the 4 barg case now more closely aligns with the 3 barg case rather than the 5 barg due to the effect of mass loading. The rate in size reduction is further diminished as the mass loading is increased to 1.8 g. The average particle size is reduced by less than 2% at time t = 0.1 s due to increased number of particles present.

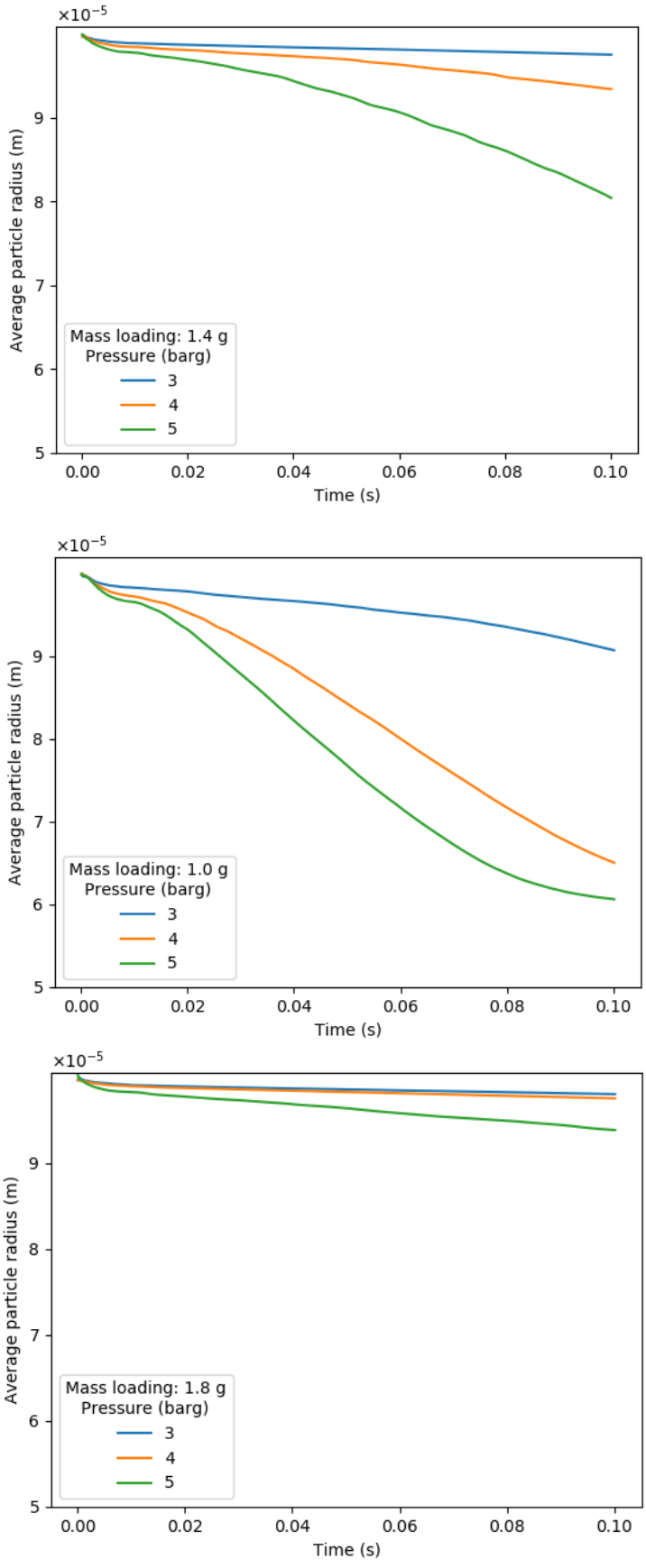

Figure 8-1: Average particle radius with respect to time for each pressure and mass loading

For completion, the mass loss recorded with respect to time is shown in Figure 8-2, for each combination of grinding gas pressure and mass loading. Each of the graphs reflects the same trend as its counterpart for particle size reduction in Figure 8-1. The combination of high velocity and a greater amount of time to accelerate in between collisions result in an increased mass loss in the 1 g case at 4 and 5 barg when compared to the other cases.

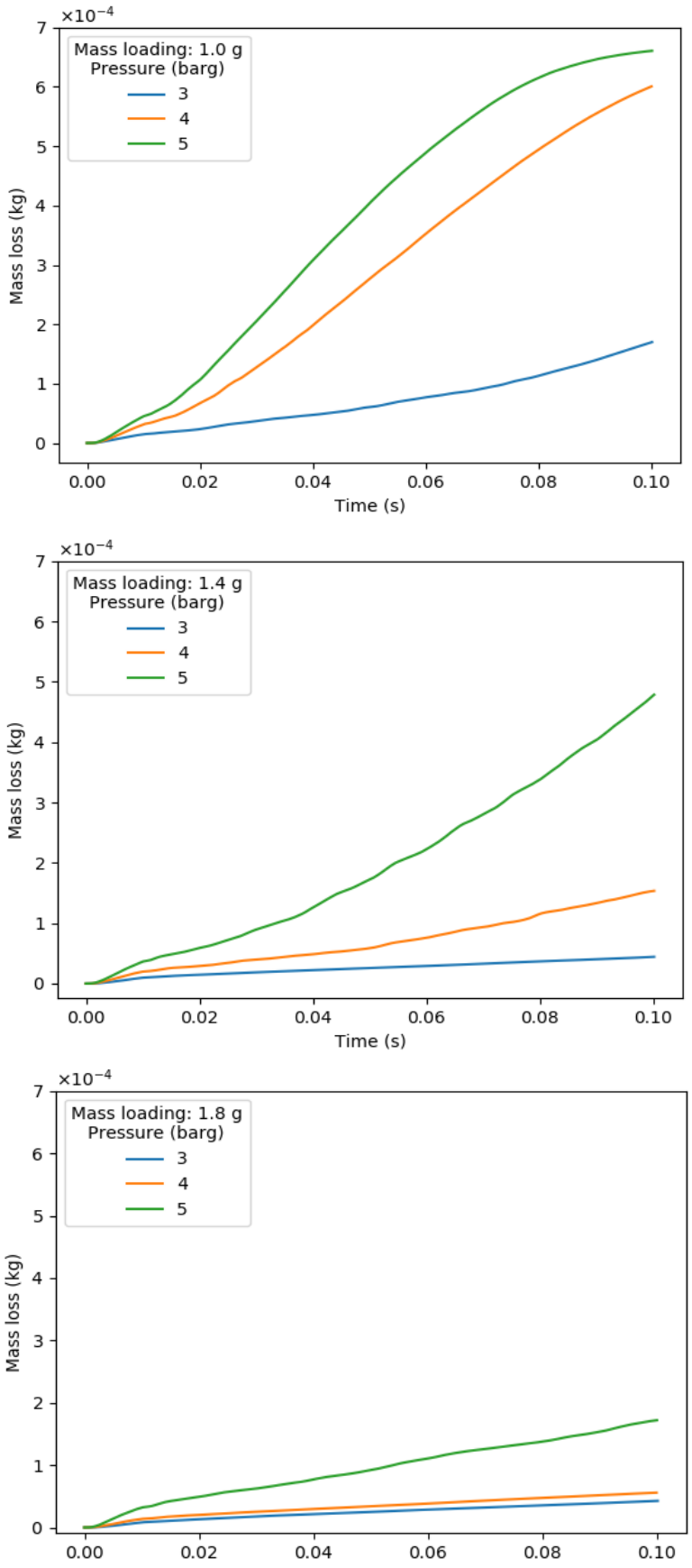

Figure 8-2: Mass loss recorded with respect to time for each combination of mass loading and grinding gas pressure

Figure 8-3 depicts the mass of debris per unit of fluid energy (energy utilisation) expended reducing the particles in size. To calculate the total energy expended reducing particle size, the theoretical fluid power (*W*) injected into the mill through the grinding jets is calculated using the pressure drop over the nozzles, and using the Equation 38, as given by Green and Southard [51], for calculating the theoretic mass flux:

$$G = P_o \sqrt{\frac{\gamma M_w}{R T_o}} \frac{M_1}{(1+\frac{\gamma-1}{2} M_1^2)^{(\gamma+1)/2(\gamma-1)}} \quad [40]$$

where G is the mass flux, M_w is the molecular weight of the gas, M_1 is the Mach number of the gas, *R* is the gas constant, P_o and T_o is the upstream pressure and temperature of the gas and γ is the ratio of specific heat capacities at constant pressure and constant volume. The pressure drop was found by analysing the fluid fields in ANSYS Fluent. It can be seen in Figure 8-3, that the 4 barg case at 1 g mass loading recorded the highest work value. Increasing the pressure to 5 barg results in a decrease in mass-to-power ratio. This suggests that as the grinding gas pressure is increased from 4 to 5 barg, the mill has become less energy efficient. The particle size may be decreased more rapidly at the higher pressure, as shown in Figure 8-1, however it is doing so at the expense of wasting energy. This also suggests that there is an optimum efficiency that could be achieved to minimise total power consumption. The 5 barg case with 1.4 g of material has a higher work efficiency than the 3 barg – 1g system. However, all other cases appear to lower work value. This is interesting, as it means that the mass loading is directly affecting the breakage rate; however, it is not unexpected. The increase in particle number results in a greater number of less energetic collisions, which occur with greater frequency. They are less energetic as more fluid energy available is limited by what is injected through the grinding gas nozzles.

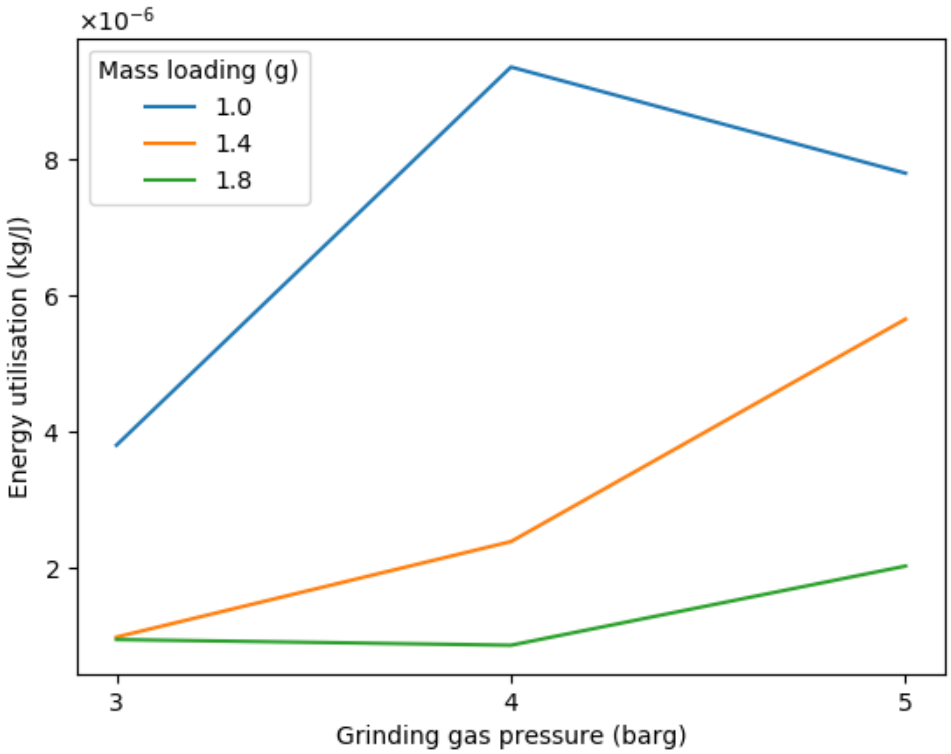

Figure 8-3: Energy utilised producing debris as a function of grinding pressure and mass loading

A spatial heat map of breakage events through inter-particle collisions can be seen in Figure 8-4. Each figure is recorded from 50 random time steps after the particle bed has formed. A sample size of 50 has been chosen as the number of collisions is very high; over 400,000 collisions per save interval of 1 µs in some instances. Successful collisions are coloured from blue to red denoting a low and high value of breakage event at a given position, respectively. Collisions that are do not lead to size reduction are coloured grey. The unsuccessful collisions also provide a sense of position where successful positions are taking place and where the particles are travelling in the milling chamber. In the 1.0 g case, size reduction is dominant along the bed surface and along the front side of the jets. The regions of high size reduction also become smaller, as the pressure is increased. The increased pressure causes the particles in the jet regions to become more tightly packed in the shearing bed and move more closely to the outer wall. The number of breakage events that occur in the jet region also increases as pressure increases. However, their number is still low in comparison to those at the bed surface, as particles in the jet region will collide with a low relative velocity.

As the mass loading is increased to 1.4 g, there is no longer a continuous region where size reduction occurs in the 3 barg case. Instead, breakage events occur close to the jet nozzle and around the mid-point of the bed in between two jets, at the surface. In the 4 and 5 barg cases, the surfaces of the particle bed are highlighted once again by the high number of breakage events occurring. Once the mass loading is increased again to 1.8 g, the area of breakage separates into distinct regions close to jet nozzles for the 3 and 4 barg pressure cases. Even at 5 barg, the areas where breakage has been recorded have reduced in size. Particles also break less commonly in the jet regions, even though the grey area denotes they travel and collide in that region.

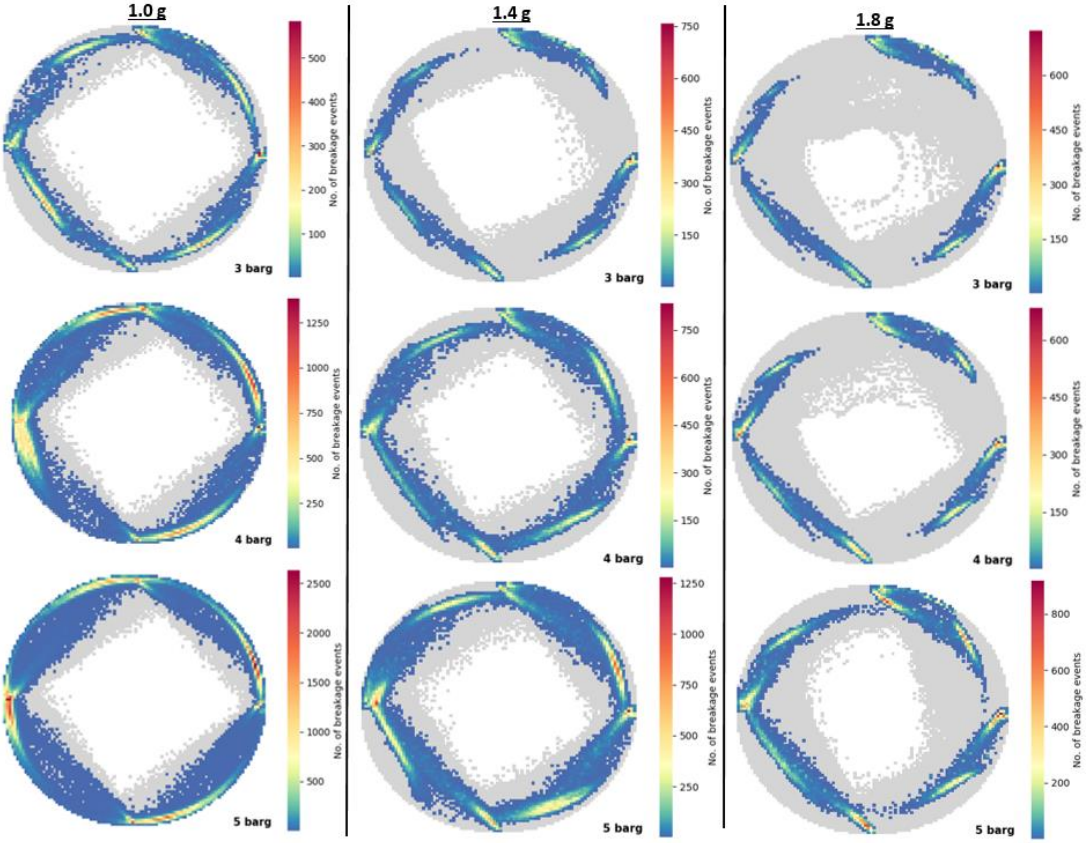

Figure 8-4: Heat map of breakage events by inter-particle collisions plotted as a function of x-y position and number.

Figure 8-5 depicts the spatial map of particle-geometry collisions as a function of x-y position and collision number. Once again, 50 random time steps are used to construct each plot once the particle bed has been formed. The grey colour highlights unsuccessful collisions that due not lead to breakage, whereas successful collisions are coloured from blue (low) to red (high).

Within each plot, there is the area of breakage located at the “1 o’clock” position along the outer wall. This is because the fluid flow field is asymmetric due to the position of the feed nozzle. Its presence causes the fluid field to become distorted, leading to particle collisions in the mentioned area.

An interesting observation, not commonly mentioned in the literature, is the number of particle-wall collisions happening in the jet region with the ceiling and base of the mill. It is clear from the images that once the bed forms, breakage against the outer wall is limited due to slow shearing layer previously discussed [24,31,50]. However, the plots show that the relative velocity is high enough allow size reduction to occur in the jet regions with the ceiling and base of the milling chamber. This behaviour in the mill seems to increase with grinding gas pressure, but decrease with particle mass loading, as more energy is needed to accelerate the increased number of particles. Yet, this might not be the case given the velocity magnitude is used in the breakage calculation. It may be more appropriate to use the normal velocity, given the small angles at which the particle collide with the mill surfaces.

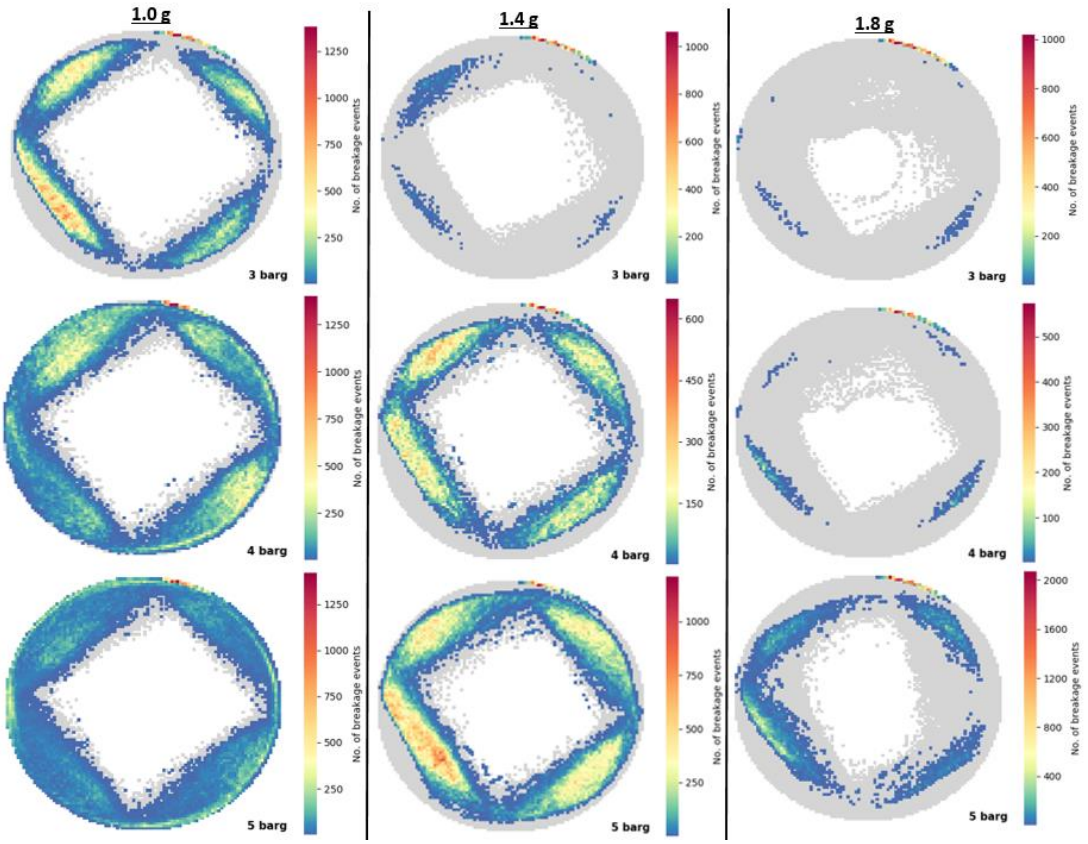

Figure 8-5: Heat map of breakage events by particle-geometry collisions as a function of x-y position and number

8.4. Conclusions

Using a coupled CFD-DEM simulation with an in-house breakage model based on the Ghadiri & Zhang chipping model, size reduction in the Hosokawa Micron AS-50 spiral jet mill is simulated. In total nine cases are analysed using three mass loading (1.0, 1.4 & 1.8 g) and three grinding gas pressures (3, 4, 5 barg). Particle mass loss and size are analysed and it is shown that increasing the mass loading adversely affected the rate of breakage. The presence of more particles led to a decrease in the rate particle size reduction, which can be attributed to a greater number of less energetic collisions.

Next, the energy utilisation used to reduce the particle size is presented. This was calculated using the theoretical mass flux through the four grinding nozzles and pressure drop recorded using Fluent. It is shown that the energy provided for breakage is used most effectively when smaller mass loadings is present in the mill chamber. The 3 barg also showed that there is a local maximum before increasing the grinding pressure any further becomes ineffective and energy is wasted.

Finally, particle collisions were shown as a function of position and number in heat map form. Interparticle collisions are prevalent along the surface of the bed, as they are exposed to the high velocities that increase the chance of breakage occurring; though, this is shown to decrease as the mass loading was increased from 1.0 g to 1.8 g. It was noteworthy that particle-geometry collisions are also prevalent in the mill, but occur in the jet region as the particle come into contact with the ceiling and base of the milling chamber. It was unexpected that the relative velocity would be high enough to allow for size reduction to occur, given the small impact angles (glancing blow).

Chapter 9 Future Work

Throughout this thesis the work has concerned the role of dynamic behaviour within the particle bed and jet regions; focusing on where particle breakage is likely to occur. Following this work, it would be of interest to see how the smallest particles arrange themselves closer to the classifier after being liberated from the bed and if the fluid field is affected by their presence. There is little to no information in the literature regarding particle trajectory after being liberated from the bed. However, if the particle number is great enough then they should influence the fluid field surrounding the classifier ring.

Continuing to develop a complete breakage model should be a priority in future work. The current model in this thesis only considers high impact collisions; hence, ignoring the work done by abrasion which will occur as the particle layers shear across one another. With both models of breakage present it will provide a definite answer over which has a greater influence on size reduction.

The coarse grain method is continually being developed and used by different groups [59,69,70]. In the section of work containing coarse graining, only particle scale was considered. The particle properties were left unscaled, as the effect of the grinding gas jets dominates particle trajectory. However, if particle breakage is to be combined with a scaling method, then the particle properties will also need to be scaled appropriately to model the contact behaviour.

To complete the model of the spiral jet mill, the feed stream of particle should be simulated. However, this is contingent on a breakage model being and a scaling solution being present. A complete model of a spiral jet mill is still infeasible given the amount of small particles that would need to simulated. However, whilst the literature agrees that the feed rate influences the final particle size, there is no little discussion on how the particles affect the fluid field upon entering the chamber through the feed nozzle.

Finally, the model should be validated against its physical counterpart. This can be done in two stages. First, the air velocity components can be predicted to give an estimated cut-size, followed by comparing liberated particles from the simulation exit against the product form the physical mill.

In summary, work should continue to develop a more complete breakage model. The effect of particle presence around the classifier and entering from the feed tube should also be studied. A scaling method, such as coarse graining that also considers particle properties, should be incorporated to

reduce simulation time. Finally, physical experimentation should be used to validate the model and what can be achieved!

List of References

[1] J.F. Richardson, J.H. Harker, J.. Backhurst, (1991) Chem. Eng. Sci. **2** 1183.

[2] R.P. Patel, A.H. Baria, N. a Patel, (2008) Asian J. Pharm. **2** 216–220.

[3] S. Sushant, K. Archana, (2013) Int. Res. J. Pharm. **4** 57–64.

[4] F. Müller, R. Polke, G. Schädel, (1996) Int. J. Miner. Process. **44**–**45** 315–326.

[5] M. Metboul, J.F. Large, P. Guigon, (1996) Int. J. Miner. Process **44**–**45**.

[6] B.E. Launder, D.B. Spalding, (1974) Comput. Methods Appl. Mech. Eng. **3** 269–289.

[7] D.C. Wilcox, Turbulence Modeling for CFD, 2nd ed., 1993.

[8] D.C. Wilcox, Turbulence Modeling for CFD, 3rd Editio, DCW Industries, Inc., Glendale, 2010.

[9] E. Kuhl, G. Antonio D'addetta, H.J. Herrmann, E. Ramm, A Comparison of Discrete Granular Material Models with Continuous Microplane Formulations, Springer-Verlag, 2000.

[10] Z.P. Bazant, P.C. Prat, MICROPLANE MODEL FOR BRITTLE-PLASTIC MATERIAL: I. THEORY, 1988.

[11] A. Di Renzo, F.P. Di Maio, (2004) Chem. Eng. Sci. **59** 525–541.

[12] H.P. Zhu, Z.Y. Zhou, R.Y. Yang, A.B. Yu, (2007) Chem. Eng. Sci. **62** 3378–3396.

[13] P.W. Cleary, (2001) Int. J. Numer. Anal. Methods Geomech. **25** 83–105.

[14] Y. Tsuji, T. Tanaka, T. Ishida, (1992) Powder Technol. **71** 239–250.

[15] B.H. Xu, a. B. Yu, (1997) Chem. Eng. Sci. **52** 2785–2809.

[16] H. Norouzi, R. Zarghami, R. Sotudeh-Gharebagh, N. Mostoufi, Coupled CFD-DEM Modeling, John Wiley & Sons, Chichester, 2016.

[17] D. Gidaspow, Multiphase Flow and Fluidization, 1994.

[18] M. Ramanujam, D. Venkateswarlu, (1969) Powder Technol. **3** 92–101.

[19] R. Tuunila, L. Nyström, (1998) Miner. Eng. **11** 1089–1094.

[20] N.P.B. Rajendran, (1999) Powder Technol. **106** 45–53.

[21] A. Katz, H. Kalman, (2007) Part. Part. Syst. Charact. **24** 332–338.

[22] S. Palaniandy, K.A.M. Azizli, H. Hussin, S.F.S. Hashim, (2008) Miner. Eng. **21** 380–388.

[23] S. Dogbe, M. Ghadiri, A. Hassanpour, C. Hare, D. Wilson, R. Storey, I. Crosley, (2017) EPJ Web Conf. **140** 7–10.

[24] L. Scott, A. Borissova, A. Burns, M. Ghadiri, (2021) Powder Technol. **377** 233–243.

[25] S.C. Dogbe, Predictive Milling of Active Pharmaceutical Ingredients and Excipients, The University of Leeds, 2017.

[26] M. Mebtoul, J.F. Large, P. Guigon, (1996) Int. J. Miner. Process. **44**–**45** 77–91.

[27] S. Teng, P. Wang, L. Zhu, M.W. Young, C.G. Gogos, (2009) Powder Technol. **195** 31–39.

[28] R. MacDonald, D. Rowe, E. Martin, L. Gorringe, (2016) Powder Technol. **299** 26–40.

[29] V. Rodnianski, N. Krakauer, K. Darwesh, A. Levy, H. Kalman, I. Peyron, F. Ricard, (2013) Powder Technol. **243** 110–119.

[30] P. Nair, M. Ramanujam, (1992) Adv. Powder Technol. **3** 273–284.

[31] B. Luczak, R. Müller, C. Kessel, M. Ulbricht, H.J. Schultz, (2019) Powder Technol. **342** 108–117.

[32] K. Chu, J. Chen, A. Yu, (2016) Miner. Eng. **90** 43–54.

[33] B. Dobson, E. Rothwell, (1969) Powder Technol. **3** 213–217.

[34] T. Tanaka, (1972) Ind. Eng. Chem. Process Des. Dev., **11** 238–241.

[35] H. Kürten, H. Rumpf, (1966) Chemie Ing. Tech. **38** 331–342.

[36] H. Kürten, H. Rumpf, (1966) Chemie Ing. Tech. **38** 1187–1192.

[37] B. Luczak, Flow Conditions inside Spiral Jet Mills and Impact on Grinding Performance Dissertation Zur Erlangung Des Akademischen Grades Eines, Universitat Duisburg-Essen, 2018.

[38] W. Zhong, A. Yu, X. Liu, Z. Tong, H. Zhang, (2016) Powder Technol. **302** 108–152.

[39] M. Sakai, (2016) ©2016 Hosokawa Powder Technol. Found. KONA Powder Part. J. No **33** 169–178.

[40] S. Bnà, R. Ponzini, M. Cestari, C. Cavazzoni, C. Cottini, A. Benassi, (2020) Powder Technol. **364** 746–773.

[41] S. Teng, P. Wang, Q. Zhang, C. Gogos, (2011) Powder Technol. **208** 684–693.

[42] A.B. T Brosh, Y Batat, H Kalman, A Levy, (2008) Bulk Solids Powder Sci. Technol **3** 83–88.

[43] T. Brosh, H. Kalman, A. Levy, I. Peyron, F. Ricard, (2014) Powder Technol. **257** 104–112.

[44] S.A. Morsi, A.J. Alexander, (1972) J. Fluid Mech. **55** 193–208.

[45] Y. Tsuji, T. Kawaguchi, T. Tanaka, (1993) Powder Technol. **77** 79–87.

[46] Z. Yuan, E.E. Michaelides, (1992) Int. J. Multiph. Flow **18** 779–785.

[47] D. Behrens, (1965) Chemie Ing. Tech. **37** 473–483.

[48] A. Di Renzo, F.P. Di Maio, R. Girimonte, B. Formisani, (2008) Powder Technol. **184** 214–223.

[49] S. Elghobashi, Particle-Laden Turbulent Flows: Direct Simulation and Closure Models, 1991.

[50] L. Scott, A. Borissova, A. Burns, M. Ghadiri, (2021) Powder Technol. **394** 439–447.

[51] D.W. Green, M.Z. Southard, Perry's Chemical Engineers' Handbook, 9th Edition, McGraw-Hill Education, 2019.

[52] Y. Mori, M. Sakai, (2020) Particuology.

[53] M. Sakai, S. Koshizuka, (2009) Chem. Eng. Sci. **64** 533–539.

[54] M. Sakai, M. Abe, Y. Shigeto, S. Mizutani, H. Takahashi, A. Viré, J.R. Percival, J. Xiang, C.C. Pain, (2014) Chem. Eng. J. **244** 33–43.

[55] M. Girardi, S. Radl, S. Sundaresan, (2016) Chem. Eng. Sci. **144** 224–238.

[56] L. Lu, K. Yoo, S. Benyahia, (2016) Ind. Eng. Chem. Res **55** 10477–10491.

[57] A. Nikolopoulos, A. Stroh, M. Zeneli, F. Alobaid, N. Nikolopoulos, J. Ströhle, S. Karellas, B. Epple, P. Grammelis, (2017) Chem. Eng. Sci. **163** 189–205.

[58] A. Di Renzo, E.S. Napolitano, F.P. Di Maio, (2021) Process. 2021, Vol. 9, Page 279 **9** 279.

[59] E.S. Napolitano, A. Di Renzo, F.P. Di Maio, (2022) Sep. Purif. Technol. **287** 120591.

[60] P.M. Widartiningsih, Y. Mori, K. Takabatake, C.Y. Wu, K. Yokoi, A. Yamaguchi, M. Sakai, (2020) Powder Technol. **371** 83–95.

[61] Z. Xie, Y. Shen, K. Takabatake, A. Yamaguchi, M. Sakai, (2020) Powder Technol. **361** 21–32.

[62] M.L. Klein, W. Shinoda, (2008) Science (80-.). **321** 798–800.

[63] P.A. Cundall, O.D.L. Strack, (1979) Géotechnique **29** 47–65.

[64] T. Han, Y. Petukhov, A. Levy, H. Kalman, (2006) Adv. Powder Technol. **17** 135–157.

[65] H. Kalman, V. Rodnianski, M. Haim, H. Kalman, V. Rodnianski, · M Haim, (2009) **11** 253–266.

[66] T. Bonakdar, M. Ghadiri, (2018) Int. J. Pharm. **552** 394–400.

[67] M. Ghadiri, Z. Zhang, (2002) Chem. Eng. Sci. **57** 3659–3669.

[68] T. Bonakdar, M. Ghadiri, (2018) Int. J. Pharm. **552** 394–400.

[69] N. Kishida, H. Nakamura, H. Takimoto, S. Ohsaki, S. Watano, (2021) Powder Technol. **390** 1–10.

[70] Y. Mori, M. Sakai, (2021) Particuology **59** 24–33.

List of Abbreviations

Variable	Definition	Units
cd	drag coefficient	~
D	Milling chamber diameter	m
d	diameter	m
d_{cut}	cut size diameter	m
F	Force	N
F_c	Contact force	N
F_f	Fluid force	N
F_g	Gravitational Force	N
G	Mass flux	$kg/m^2.s$
g	gravitational constant	$m^3/kg.s^2$
H	Hardness	N/mm^2
h	height	m
K_c	toughness	J/m^3
M	Mach number	~
Mw	Molecular weight	g/mol
m	Mass	kg
m	Mass flow rate	kg/s
n_p	Number of particles in grain	~
P	Pressure	Pa
P_o	Upstream Pressure	Pa
R	Gas constant	J/K.mol
r	radius	m
T	Temperature	K
T_o	Upstream temperature	K
t	Time	s
V	Volume	m^3
v	Velocity	m/s
β	Momentum interphase coefficient	~
γ	Heat capacity ratio	~
ε	Void fraction	~
ρ	Density	Kg/m^3
φ	Scaling factor	~

Subscript	Definition
c	classifier
cg	coarse grain
f	fluid
g	gas
r	radial
t	tangential

Appendix

```
/**************************************
BREAKAGE MODEL
**************************************/

const double* Contact_Happened = contactPropData-
>getValue(ContactHappened.c_str());
double* Update_Contact_Delta = contactPropData-
>getDelta(ContactHappened.c_str());
const double* Last_Break_Event_Elem1 = elem1PropData-
>getValue(ParticleBreakTime.c_str());
double* Break_Time_Delta_Elem1 = elem1PropData-
>getDelta(ParticleBreakTime.c_str());
double* Mass_loss_delta = simulationPropData->getDelta(TotalMassLoss.c_str());



if (*Contact_Happened == 0)
{
double relVelSq = relVel.lengthSquared();
double scale1 = m_particleMngr->getScale(elem1Id);

if (elem1Type == pName && elem2IsSurf == true && elem2Type == pName)  // both
elem1 and elem2 are breakable
{
// Update Elem 1 radius
double rStarOne = (Break_index_constant * elem1Density * (2 *
(elem1PhysicalRadius/scaling_factor))*relVelSq)+GZ_Minimum_breakage_constant;
if (rStarOne > 0.0)
{
double volume1 = elem1Volume * ((100 - rStarOne) * 0.01);
double radius1 = pow(0.75 * 0.3183098861837 * volume1, 0.333333); // inverse
PI 0.3183098861837
double newScale1 = scale1 * (radius1 / elem1PhysicalRadius);
double mass_loss = (elem1Volume - volume1) * elem1Density;

if (newScale1 < scale1 && newScale1 > PSizeLimitRatio)
{
m_particleMngr->setScale(elem1Id, newScale1);
*Update_Contact_Delta = 1;
*Break_Time_Delta_Elem1 = time - *Last_Break_Event_Elem1;
*Mass_loss_delta = mass_loss;
                              }
else if (scale1 > PSizeLimitRatio && newScale1 < PSizeLimitRatio)
{
m_particleMngr->setScale(elem1Id, PSizeLimitRatio);
*Update_Contact_Delta = 1;
*Break_Time_Delta_Elem1 = time - *Last_Break_Event_Elem1;
*Mass_loss_delta = mass_loss;
}
}


// Update Elem 2 radius
double rStarTwo = (Break_index_constant * elem2Density * (2 *
(elem2PhysicalRadius/scaling_factor)) * relVelSq) +
GZ_Minimum_breakage_constant;
if (rStarTwo > 0.0)
{
const double* Last_Break_Event_Elem2 = elem2PropData-
>getValue(ParticleBreakTime.c_str());
```

```
double* Break_Time_Delta_Elem2 = elem2PropData-
>getDelta(ParticleBreakTime.c_str());
double scale2 = m_particleMngr->getScale(elem2Id);

double volume2 = elem2Volume * ((100 - rStarTwo) * 0.01);
double radius2 = pow(0.75 * 0.3183098861837 * volume2, 0.333333);
double newScale2 = scale2 * (radius2 / elem2PhysicalRadius);
double mass_loss2 = (elem2Volume - volume2) * elem2Density;

if (newScale2 < scale2 && newScale2 > PSizeLimitRatio)
{
m_particleMngr->setScale(elem2Id, newScale2);
*Update_Contact_Delta = 1;
*Break_Time_Delta_Elem2 = time - *Last_Break_Event_Elem2;
*Mass_loss_delta = mass_loss2;
}
else if (scale2 > PSizeLimitRatio && newScale2 < PSizeLimitRatio)
{
m_particleMngr->setScale(elem2Id, PSizeLimitRatio);
*Update_Contact_Delta = 1;
*Break_Time_Delta_Elem2 = time - *Last_Break_Event_Elem2;
*Mass_loss_delta = mass_loss2;
}
}
}

if (elem1Type == pName && elem2IsSurf == true && elem2Type != pName) // elem1
is breakable but elem2 is not
{
// Update Elem 1 radius
double rStarOne = (Break_index_constant * elem1Density * (2 *
(elem1PhysicalRadius/scaling_factor)) * relVelSq) +
GZ_Minimum_breakage_constant;
if (rStarOne > 0.0)
{
double volume1 = elem1Volume * ((100 - rStarOne) * 0.01);
double radius1 = pow(0.75 * 0.3183098861837 * volume1, 0.333333); // inverse
PI 0.3183098861837
double newScale1 = scale1 * (radius1 / elem1PhysicalRadius);
double mass_loss = (elem1Volume - volume1) * elem1Density;

if (newScale1 < scale1 && newScale1 > PSizeLimitRatio)
{
m_particleMngr->setScale(elem1Id, newScale1);
*Update_Contact_Delta = 1;
*Break_Time_Delta_Elem1 = time - *Last_Break_Event_Elem1;
*Mass_loss_delta = mass_loss;
}
else if (scale1 > PSizeLimitRatio && newScale1 < PSizeLimitRatio)
{
m_particleMngr->setScale(elem1Id, PSizeLimitRatio);
*Update_Contact_Delta = 1;
*Break_Time_Delta_Elem1 = time - *Last_Break_Event_Elem1;
*Mass_loss_delta = mass_loss;
}
}
}

if (elem1Type == pName && elem2IsSurf != true) // elem1 is breakable and hits
geometry
		{
			// Update Elem 1 radius
```

```
double rStarOne = (Break_index_constant * elem1Density * (2 *
(elem1PhysicalRadius/scaling_factor)) * relVelSq) +
GZ_Minimum_breakage_constant;
if (rStarOne > 0.0)
{
double volume1 = elem1Volume * ((100 - rStarOne) * 0.01);
double radius1 = pow(0.75 * 0.3183098861837 * volume1, 0.333333); // inverse
PI 0.3183098861837
double newScale1 = scale1 * (radius1 / elem1PhysicalRadius);
double mass_loss = (elem1Volume - volume1) * elem1Density;

if (newScale1 < scale1 && newScale1 > PSizeLimitRatio)
{
m_particleMngr->setScale(elem1Id, newScale1);
*Update_Contact_Delta = 1;
*Break_Time_Delta_Elem1 = time - *Last_Break_Event_Elem1;
*Mass_loss_delta = mass_loss;
}
else if (scale1 > PSizeLimitRatio && newScale1 < PSizeLimitRatio)
{
m_particleMngr->setScale(elem1Id, PSizeLimitRatio);
*Update_Contact_Delta = 1;
*Break_Time_Delta_Elem1 = time - *Last_Break_Event_Elem1;
*Mass_loss_delta = mass_loss;
}
}
}

if (elem1Type != pName && elem2IsSurf == true && elem2Type == pName) // elem2
is breakable but elem1 isn't
{
// Update Elem 2 radius

double rStarTwo = (Break_index_constant * elem2Density * (2 *
(elem2PhysicalRadius/scaling_factor)) * relVelSq) +
GZ_Minimum_breakage_constant;
if (rStarTwo > 0.0)
{
const double* Last_Break_Event_Elem2 = elem2PropData-
>getValue(ParticleBreakTime.c_str());
double* Break_Time_Delta_Elem2 = elem2PropData-
>getDelta(ParticleBreakTime.c_str());
double scale2 = m_particleMngr->getScale(elem2Id);

double volume2 = elem2Volume * ((100 - rStarTwo) * 0.01);
double radius2 = pow(0.75 * 0.3183098861837 * volume2, 0.333333);
double newScale2 = scale2 * (radius2 / elem2PhysicalRadius);
double mass_loss = (elem2Volume - volume2) * elem2Density;

if (newScale2 < scale2 && newScale2 > PSizeLimitRatio)
{
m_particleMngr->setScale(elem2Id, newScale2);
*Update_Contact_Delta = 1;
*Break_Time_Delta_Elem2 = time - *Last_Break_Event_Elem2;
*Mass_loss_delta = mass_loss;
}
else if (scale2 > PSizeLimitRatio && newScale2 < PSizeLimitRatio)
{
m_particleMngr->setScale(elem2Id, PSizeLimitRatio);
*Update_Contact_Delta = 1;
*Break_Time_Delta_Elem2 = time - *Last_Break_Event_Elem2;
*Mass_loss_delta = mass_loss;
}
}
```

```
}
}
```